MEASUREMENT OF THE MASS AND WIDTH OF THE Z BOSON FROM Z$\rightarrow e^+e^-$ DECAY IN $\overline{P}P$ COLLISIONS AT $\sqrt{s} = 1.8$ TeV

BY

HOVHANNES KEUTELIAN

B.S., University of Illinois, 1983

THESIS

Submitted in partial fulfillment of the requirements
for the degree of Doctor of Philosophy in Physics
in the Graduate College of the
University of Illinois at Urbana-Champaign, 1990

Urbana, Illinois

AA0315

UNIVERSITY OF ILLINOIS AT URBANA-CHAMPAIGN

THE GRADUATE COLLEGE

MAY 1990

WE HEREBY RECOMMEND THAT THE THESIS BY

HOVHANNES KEUTELIAN

ENTITLED MEASUREMENT OF THE MASS AND WIDTH OF THE Z BOSON FROM $Z \rightarrow e^+e^-$ DECAY IN $\overline{P}P$ COLLISIONS AT $\sqrt{s} = 1.8$ TeV

BE ACCEPTED IN PARTIAL FULFILLMENT OF THE REQUIREMENTS FOR THE DEGREE OF DOCTOR OF PHILOSOPHY

L. E. Holloway
Director of Thesis Research

G Clendenson
Head of Department

Committee on Final Examination†

L. E. Holloway
Chairperson

Loella M Jones

David G Sutton

Bob Eisenstein

† Required for doctor's degree but not for master's.

O-517

MEASUREMENT OF THE MASS AND WIDTH OF THE Z BOSON FROM $Z \rightarrow e^+e^-$ DECAY IN $\overline{P}P$ COLLISIONS AT $\sqrt{s}$=1.8 TeV

Hovhannes Keutelian, Ph.D.
Department of Physics
University of Illinois at Urbana-Champaign, 1990
Professor L.E. Holloway, advisor

I report the results of an analysis to measure the mass and width of the Z gauge boson from $Z \rightarrow e^+e^-$ decays in $\overline{p}p$ collisions at $\sqrt{s} = 1.8$ TeV. The $Z \rightarrow e^+e^-$ data from the CDF detector yields a mass of the Z boson of $M_Z = 90.78 \pm 0.40(\text{stat.}) \pm 0.38(\text{syst.}) \pm 0.2(\text{scale})$ GeV/c^2 and a width of $\Gamma_Z = 2.8 \pm 1.0(\text{stat.}) \pm 0.5(\text{syst.})$ GeV.

To the memory of my brother

Kevork Keutelian

Acknowledgments

My special thanks go to Lee Holloway for giving me the opportunity to join the CDF group and for his help in finally getting me graduated. Words can't describe the 6 years of working together with Steve Errede. I learned a considerable amount from him in those years. I thank him for reinforcing my belief that detector capabilities must be understood in great detail in order to make the best measurements. Sampa, I thank for your support in difficult times. You are a dear friend who has a great skill in organizing social events and is fun to be with. Alain Kaloyeros, I'll forever treasure the fun times and your friendship. Phil and Vic, sharp tongued and quick thinking friends, I will forever remember the great parties we had in the Illinois house. Peter, I'm jealous of your hair.

Throughout the past 6 years many individuals shaped(warped) my thoughts and my professional and social life: PhDs, fellow graduate students, and professional support staff, both at the University of Illinois and at Fermilab. Amongst others, I want to thank Bob Sard, Shau-Jin Chang, Lorella M. Jones, Bob I. Eisenstein, Steve Errede, Sampa Bhadra, Inga Karliner, Allan Clark, Larry Nodulman, Henry Frisch, Barry Wicklund, Aseet Mukherjee, Peter Berge, Chris Wendt, Steve Hahn, Alain Gauthier, Tom Westhusing, Dave Smith, Phil Schlabach, Vic Scarpine, Peter Hurst, William Trischuk, Leigh Markoski, Karen Byrum, Jodi Lamoureux, Brian Winer, Tim Hessing, Tim Rohally, Dave Lesney, Jerry Wray, Lee Peek, Harold Scott, Vidas Simaitis, Fred Cogswell, Tom Trumpinski.

My greatest thanks go to my family for their support and encouragement.

This research was supported in part by the U.S. Department of Energy under contract DE-AC02-76ERO1195.

CDF Collaboration for the 1988-1989 Run

F. Abe,[8] D. Amidei,[4] G. Apollinari,[11] M. Atac,[4] P. Auchincloss,[14] A. R. Baden,[6] A. Bamberger,[19] A. Barbaro-Galtieri,[9] V. E. Barnes,[12] F. Bedeschi,[11] S. Behrends,[2] S. Belforte,[11] G. Bellettini,[11] J. Bellinger,[18] J. Bensinger,[2] A. Beretvas,[4] J. P. Berge,[4] S. Bertolucci,[5] S. Bhadra,[7] M. Binkley,[4] R. Blair,[1] C. Blocker,[2] A. W. Booth,[4] G. Brandenburg,[6] D. Brown,[6] E. Buckley,[14] A. Byon,[12] K. L. Byrum,[18] C. Campagnari,[3] M. Campbell,[3] R. Carey,[6] W. Carithers,[9] D. Carlsmith,[18] J. T. Carroll,[4] R. Cashmore,[19] F. Cervelli,[11] K. Chadwick,[4] G. Chiarelli,[5] W. Chinowsky,[9] S. Cihangir,[4] A. G. Clark,[4] D. Connor,[10] M. Contreras,[2] J. Cooper,[4] M. Cordelli,[5] D. Crane,[4] M. Curatolo,[5] C. Day,[4] S. Dell'Agnello,[11] M. Dell'Orso,[11] L. Demortier,[2] P. F. Derwent,[3] T. Devlin,[14] D. DiBitonto,[15] R. B. Drucker,[9] J. E. Elias,[4] R. Ely,[9] S. Errede,[7] B. Esposito,[5] B. Flaugher,[14] G. W. Foster,[4] M. Franklin,[6] J. Freeman,[4] H. Frisch,[3] Y. Fukui,[8] Y. Funayama,[16] A. F. Garfinkel,[12] A. Gauthier,[7] S. Geer,[6] P. Giannetti,[11] N. Giokaris,[13] P. Giromini,[5] L. Gladney,[10] M. Gold,[9] K. Goulianos,[13] H. Grassmann,[11] C. Grosso-Pilcher,[3] C. Haber,[9] S. R. Hahn,[4] R. Handler,[18] K. Hara,[16] R. M. Harris,[9] J. Hauser,[3] T. Hessing,[15] R. Hollebeek,[10] L. Holloway,[7] P. Hu,[14] B. Hubbard,[9] B. T. Huffman,[12] R. Hughes,[10] P. Hurst,[7] J. Huth,[4] M. Incagli,[11] T. Ino,[16] H. Iso,[16] H. Jensen,[4] C. P. Jessop,[6] R. P. Johnson,[4] U. Joshi,[4] R. W. Kadel,[4] T. Kamon,[15] S. Kanda,[16] D. A. Kardelis,[7] I. Karliner,[7] E. Kearns,[6] R. Kephart,[4] P. Kesten,[2] R. M. Keup,[7] H. Keutelian,[7] S. Kim,[16] L. Kirsch,[2] K. Kondo,[16] S. E. Kuhlmann,[1] E. Kuns,[14] A. T. Laasanen,[12] J. I. Lamoureux,[18] W. Li,[1] T. M. Liss,[7] N. Lockyer,[10] C. B. Luchini,[7] P. Maas,[4] M. Mangano[11] J. P. Marriner,[4] R. Markeloff,[18] L. A. Markosky,[18] R. Mattingly,[2] P. McIntyre,[15] A. Menzione,[11] T. Meyer,[15] S. Mikamo,[8] M. Miller,[3] T. Mimashi,[16] S. Miscetti,[5] M. Mishina,[8] S. Miyashita,[16] Y. Morita,[16] S. Moulding,[2] A. Mukherjee,[4] L. F. Nakae,[2] I. Nakano,[16] C. Nelson,[4] C. Newman-Holmes,[4] J. S. T. Ng,[6] M. Ninomiya,[16] L. Nodulman,[1] S. Ogawa,[16] R. Paoletti,[11] A. Para,[4] E. Pare,[6] J. Patrick,[4] T. J. Phillips,[6] R. Plunkett,[4] L. Pondrom,[18] J. Proudfoot,[1] G. Punzi,[11] D. Quarrie,[4] K. Ragan,[10] G. Redlinger,[3] J. Rhoades,[18] M. Roach,[17] F. Rimondi,[19] L. Ristori,[11] T. Rohaly,[10] A. Roodman,[3] D. Saltzberg,[3] A. Sansoni,[5] R. D. Sard,[7] A. Savoy-Navarro,[4] V. Scarpine,[7] P. Schlabach,[7] E. E. Schmidt,[4] M. H. Schub,[12] R. Schwitters,[6] A. Scribano,[11] S. Segler,[4] Y. Seiya,[16] M. Sekiguchi,[16] P. Sestini,[11] M. Shapiro,[6] M. Sheaff,[18] M. Shochet,[3] J. Siegrist,[9] P. Sinervo,[10] J. Skarha,[18] K. Sliwa,[17] D. A. Smith,[11] F. D. Snider,[3] R. St. Denis,[6] A. Stefanini,[11] R. L. Swartz, Jr.,[7] M. Takano,[16] K. Takikawa,[16] S. Tarem,[2] D. Theriot,[4] M. Timko,[15] P. Tipton,[9] S. Tkaczyk,[4] A. Tollestrup,[4] G. Tonelli,[11] J. Tonnison,[12] W. Trischuk,[6] Y. Tsay,[3] F. Ukegawa,[16] D. Underwood,[1] R. Vidal,[4] R. G. Wagner,[1] R. L. Wagner,[4] J. Walsh,[10] T. Watts,[14] R. Webb,[15] C. Wendt,[18] W. C. Wester, III,[9] T. Westhusing,[11] S. N. White,[13] A. B. Wicklund,[1] H. H. Williams,[10] B. L. Winer,[9] A. Yagil,[4] A. Yamashita,[16] K. Yasuoka,[16] G. P. Yeh,[4] J. Yoh,[4] M. Yokoyama,[16] J. C. Yun,[4] F. Zetti[11]

[1] *Argonne National Laboratory, Argonne, Illinois 60439*; [2] *Brandeis University, Waltham, Massachusetts 02254*
[3] *University of Chicago, Chicago, Illinois 60637*; [4] *Fermi National Accelerator Laboratory, Batavia, Illinois 60510*
[5] *Laboratori Nazionali di Frascati, Istituto Nazionale di Fisica Nucleare, Frascati, Italy*
[6] *Harvard University, Cambridge, Massachusetts 02138*; [7] *University of Illinois, Urbana, Illinois 61801*
[8] *National Laboratory for High Energy Physics (KEK); Tsukuba, Ibaraki 305, Japan*
[9] *Lawrence Berkeley Laboratory, Berkeley, California 94720*
[10] *University of Pennsylvania, Philadelphia, Pennsylvania 19104*
[11] *Istituto Nazionale di Fisica Nucleare, University and Scuola Normale Superiore of Pisa, I-56100 Pisa, Italy*
[12] *Purdue University, West Lafayette, Indiana 47907*; [13] *Rockefeller University, New York, New York 10021*
[14] *Rutgers University, Piscataway, New Jersey 08854*; [15] *Texas A&M University, College Station, Texas 77843*
[16] *University of Tsukuba, Tsukuba, Ibaraki 305, Japan*; [17] *Tufts University, Medford, Massachusetts 02155*
[18] *University of Wisconsin, Madison, Wisconsin 53706*; [19] *Visitor*

Contents

1 Introduction 1
1.1 Theory 1
2 Apparatus and Data Collection 4
2.1 Tracking Detectors 4
2.2 Calorimeter Detectors 9
2.3 Trigger 12
2.4 Data Collection 14
3 Event Selection and Detector Calibration 14
3.1 Event Selection 14
3.2 Detector Calibration 26
3.2.1 Determining the Momentum Scale 26
3.2.2 Determining the Energy Scale 31
4 Measuring the Z Mass and Width 35
4.1 Fitting Procedure 35
4.1.1 Fitting algorithm 35
4.1.2 Invariant mass calculation from measured quantities 37
4.1.3 Calculation of the effective mass resolution 38
4.1.4 Mass acceptance of Et and fiducial cuts 42
4.1.5 Fitted Mass Range Selection 42
4.2 Fitting Systematics 46
4.2.1 Structure function contribution to the Z mass fit 46
4.2.2 QED radiative effect to the Z Mass 46
4.3 Fitting the $\overline{p}p$ Z data 48
5 Results and Future Prospects 58
A $Z \rightarrow e^+e^-$ Event Display 62

B The Kolmogorov-Smirnov Statistic 67

C CDT z position calibration 71

References 81

Vita 86

1 Introduction

In the Standard Model of electroweak interactions, the mass of the Z gauge boson is directly related to the $SU(2)_L$ and U(1) coupling constants g' and g [1], and to the vacuum expectation value of the Higgs field [2]. The width of the Z is also predicted in the theory from its couplings to the quark and lepton generations. This thesis describes a measurement of the Z mass and width based on an integrated luminosity of 4.4 pb^{-1} of $\overline{p}p$ collisions at $\sqrt{s} = 1.8$ TeV collected with the Collider Detector at Fermilab(CDF)[3]. This analysis uses data collected during 1988-1989 CDF's second collider run. The Z mass and width values are extracted by fitting the invariant mass distribution of e^+e^- pairs from $Z \rightarrow e^+e^-$ decay candidates. The distribution of the invariant masses is assumed to form a Gaussian smeared relativistic Breit-Wigner distribution. Parton luminosity and internal radiative effects have been included in the analysis.

1.1 Theory

Having been predicted by the standard model of electroweak interactions[1], the experimental discovery of weak bosons at the CERN $\overline{p}p$ collider successfully concluded the long theoretical development to understand the weak nuclear force[4]. The standard model is a non-abelian gauge theory based on the gauge group $SU(2)_L \times U(1)_Y$ where the ideas of Yang-Mills theories, isospin invariance, spontaneous symmetry breaking, and Higgs mechanism merge in one common concept. The input parameters themselves cannot be predicted but have to be taken from appropriate experiments.

The standard model with its four input parameters(besides fermion masses and mixing angles); A(photon), W, and Z gauge bosons, and the Higgs field, essentially describes the electroweak processes between fermions. These physically observable quantities are related to the gauge couplings of the theory. The following choice of weak mixing angle:

$$\cos\theta_W = \frac{M_W}{M_Z}, \tag{1}$$

leads to the expression where the electron charge is related to both the weak mixing angle and the gauge coupling in the model:

$$e = g\sin\theta_W. \tag{2}$$

The determination of W, Z, Higgs masses test the validity of the last equation. By applying the theory to the $\mu^- \rightarrow \nu_\mu e^- \overline{\nu_e}$ decay, via W exchange, one obtains the relation:

$$M_W^2 = \frac{\pi\alpha}{\sqrt{2}G_F\sin^2\theta_W}, \tag{3}$$

where the fine structure constant $\alpha = 1/137.03604(11)$, and the Fermi constant $G_F = 1.166344(11) \times 10^{-5}\mathrm{GeV}^{-2}$. The electroweak mixing angle θ_W is determined by experiments involving Z exchange. A value of $\sin^2\theta_W = 0.231 \pm 0.006$ is obtained from neutrino-quark scattering. The experimental input parameters α, G_F, $\sin^2\theta_W$ and the above relations help determine the weak boson masses in the lowest order application of the standard model:

$$M_W = 77.6 \pm 1.0 \text{ GeV/c}^2 , \quad M_Z = 88.5 \pm 0.8 \text{ GeV/c}^2 .$$

These values are modified by including higher order quantum effects, the "radiative corrections", in the mass calculation. These radiative corrections lead to the interdependence of W, Z, Higgs masses with an additional dependence on yet undetermined top quark mass. The earlier W and Z mass measurements show the radiative corrections are necessary to explain the experimental results[19]:

$$M_W = 81.0 \pm 1.3 \text{ GeV/c}^2 , \quad M_Z = 92.4 \pm 1.8 \text{ GeV/c}^2 .$$

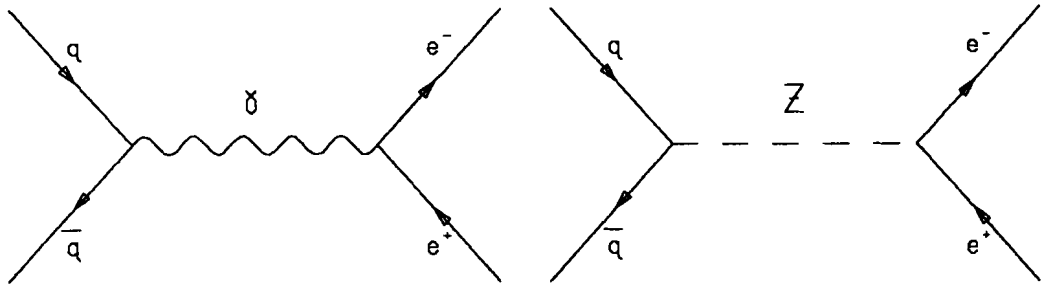

Figure 1: Lowest order Feynman diagrams associated with $\bar{p}p \rightarrow e^+e^-$.

At lowest order, both photon exchange and Z exchange contribute to electron pair production in hadronic collisions; the Feynman diagrams for these processes are shown in figure 1. A straightforward calculation based on these diagrams gives the cross section [5]

$$\sigma = \int_0^1 dx_a \int_0^1 dx_b \sum_q q(x_a, \hat{s})\bar{q}(x_b, \hat{s}) \left[A\frac{1}{\hat{s}} + B\frac{\hat{s} - M_Z^2}{(\hat{s} - M_Z^2)^2 + (\hat{s}\Gamma/M_Z)^2} + C\frac{\hat{s}}{(\hat{s} - M_Z^2)^2 + (\hat{s}\Gamma/M_Z)^2} \right]. \tag{4}$$

Here $q(x_a, \hat{s})$ and $\bar{q}(x_b, \hat{s})$ are the quark distribution functions in the proton and antiproton, and the sum is over the quark species. The first term in the cross section is due to photon exchange and the third due to Z exchange, while the the second term arises from the quantum mechanical interference of these two subprocesses. The constants A, B, and C depend on the standard model parameters. The mass determination relies on the shape of the distribution, the Z pole, and not on the absolute cross section; the exact forms of A, B, and C are not important in this analysis. The variable $\hat{s}$ is just the invariant mass of the e^+e^- pair, m^2.

2 Apparatus and Data Collection

The Collider Detector at Fermilab(CDF) is a 5000 ton multipurpose detector built to study 1.8 TeV/c^2 $\bar{p}p$ collisions at the Fermilab Tevatron (Figures 2,3). Event analysis is based on charged particle tracking, magnetic momentum analysis and fine-grained calorimetry. The combined electromagnetic and hadron calorimeters have approximately uniform granularity in pseudorapidity-azimuthal angle and extend to within 2° of the beam directions. Charged particle momenta are analyzed in 1.4116 Tesla solenoidal magnetic field; the magnetic field was generated by a superconducting coil which is 3 meters in diameter and 5 meters in length.

In the CDF detector, the positive z-axis of a right handed coordinate system was defined to be parallel to the direction travelled by protons. The polar angle, θ, is measured from the proton beam direction. The x-axis is in the horizontal plane of the Tevatron and is pointed radially out of the ring, and the y-axis is pointed upward. The pseudorapidity, $\eta = -\ln(\tan(\theta/2))$, is an approximately Lorentz invariant measure applicable to distributions in the polar angle variable. The CDF detector is described in detail in reference [3]; a brief description of components used in this analysis follows.

2.1 Tracking Detectors

Radially closest to the beryllium beam pipe and nominal interaction point was the Vertex Time Projection Chamber(VTPC)(Figure 4.) Covering a total length of 2.8 meters along the beamline, this chamber was used to determine the vertex position along the z axis by measuring charged particle tracks direction in the r-z plane. The r.m.s. resolution in z is 1 mm [6]. In the Z candidate events the vertex position measured along z was required to be within ±60 cm. about the center of the detector, z=0. The distribution in z of reconstructed vertices in candidate Z events is shown in figure 5 and is well approximated by a Gaussian of mean 0.7 ± 2.5 cm and width of 31.9 ± 2.7 cm.

The VTPC was surrounded by the Central Tracking Chamber(CTC). Both resided in

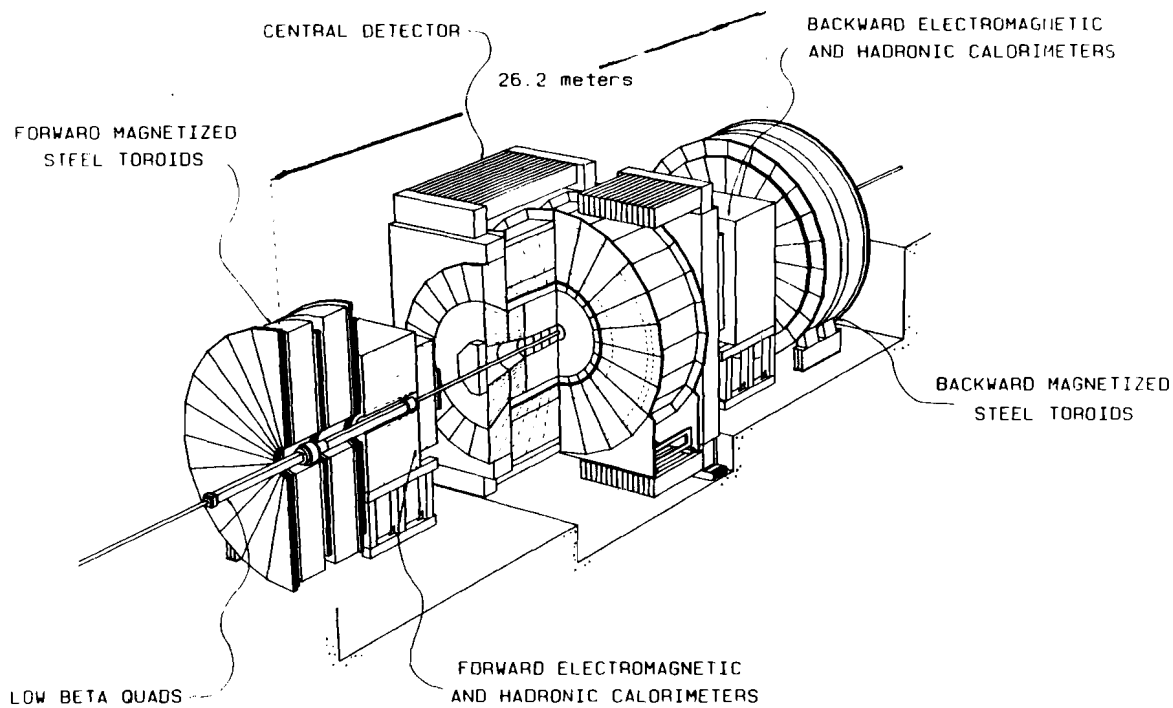

Figure 2: A perspective view of the CDF detector showing the central detector and the forward and backward detectors.

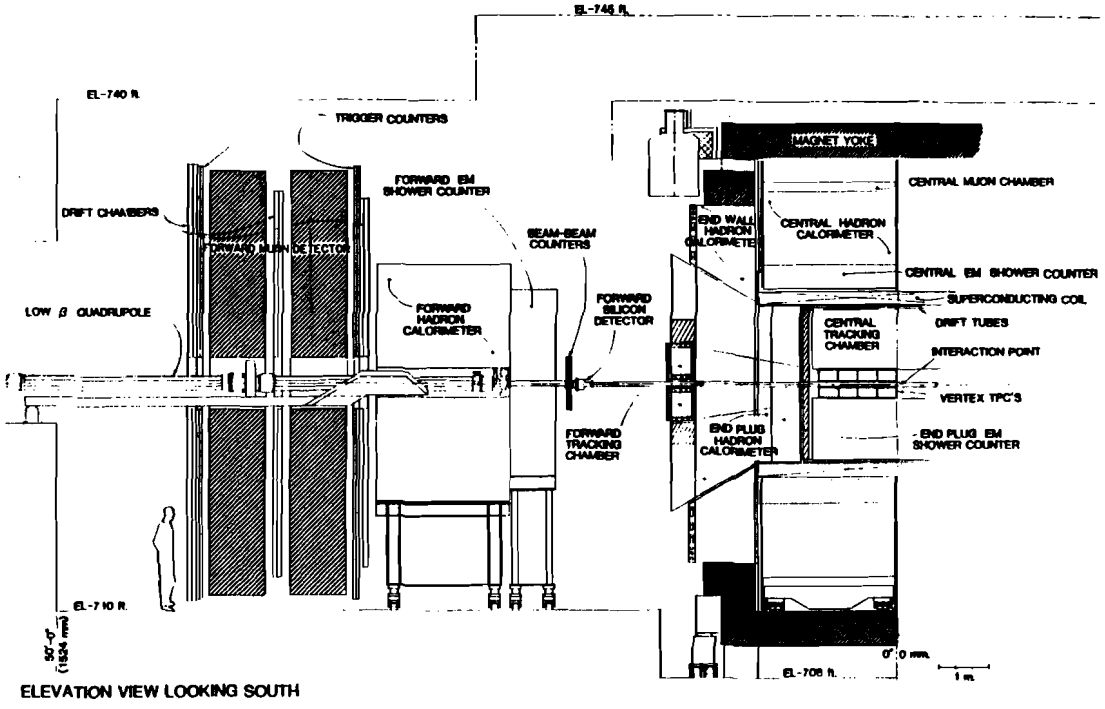

Figure 3: A cut-away view through the forward half of CDF. The detector is forward-backward symmetric about the interaction point.

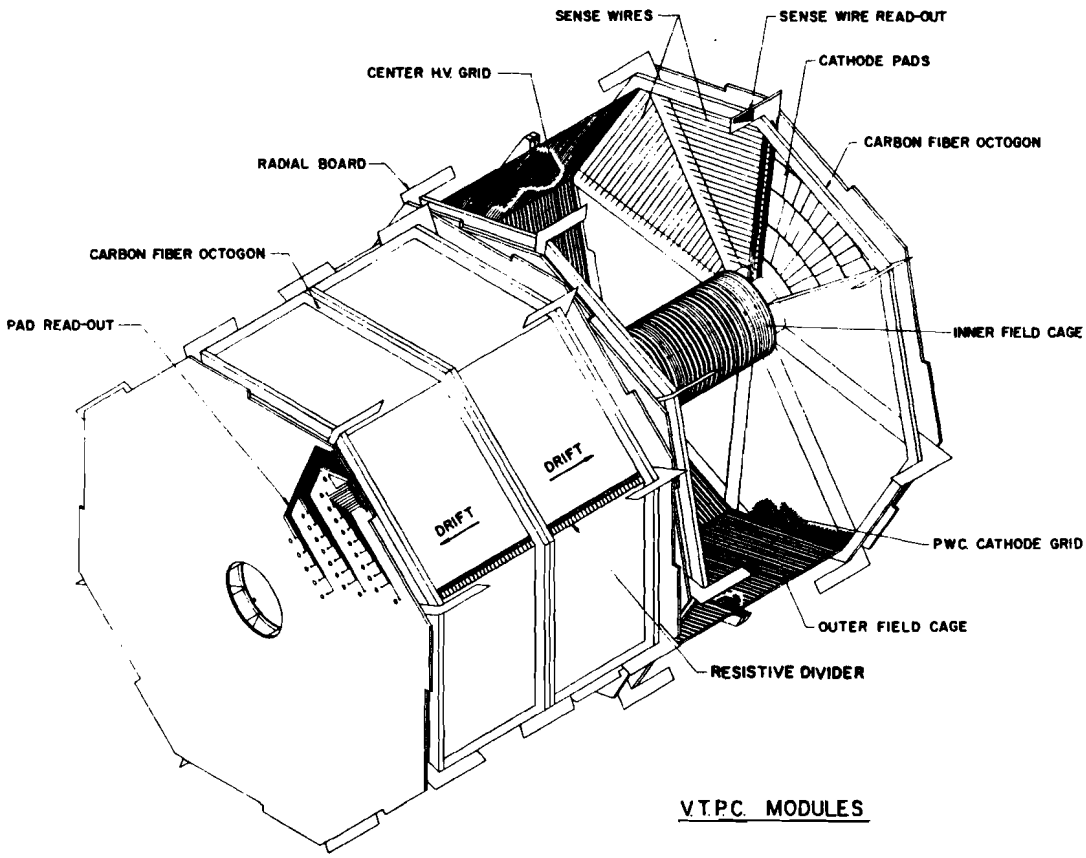

Figure 4: An isometric view of two VTPC modules. They are rotated in ϕ by 11.3° with respect to each other.

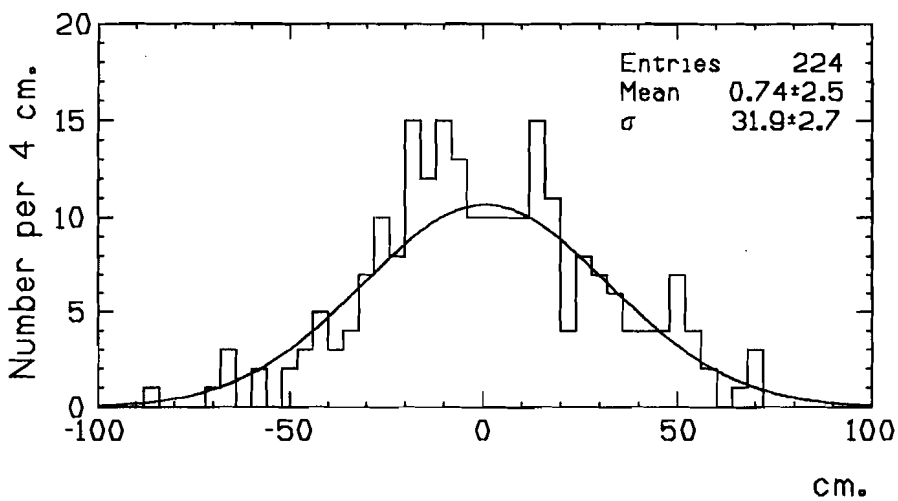

Figure 5: The event vertex position distribution in z of the Z candidates.

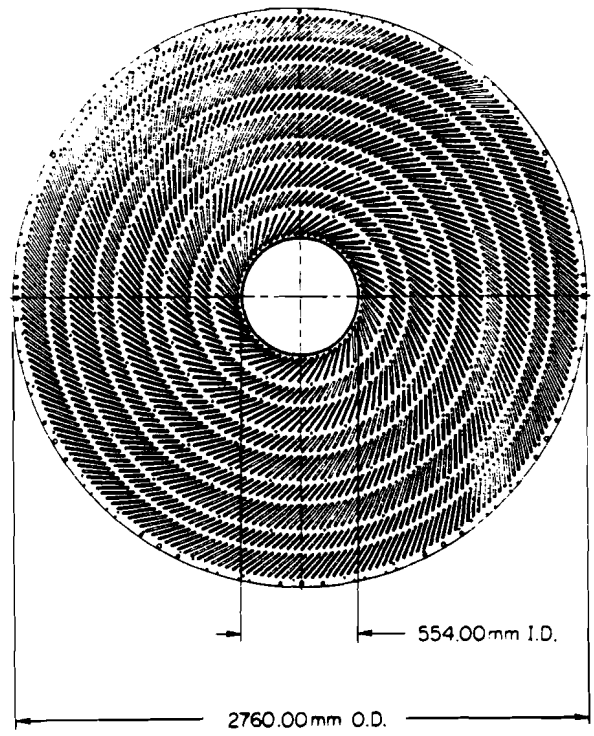

Figure 6: End view of the Central Tracking Chamber showing the location of the slots in the aluminum endplates.

1.4116 Tesla solenoidal magnetic field. The CTC was designed to determine the curvature of charged particle tracks in the $r - \phi$ plane, and thereby determine their momentum. The CTC has 84 layers of wires grouped together in nine "superlayers,"(Figure 6.) Five of the nine superlayers have twelve sense wires parallel to the beam direction and the magnetic field. These axial layers were used for the primary determination of the track curvature. The other four layers have 6 sense wires at a $\pm 3°$ stereo angle with respect to the axial sense wires. These provided the information necessary to determine the angle of the tracks with respect to the beam axis. In increasing radii the nine superlayer's stereo angles with respect to the axial direction are: $0°, +3°, 0°, -3°, 0°, +3°, 0°, -3°, 0°$. All superlayers have tilted cells at a 45° angle with respect to the radial direction to compensate for the Lorentz angle of electron drift in the magnetic field (Figure 7.) In

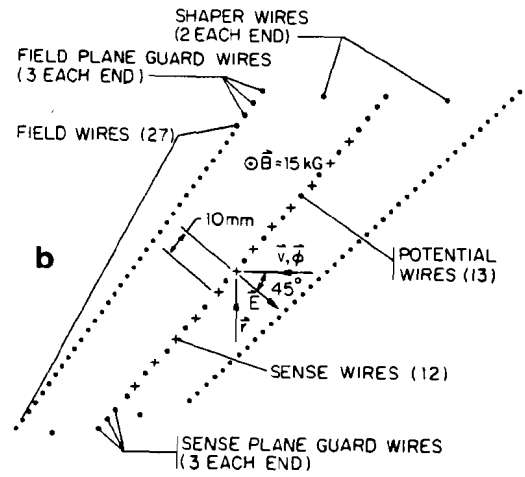

Figure 7: Wire nomenclature for an axial cell.

ideal conditions this allows the electrons to drift azimuthally thus simplifying the time-to-distance relationship.

The CTC alone provided a momentum resolution of $\sigma_{p_t} = 0.002 \times p_t{}^2$ for isolated tracks, p_t is measured in GeV/c . The addition of a well defined vertex position extended the effective tracking radius from 100 cm to 130 cm, thereby halving the effective resolution to $\sigma_{p_t} = 0.0011 \times p_t{}^2$. The average effective mass resolution of Z decays is about $\sigma_m = 2.8$ GeV/c^2 . The p_t resolution scales as $1/l^2$, where l is the radial path of a charged particle in the solenoidal magnetic field. This improvement in resolution reduced the systematic uncertainties of momentum and energy scales; details are given in section 3.2. The momentum resolution is degraded if a track does not pass through all layers of the chamber. Events used in this analysis were required to have electrons and positrons pass through all layers of the Central Tracking Chamber.

2.2 Calorimeter Detectors

The central ($-1.1 < \eta < 1.1$) region of the calorimeter is made up of lead-scintillator electromagnetic shower counters followed by an iron-scintillator hadron calorimeter. The central calorimeter is segmented into projective towers, each tower subtends a rapidity

interval of $\Delta\eta = 0.11$ and a ϕ interval of $\Delta\phi = 15°$.

The Central Electromagnetic Calorimeter(CEM)[7] was used to measure the energy of the electrons from Z decays. These energy values in conjunction with the measured angles by CTC were used to calculate the invariant masses of the Z candidates. The CEM consists of 31 layers of polystyrene scintillator interleaved with 30 layers of lead absorber. Including the outer chamber wall, magnet coil and the calorimeter itself, a total of 18 radiation lengths of material are presented to electrons. The ensemble absorbs 98% of the energy of the 45 GeV electrons from a Z decay. The calorimeter is broken up into 15^0 wedges in ϕ (Figure 8.) Light from the scintillators is read out through wave length shifters on both sides of a wedge. A central wedge is divided up into 10 towers labeled from 0(near $\theta = 90°$) through 9. The Central Electromagnetic Strip(CES) chamber is located at the EM shower maxima; in the CEM at a depth of 6 radiation lengths. This proportional chamber with orthogonal wires and strips was used to measure the electron shower positions in ϕ and z views. The electron shower positions from W and Z decays were measured with 2 - 3 mm accuracy. The effective region of the strip chamber in the plane of a wedge is $|x| \leq 22.5$ cm(in ϕ) and 6.0 cm. $\leq z \leq 239.4$ cm(in z), where the the active area of the CEM extends to $|x| \leq 23.1$ cm and 4.2 cm $\leq z \leq 246.0$ cm.

The 478 CEM towers were calibrated with 50 GeV electrons in a test-beam. These calibrations were maintained by referring them to Cs^{137} source signals [8]. This procedure provided a set of calibrations that was good to about 2.5% after 5 years. In 1989, the CEM was calibrated $in - situ$ using inclusive electrons in the CDF $\overline{p}p$ data. These calibrations are described in section 3.2. The energy resolution, $\sigma_E/E = 13.5\%/\sqrt{E \sin\theta}$, of individual CEM towers was determined from test beam data; the determination of the tower-to-tower resolution of 2.4% is explained in section 4. The effective mass resolution of Z decays is about $\sigma_m = 2.0$ GeV/c^2 ; details of calculation are given in section 4. With this resolution and with the CEM ability to capture radiated photons from electrons in a Z decay it was possible to probe the width of the Z mass resonance.

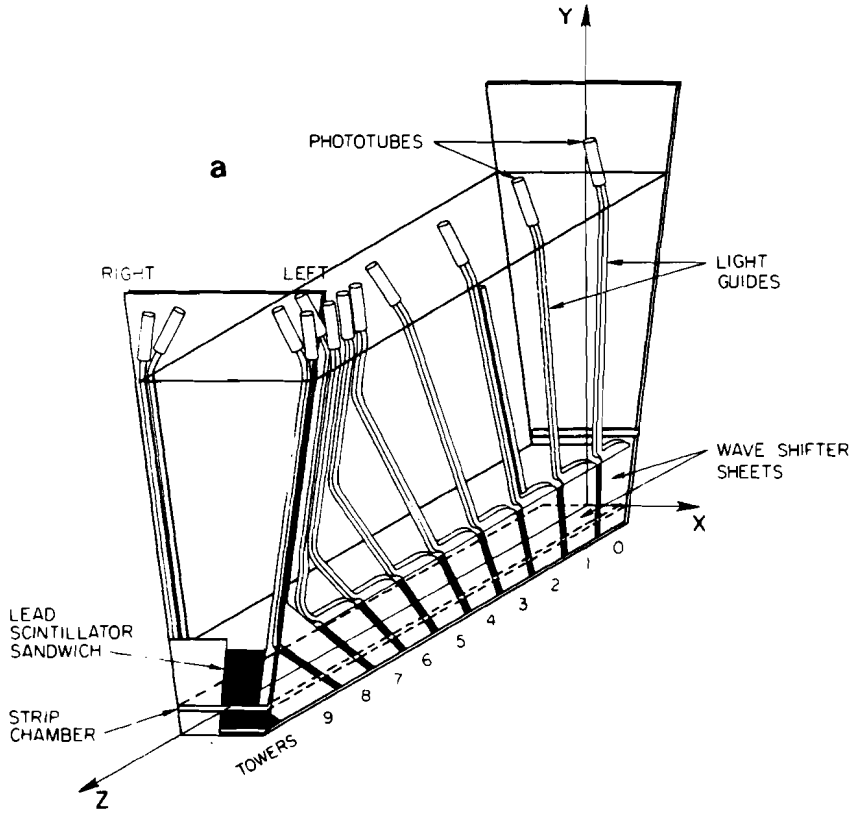

Figure 8: Schematic of the wedge module of the CDF central calorimeter and the coordinate system used for response mapping. Layout of the light-gathering system of the CEM calorimeter wedge is shown.

The Central Hadron Calorimeter(CHA) and the Endwall Hadron Calorimeter(WHA) [9] were used to measure the hadronic energy associated with the central EM clusters. The CHA consists of 33 layers of scintillating plastic interleaved with 32 layers of 2.5 cm thick steels. The calorimeter has 4.7 absorption length. The WHA consists of 16 layers of scintillating plastic interleaved with 15 layers of 5.0 cm thick steels. The calorimeter has 4.5 absorption length. The energy resolution, $\sigma_E/E = 4\% + 33\%/\sqrt{E \sin\theta}$, of CHA and WHA was determined from test beam data. The hadron calorimeter energy resolution is about 3 times poorer compared to the CEM energy resolution; this was no drawback when the hadron calorimeter energy measurement was used to reject pions. The hadronic to electromagnetic energy ratio, Had/EM, was used to reject backgrounds imitating an electron shower. The measured hadronic energy was in no other way used in this analysis.

2.3 Trigger

The interaction rate during the 1988-1989 running at the Tevatron collider was 10^5 times higher than the CDF data recording capability. With a four level trigger[10] system it was possible to select interesting events. A description of the triggers relevant to the collection of Z candidates follows.

The lowest level of the triggering scheme, level 0, selected inelastic collisions by requiring that time of flight counters on either side of the interaction region be hit. This is the minimum bias trigger. This trigger's decision was available in time to inhibit data taking during the next beam crossing. Beam crossing occurred every 3.5 μs.

The level 1 decision was made within the $7\mu s$ allowed by level 0. If the event failed in level 1, the front end electronics were reset, in time for the second crossing after the initial level 0 decision.

The level-1 calorimeter trigger system computed the energy flow in both the electromagnetic and hadronic compartments of the calorimeter. For W and Z electron candidates, all events fulfilled the requirement that there be at least 6 GeV in a single trigger

cell of the central electromagnetic calorimeter. A trigger cell covered two towers of the CEM in the same wedge, 0.2 in η by 15° in ϕ.

In level 2, the electron trigger(as well as other CDF level 2 triggers) used 2 dimensional tracks found by the Central Fast Tracker(CFT) [11], a hardware track processor which used fast timing information from the CTC to detect high transverse momentum tracks. The track finder analyzed prompt hits from the axial sense wires of the CTC to identify tracks by comparing prompt hits in the CTC to predetermined hit patterns for the range of transverse momenta allowed by the CFT trigger threshold. The processor covered the p_t range from 2.5 to 15 GeV/c with a momentum resolution of $\sigma_{p_t} = 0.035 \times p_t{}^2$($p_t$ in GeV/c). The list of found tracks was presented to the rest of the CDF trigger system for use in level 2 decisions.

The level-2 trigger selected central electrons if: 1) a cluster [12] of transverse energy was found above 12 GeV., 2) a track found by the CFT, with a nominal threshold $p_t > 6$ GeV/c, pointed towards the wedge that contained the cluster, and 3) less than 12.5% of the energy in the trigger cell was in the hadron compartment. By studying events passing other triggers, this trigger was found to be 98% efficient for W electrons. Comparisons of this trigger to lower threshold electron triggers revealed that it was fully efficient at 15 GeV [13].

A level 3 trigger system was also implemented during the 1988-89 running period. This consisted of a farm of 60 Motorola 68020 processors. All the raw data was available for decision making. Due to constraints on execution time the streamlined versions of the complete CDF reconstruction code was used.

The level-3 electron filter required that the electron cluster, identified in level 2, be reconstructed with at least 12 GeV in software. The filter also required that the fast reconstruction yield a track of at least 6 GeV/c, associated with the cluster.

The Z candidates were also selected by another trigger that did not use tracking information. The diphoton trigger decision was solely based on the calorimeter information.

The level-2 trigger selected diphotons if: 1) Two clusters[14] of transverse energy were found above 10 GeV, 2) less than 12.5% of the energy in each trigger cells were in the hadron compartment. The level-3 diphoton filter required the EM clusters, identified in level-2, to be reconstructed and have transverse energy above 10 GeV, and to have less than 12.5% of the energy in the hadron towers.

The overlap of the electron and the diphoton triggers in the Z candidates is close to 100%. In a di-electron sample 114 events passed the level-2 electron trigger and 113 events passed the diphoton trigger. These events were selected from 81-101 GeV/c^2 invariant mass range. The inclusive electron cuts are applied to one of the EM clusters in the di-electron events, and the second cluster is required to pass HAD/EM$<$ 0.1 and there is 3D CTC track pointing to it.

2.4 Data Collection

The data used in this analysis was collected over a 12-month period from June of 1988 through May of 1990(Figure 9.) The peak machine luminosity grew to over $2 \times 10^{30}\text{cm}^{-2}\text{s}^{-1}$. The overall trigger rate was limited to 1-2 Hz by the speed the data was transferred to tape. The average event record contained 150 kbytes of information. The final 4.4 pb^{-1} sample consists of 4×10^5 events recorded on 5,500 magnetic tapes.

3 Event Selection and Detector Calibration

3.1 Event Selection

The selection of the Z candidates relies on the electron cuts shown in table 1. The event selection proceeds by first preparing a sample where at least one of the CEM clusters passes the inclusive electron cuts. Next the Z candidates are selected by requiring that the invariant mass of an EM cluster pair be greater than 50 GeV/c^2 and three dimensional CTC tracks to point at both EM clusters. The EM cluster is defined in the detector calibration section. The mass and width fit uses a high quality sample of Z candidates

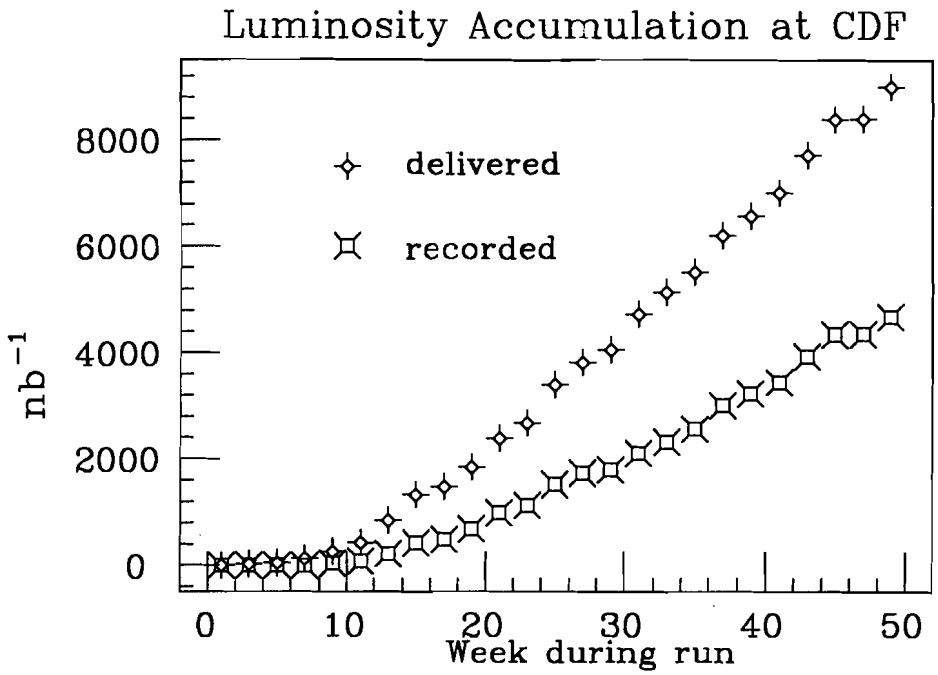

Figure 9: Data collection during 1988-1989 $\bar{p}p$ collider run by CDF

where both EM clusters pass the electron cuts. Description of fitting is given in section 4.

Figure 10 shows the geometry of towers within a CEM wedge. The target marks indicate the reference points used to obtain the position dependent energy corrections from test beam electron data[15]. Fiducial cuts in both x and z views of a wedge ensure a well measured energy of an EM cluster. By being a good source of electrons, the distributions of quantities from electrons in the $W \rightarrow e\nu$ sample give an idea about the shape and the range of the cuts mentioned in table 1. The preparation of W sample uses cuts based on missing transverse energy and a cut on the transverse energy of electrons, $E_t > 25$ GeV.

A Gaussian of mean -0.94 ± 0.72 cm and width of 29.5 ± 1.5 cm approximates the event vertex distribution (Fig. 11) in z of the W candidates. The requirement of an event vertex position within ± 60 cm is an accepted fiducial cut by the CDF collaboration. This cut primarily ensures the full acceptance of the VTPC for $|\eta| \leq 3$ units in pseudorapidity [16]. The mean value of the ratio of calorimeter hadron energy to elec-

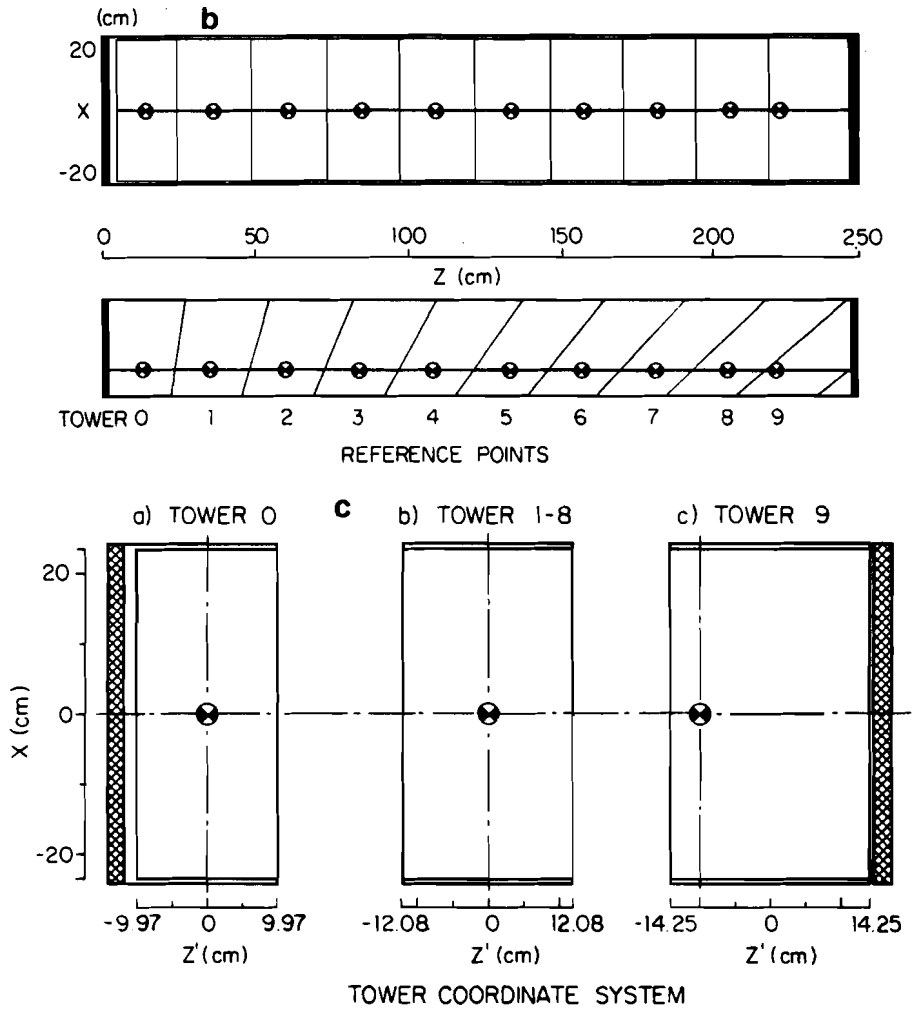

Figure 10: Tower geometry of the CEM wedge. Tower 0 is near $\theta = 90°$. The x axis of the tower is along the $r\phi$ plane of the CDF's right handed coordinate system. The Tower 9 material is thinner(radiation length) compared to other towers, hence its contribution is removed from the Z mass analysis.

Table 1: Quantities used in the Z mass and width analysis.

Name of the cut	Description of the cut
3D track required	An EM cluster is considered an electron candidate if three dimensional CTC track is pointing at it.
Fiducial	To keep the electron showers away from wedge edges in ϕ; $\|x\| < 21$ cm. Contribution from tower 9 to the EM cluster energy is removed.
Event Z Vertex	An event vertex to be within ± 60 cm; 2σ of the beam position spread.
CES-CTC	Track matching between the Central Electromagnetic Strip(CES) chamber and the CTC.
LShare	A measure of the energy sharing among towers in an EM cluster compared to the sharing observed at the testbeam.
Had/Em	The ratio of calorimeter hadron energy to electromagnetic energy.
E/P	The ratio of calorimeter EM energy to tracking momentum.
Mass range	Any CEM cluster pair with an invariant mass greater than 50 GeV/c^2 is considered a possible Z candidate.
CES χ^2s	The consistency of the EM shower profile observed in the CES chamber compared to the testbeam showers.

tromagnetic energy(Fig. 12), HAD/EM≤ 0.1, indicates that on the average $1.40 \pm 0.03\%$ of electromagnetic energy leaks to the hadron calorimeter. The "LShare" is a measure of consistency of the energy lateral sharing among CEM towers of an EM cluster compared to the sharing observed at the testbeam. The center location of the LShare distribution(Fig. 13) is at 0 with r.m.s value of 0.06. The LShare cut of ≤ 0.2 selects more than 99% of electrons from W sample. The ratio of electromagnetic energy to the tracking momentum, E/P, is an effective electron identification cut in the CDF detector. Except for values greater than 1.1, a Gaussian of mean 1.010 ± 0.001 and width of 0.051 ± 0.001 well approximates the E/P(Fig. 14) distribution. The tail above 1.1 reflects the QED radiation from electrons. The width of the distribution is the convolution of the measurement uncertainties of CEM and CTC, its value agrees with what is expected. Without the QED radiation from electrons the mean value of this distribution is 1. In section

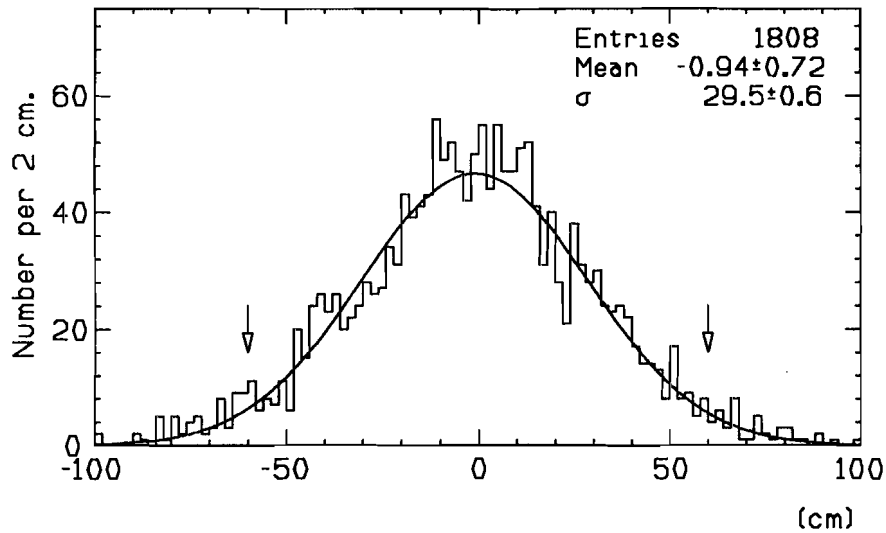

Figure 11: The event vertex distribution in z of the W candidates. The arrows indicate the value of the vertex cut.

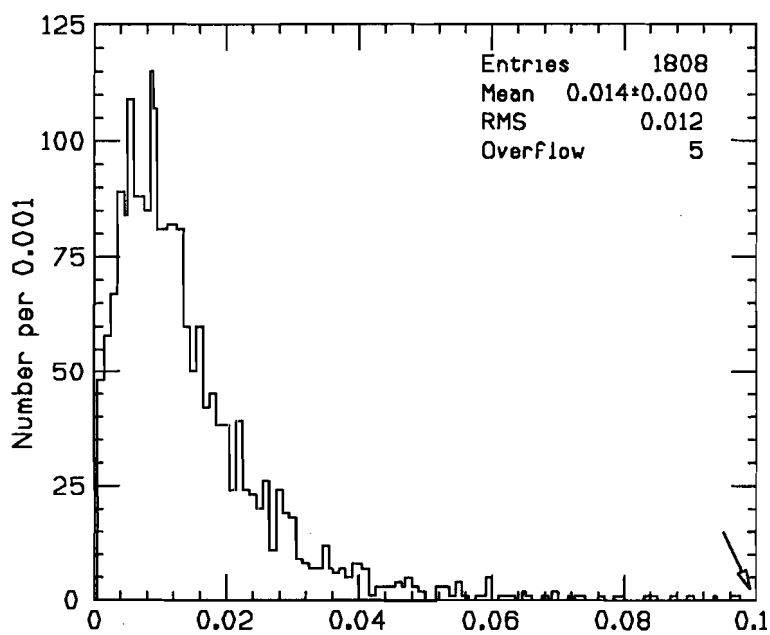

Figure 12: The HAD/EM distribution of electrons from W candidates. The upper limit on this variable is 0.10.

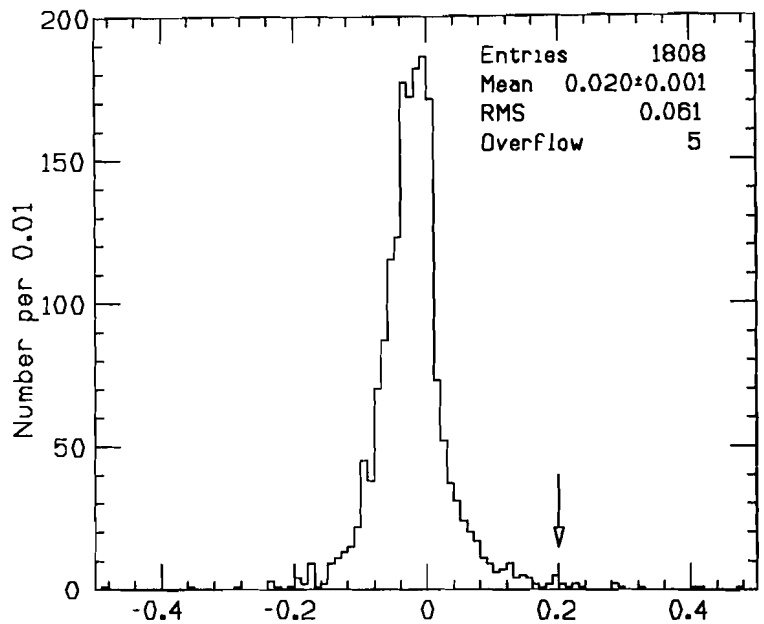

Figure 13: The LShare distribution of electrons from W candidates. The arrow points at the upper limit of this cut

3 the mean value of $< E/P >$, for an upper cut E/P$\leq$ 1.4, is going to be used to determine the energy scale. The CES-CTC track matching resolutions in $r\phi$ and z views (Fig. 15a:b) are about $\sim 2-3$ mm. These values are consistent with the intrinsic position resolution of CES and the angular resolutions of CTC. Track matching cut of ± 1 cm in $r\phi$ and ± 1.5 cm in z keeps most of the electrons from W candidates. The CES χ^2s are measures of consistency of the observed EM shower profile compared to the test beam showers; these have 9 degrees of freedom in each ϕ and z views. A large fraction of electrons have χ^2 values below 10(Fig. 16a:c). The distribution of the average χ^2((Fig. 16c), $\chi^2_{avg.} = (\chi^2_{strip} + \chi^2_{wire})/2$, is similar to distributions in each view. In the fitting section, I'll give details on the effect of the CES χ^2 on the Z mass value. A $\chi^2_{avg.} \leq 10$ is the strictest limit studied in the fitting section.

The preparation of an inclusive electron sample proceeds by requiring at least one electron candidate per event satisfying the following: (1) A three dimensional CTC track pointing to the EM cluster; (2) In a wedge(Fig. 8) the cluster to be located in towers 0

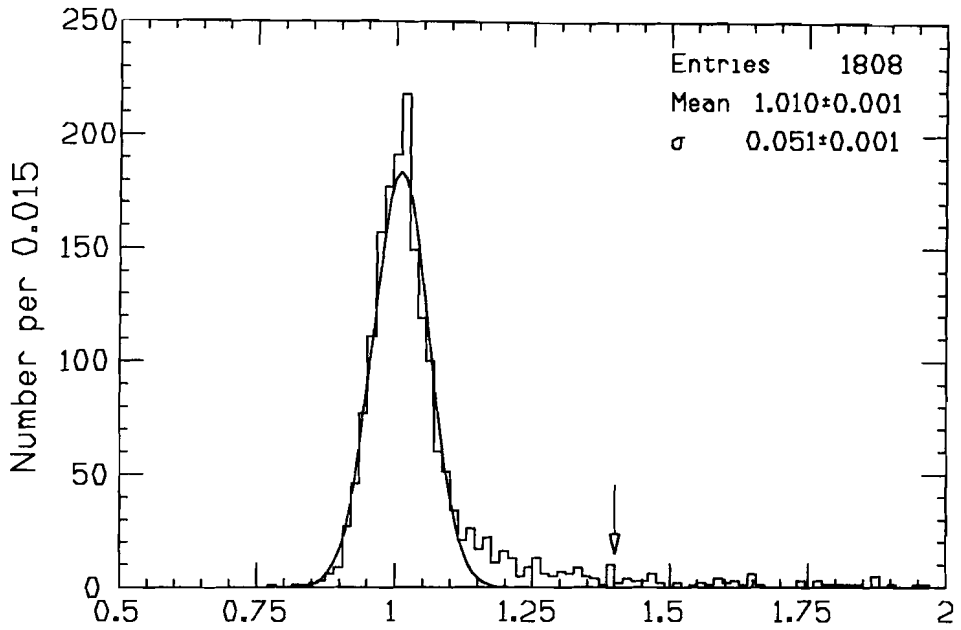

Figure 14: The E/P distribution of electrons from W candidates. The arrow indicates upper limit on this variable used in selecting Z candidates.

through 8; (3) The event vertex in z is to be within ±60 cm. (4) In a wedge the electron is to be within ±21 cm in the x direction and > 10 cm in the z direction as to have its shower fully contained; (5) a match between the strip chamber shower position and the extrapolated track position of $|\Delta z| \sin\theta \leq 1.5$ cm in the z direction and $|\Delta x| \leq 1.0$ cm in the ϕ direction; (6) the ratio of hadronic to electromagnetic calorimeter energy be less than 0.10; (7) the lateral shower profile in the calorimeter consistent with an electron shower, LShare$\leq$ 0.2; (8) the ratio of electromagnetic energy to track momentum, E/P $\leq$ 2.0.

Two additional requirements: (i) an EM cluster pair be greater that 50 GeV/c^2 and (ii) three dimensional CTC tracks point at both EM clusters, select Z candidates from the inclusive electron sample. This di-electron sample consists of 215 EM cluster pairs(Fig. 17) formed from 209 events. In this sample there is an event with an invariant mass of 190.2 GeV/c^2 ; this single event is consistent with the Z and Drell-Yan production cross section, recorded luminosity, and the efficiencies of electron cuts[17].

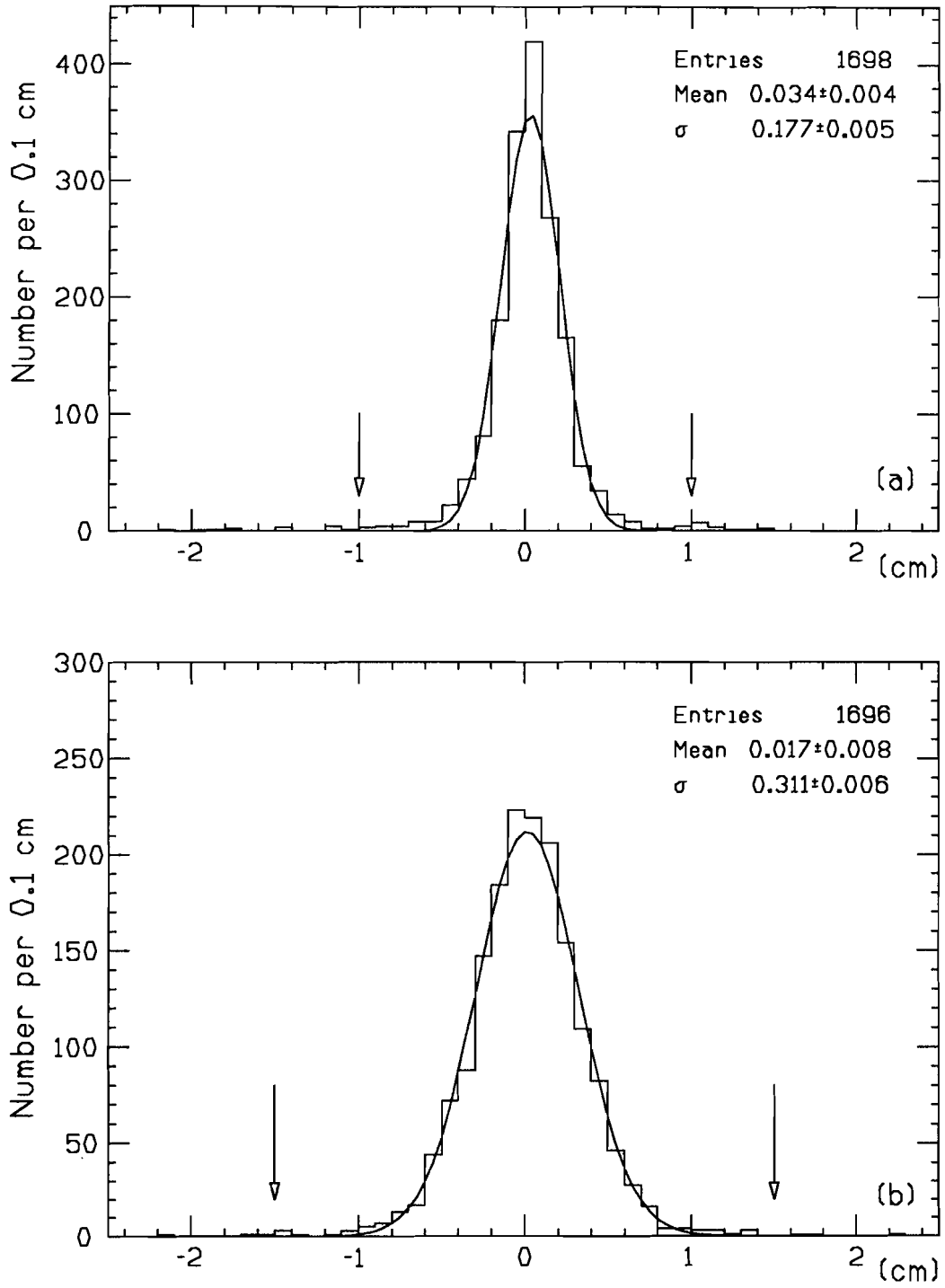

Figure 15: The CES-CTC track matching distributions both in a) x and b) z views. The track matching variable in z is $\Delta z \sin\theta$.

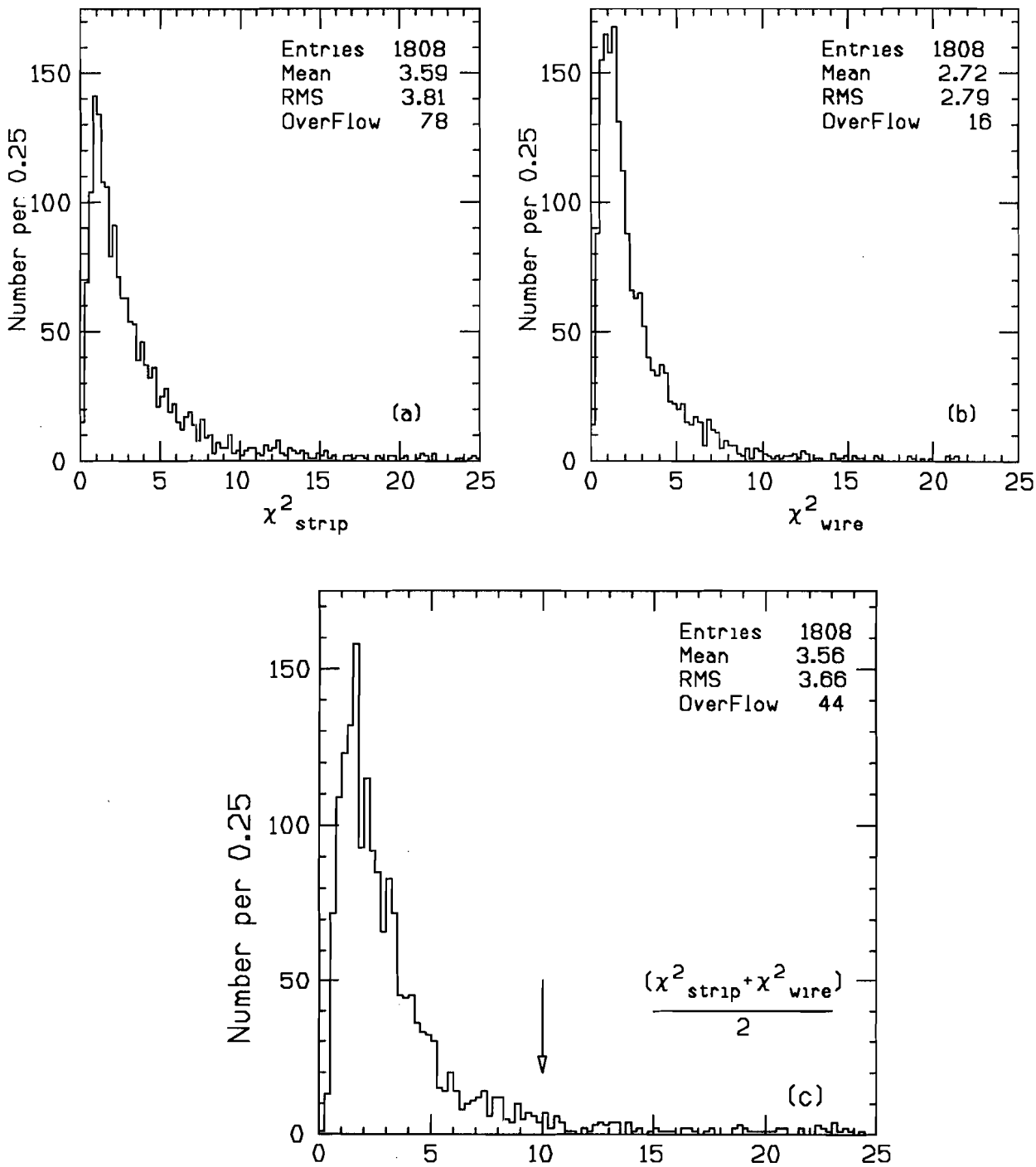

Figure 16: The CES χ^2 distributions.

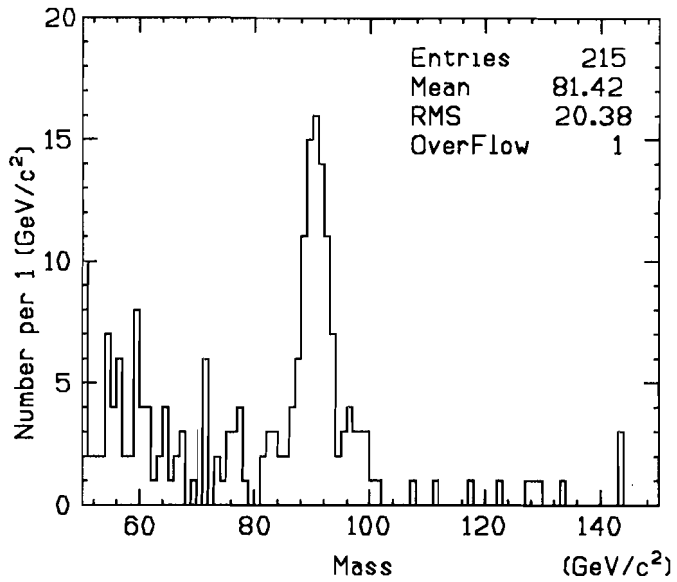

Figure 17: Invariant mass distribution of EM cluster pairs where at least one of the clusters passed the inclusive electron cuts. The Z resonance is clearly visible.

The distributions of electron variables from the di-electron sample agree pretty well with the distributions of electrons from W candidates (Fig. 18, 19.) The EM cluster distributions from di-electron sample carry the following information: 1) The mean value of the Had/EM distribution indicates 2% electromagnetic energy leakage to the hadron calorimeter as expected from testbeam data; 2) The CES-CTC track matching resolution both in $r\phi$ and z are ~ 2 mm and ~ 3 mm. 3) The center of the LShare distribution is at 0 with an r.m.s value of 0.06. The electron distributions without cuts can show how effective an electron cut is by counting the number of events falling outside the range of the cut. The E/P rejects largest number of events and the Had/EM fewer number of events.

There is correlation among the electron cuts; their individual efficiency depend on their order of application. The combined efficiency is independent of the order of application. From these distributions one cannot deduce how many Z candidate events will survive after applying the electron cuts on the second EM cluster in the di-electron sample. The implicit assumption in this analysis is that the efficiencies of electron cuts do not distort the di-electron invariant mass distribution near the Z resonance. Indeed,

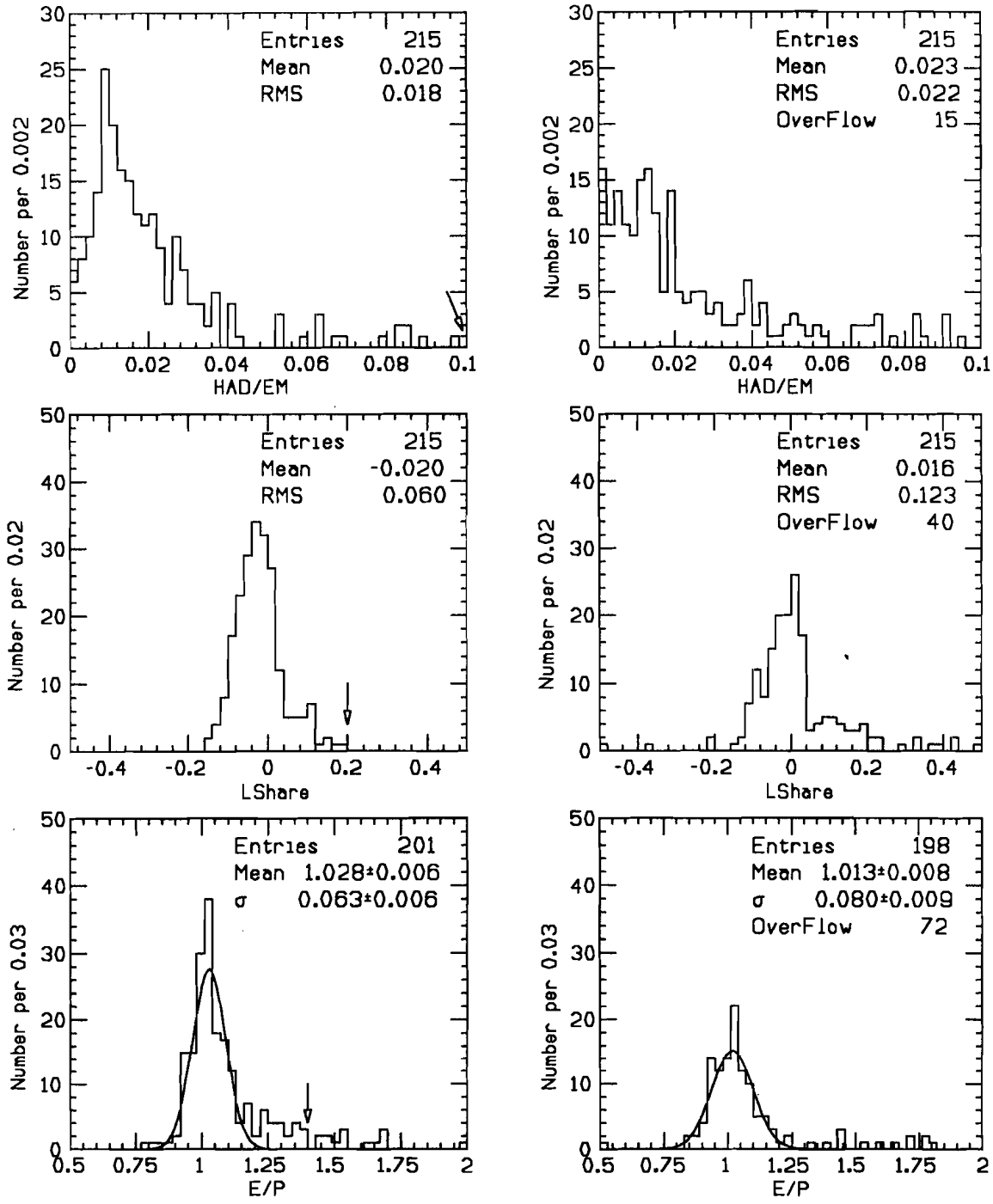

Figure 18: The histograms on the left side are prepared from information of the EM cluster, from an EM pair, that passed the inclusive electron cuts. The second cluster information, regardless if it passes or fails the inclusive electron cuts, are used to prepare the histograms on the right side. The minimum cuts on the second cluster are a 3D CTC track pointing at the cluster, and HAD/EM$\leq$ 0.125. Comparison of these histograms with those from W electrons show HAD/EM, LShare, and E/P distributions are similar in both W and Z decays; these are as expected.

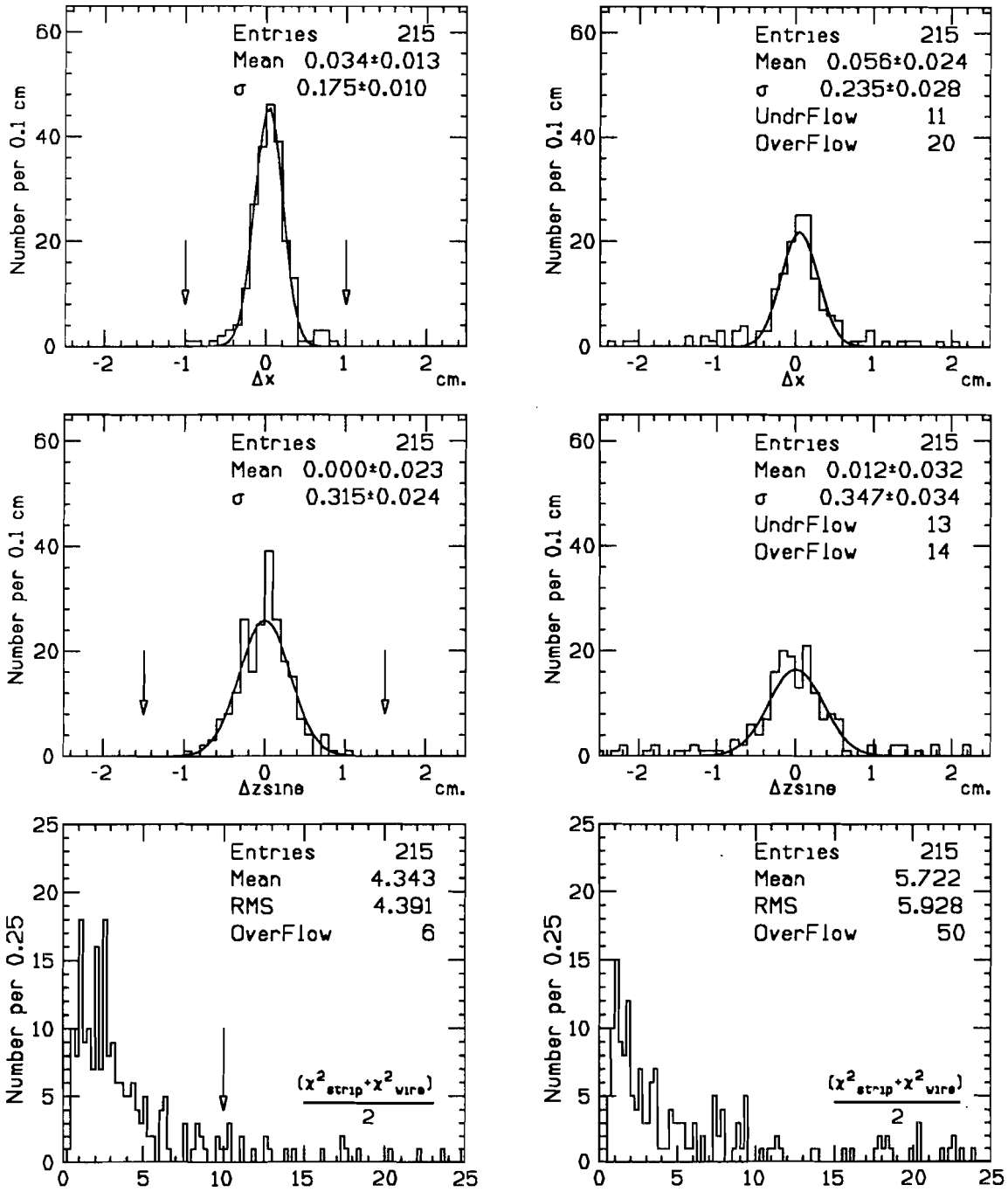

Figure 19: The histograms on the left side are prepared from information of the EM cluster, from an EM pair, that passed the inclusive electron cuts. The second cluster information, regardless if it passes or fails the inclusive electron cuts, are used to prepare the histograms on the right side. The minimum cuts on the second cluster are a 3D CTC track pointing at the cluster, and HAD/EM$\leq$ 0.125. Comparison of these histograms with those from W electrons show CES-CTC track matching in $r\phi$ and z views, the CES $\chi^2_{avg.}$, are similar in both W and Z decays.

the data is modeled well by a Gaussian smeared Breit-Wigner distribution within the 81-101 GeV/c^2 range.

After the application of inclusive electron cuts to the second EM cluster 92 out of 209 events survive from the di-electron sample(Fig. 20.) One of the event has a mass of 190.2 GeV/c^2 and another event contributes 2 EM pairs to this sample. The conclusion of a visual scan of the event with multiple EM pairs is that the event has no Z candidate characteristics; there are 6 EM clusters in the event. This event does not enter in the mass and width fits. In the fitting section, I'll use a stricter E/P cut to make the calculation of the EM cluster energy consistent with the energy calibration. Details of CES χ^2 cut and discussion of backgrounds are given in the mass and width fitting section.

3.2 Detector Calibration

In this analysis, the momentum measurement sets the absolute mass scale. Hence the overall uncertainty of the mass stems from the uncertainty in the momentum scale determination. First I describe the CTC calibration with emphasis on determining the momentum scale and afterwards the CEM calibration which determines the energy scale.

3.2.1 Determining the Momentum Scale

The momentum calculation of a charged track uses the magnetic field magnitude, the measured curvature, and angles in the CTC. The formula used to calculate momentum is: $p = (\beta/C)\sqrt{1+\cot^2\theta}$, where the factor β contains the magnetic field magnitude, and C is the track curvature. A discussion of the magnetic field uncertainty and the curvature systematics follows.

The uncertainty in the absolute magnetic field is $\pm 0.05\%$, where the dominant contribution to this uncertainty stems from the fact that the solenoid was operated at a current of 4650A, whereas it was mapped at 5000A [18]. Also the determination of the average magnetic field magnitude contributes to this uncertainty; the solenoid's magnetic field is

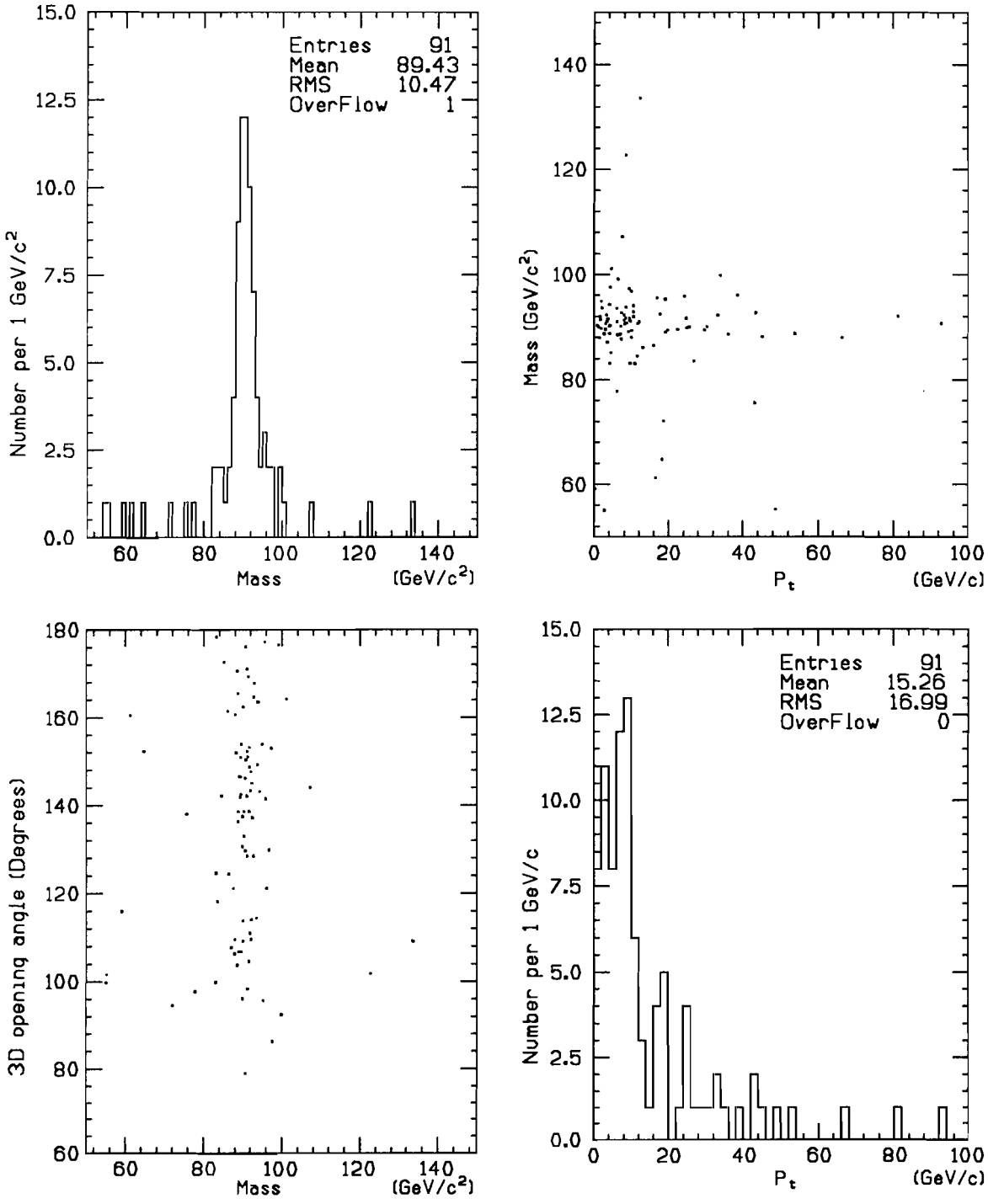

Figure 20: Invariant mass distribution of EM cluster pairs where electron cuts are applied to both clusters. Pt distribution of the pairs are also shown. The 3D dimensional opening angle show no visible bias on the invariant masses.

position dependent along the axial and the radial directions.

Calibration of the CTC begins with the determination of timing offsets, drift velocities and a beam position on a run by run basis. The beam center is determined with 5 μm accuracy for a 50 μm beam size in the $r\phi$ plane. The determination of the chamber alignment uses charged particle tracks in minimum bias events. The tilted geometry of the drift chamber cells means that each track provides a measurement of the drift-time relationship. This information reduces timing measurement systematics in the curvature determination. This data is collected online and provides calibration parameters for the first pass reconstruction. Having reconstructed tracks with this alignment we find 180 μm average axial residuals and average stereo residuals of 225 μm.

Remaining tracking chamber distortions fall into two categories: 1) azimuthal misalignment and 2) overall magnification due, for example, to mechanical loading. The azimuthal alignment errors can effect the chamber's resolution at high momenta, by leading to charge dependent sagitta errors of the type:

$$\frac{1}{p} = \frac{1}{p_{\text{true}}} + \frac{1}{\Lambda} \qquad (e^+, \mu^+) \tag{5}$$

$$\frac{1}{p} = \frac{1}{p_{\text{true}}} - \frac{1}{\Lambda} \qquad (e^-, \mu^-) \tag{6}$$

By comparing average energy to momentum ratios $< E/P >$ for electrons and positrons the sagitta error is:

$$\frac{1}{\Lambda} = \frac{1}{< E >_+ + < E >_-}(< E/p >_+ - < E/p >_-). \tag{7}$$

Since the W $\rightarrow$ eν sample is a good source of electrons and positrons, the alignment procedure uses this sample to zero the sagitta error. The determination of 166 wire-layer azimuth offsets(one for each wire-layer at each end of the chamber less two phases) begins by equalizing both $< E/p >$ and $\sigma_{<E/p>}$ for electrons and positrons; the additional requirement is that the electrons and the positrons to emanate from a common beam spot. The sign dependent shifts are 3% before correction and 0.3% after correction. There

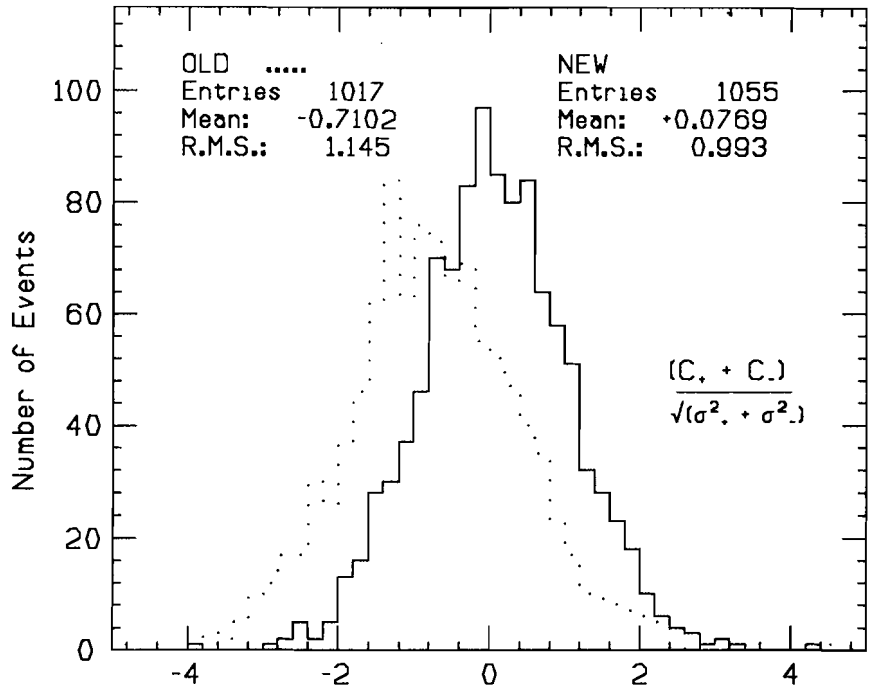

Figure 21: Curvature match of cosmic ray muons before and after aligning the CTC geometry.

are ten times more W events compared to Z events, therefore higher order corrections to CTC alignment do not limit the accuracy of the Z mass measurement; the statistical fluctuations dominate the measurement accuracy.

The effect of gravity on the chamber wires degrades the chamber resolution. The verification of both the correction for the effect of gravity on the sense wires and the alignment uses cosmic rays; cosmic rays provide apparent tracks of equal momenta but opposite charge. The curvature matching (Fig. 21) of cosmic ray branches shows the improvement. The mean value corresponds to $1/\Lambda \sim (8.7 \pm 3.5) \times 10^{-5}(\mathrm{GeV/c})^{-1}$, about 0.3% of the measured curvature and is consistent with results from $< E/p >$ calibration. The average curvature of an electron from W decay is $\sim 6 \times 10^{-5}\mathrm{cm}^{-1}$. This corresponds to a sagitta value of 0.15 cm. The alignment does not change the scale; it only improves the resolution at high momenta. By including the beam position in the track fit, the chamber's resolution becomes $\sigma_{p_t} = 0.0011 \times p_t^2 (p_t \; in \; \mathrm{GeV/c})$, or about 1.3 GeV/c for a 35 GeV/c track typical of W decay leptons.

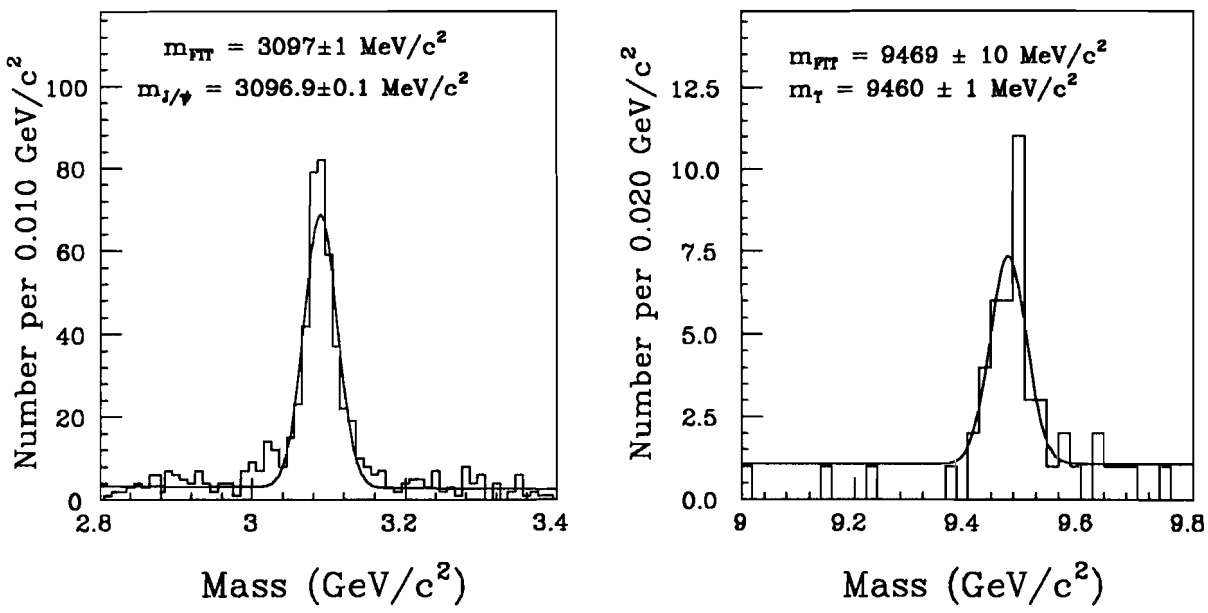

Figure 22: Dimuon invariant mass spectrum.

The check for residual chamber dilation uses the CDF's sample of J/ψ and $\Upsilon(1S)$ dimuons(Fig. 22). The reconstructed masses of 3.097 ± 0.001 GeV/c^2 and 9.469 ± 0.010 GeV/c^2 agree well with the world-average values[19]. The J/ψ mass agrees to within its 0.03% statistical uncertainty and the $\Upsilon(1S)$ mass is $0.1 \pm 0.1\%$ high. The average transverse momenta, in the dimuon samples, of muons is ~ 5 GeV/c. By adding in quadrature the uncertainties of the magnetic field, the sagitta error and the $\Upsilon(1S)$ mass, the tracking chamber momentum scale uncertainty is $\sim 0.11\% = \sqrt{(0.05^2 + 0.00^2 + 0.10^2)}\%$.

The checks mentioned above support the assumption that the curvature determination is linear for leptons from W and Z decays. No mass resonance exists between the Z and the Υ mass resonances to further verify linearity assumption. For transverse momenta typical of W and Z decays the CTC track fitting code reproduces track curvatures to better than 0.1%, hence a conservative estimate of the momentum scale is set to 0.2% for high momentum tracks.

3.2.2 Determining the Energy Scale

In addition to the electron shower energy, the energy scale determination relies on the momentum scale of the CTC and on the simulation of W events in the CDF detector. Electron showers in the central calorimeter may span 1 to 3 calorimeter towers in a single wedge. The electron shower energy calculation includes at most the two highest energy towers of the electromagnetic calorimeter. However, to form an EM cluster from more than one tower, the neighbouring tower must have more than 100 MeV of E_t. The phototube electronics introduces a measurement uncertainty of $\sim$ 30 MeV per tower. The electron energy calculation uses: the measured CEM cluster energy, a position dependent correction of each tower from a response map [15], a correction to remove tower to tower variations. The mathematical expression is:

$$\mathrm{E_i^{corrected}} = \frac{\mathrm{E_i^{measured}}}{\mathrm{r_i\ q_i}}, \tag{8}$$

where r is the position dependent and q is the tower to tower variation corrections for the i-th tower. The response map correction uses the EM shower position measured by the strip chambers or the extrapolated position of the CTC track in the strip chamber plane. This correction accounts for light attenuation, the effect of cracks, and transverse leakage and is accurate to $\pm 1.1\%$ over the CEM fiducial area the W electrons occupy.

The removal of tower to tower variation uses a sample of inclusive electrons with $E_t \geq$ 15 GeV. The tower to tower constants are common to electrons and positrons; where the transverse energy cut prevents trigger bias. The factor $\mathrm{q_i}$ is equal to the inverse of the mean $< E/p >_i$ of each tower. The average $< E/p >_i$ is close to unity and its use is suitable to correct a few percent effect.

The following cuts select a sample of inclusive electrons: 1) The fraction of the electron candidate's energy(the energy in the electromagnetic calorimeter) leaking into the hadron calorimeter(HAD/EM) be less than 0.04; 2) the energy sharing among towers in the cluster be consistent with the sharing observed at the testbeam, LShare$\leq$ 0.2; 3) the

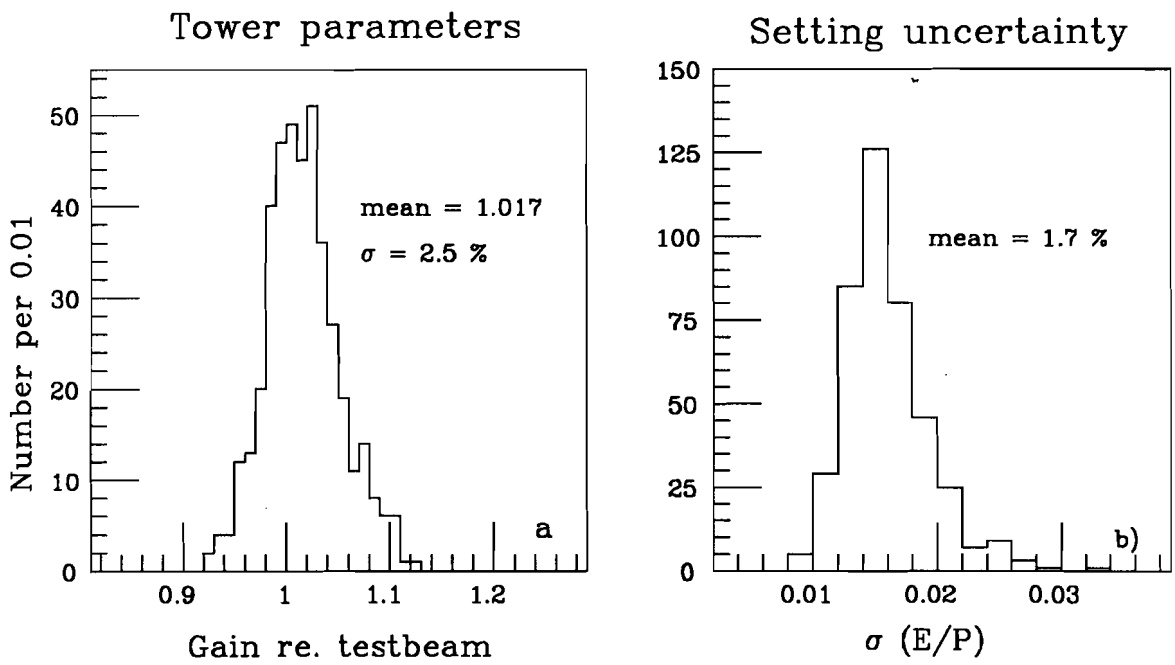

Figure 23: CEM tower mapping parameters and setting uncertainty.

shower profile seen in the strip chamber be consistent with testbeam showers($\chi^2 < 10$ for 9 degrees of freedom in each view); 4) the CTC track and shower positions match within $|\Delta x| \leq 1$ cm and $|\Delta z| \sin\theta \leq 8$ mm; 5) the ratio of electromagnetic energy to tracking momentum be within $0.7 \leq E/p \leq 1.3$; 6) the pulse height ratio of wires to strips of the shower chamber be within 40% of the nominal. This results in the selection of 17,000 electron candidates, on the average 35 electrons per tower. The selection is not highly restrictive, leaving about 4% background. This background can shift the mean E/p, but influences all towers similarly. The resulting relative tower gains have an average statistical accuracy of 1.7%. Figure 23 shows a distribution of the ratio of individual gains to those derived from test beam calibrations which has an rms width of 2.5%.

The overall scale factor for CEM energy comes from a comparison of E/p for W electrons to a prediction which includes radiative effects. The calibration relies on the comparison of the electron momentum, measured with the tracking chamber, to its energy from the calorimeter. The distribution of the E/p ratio is independent of the electron's kinematic distribution. The average energy does not exactly match the average momen-

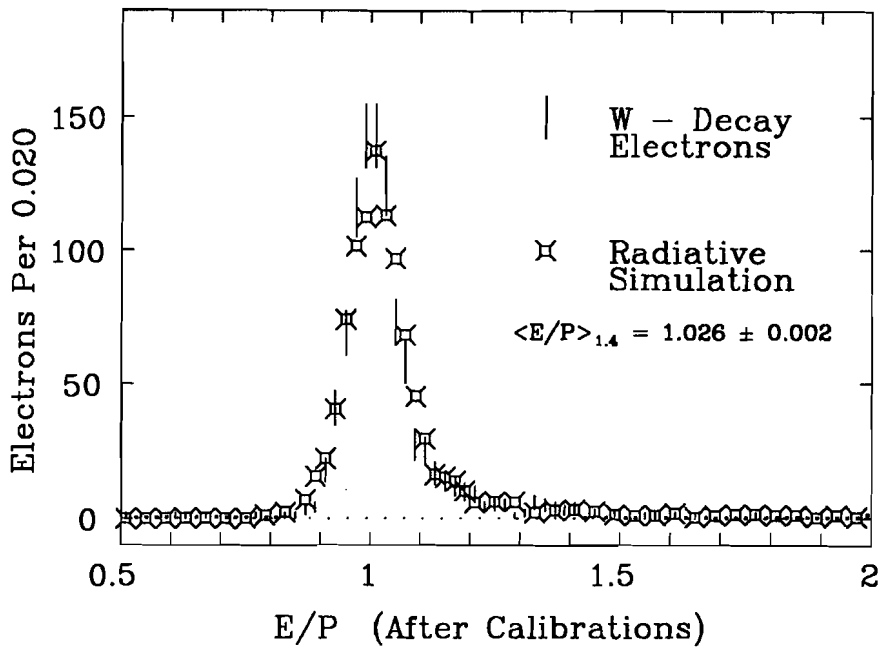

Figure 24: E/P of W electrons(after including CEM calibration)

tum because high energy electrons may radiate before reaching the calorimeter. The W decay may also have associated internal radiation. While the calorimeter measures most of the radiated photon energy, the tracking chamber measures only the momentum of the charged track. Thus, E/p$\geq$ 1 on average.

The simulation predicts a 2.6% shift in the mean E/p if the E/p distribution is truncated at 1.4(Fig. 24.) The truncation point is more than $5\sigma_{<E/p>}$ away from 1; this covers more than 99% dispersion of the E/p distribution coming from the measurement resolutions of CEM and CTC. To reproduce the 2.6% shift in the data requires a re-scaling all CEM energies by 1.01655(a 1.7% adjustment of the overall test beam calibration). The factor 1.01655 is the result of the following calculation:

$$1.01655 = \frac{1}{< \mathrm{E/p} >_{\mathrm{data}}} \times \frac{< \mathrm{E/p} >_{\substack{\text{Monte Carlo} \\ \text{radiation ON}}}}{< \mathrm{E/p} >_{\substack{\text{Monte Carlo} \\ \text{radiation OFF}}}} \tag{9}$$

The tracking chamber momentum scale is known to 0.2%. With a calibration sample of 1,100 W electron candidates the statistical E/p matching uncertainty is 0.23%. Studies of the simulation and radiative calculation, including the loss of photons in the magnet

coil and the amount of material present in front of the tracking chamber lead to 0.25% systematic uncertainty. Thus the overall systematic uncertainty on the energy scale is:

$$\sqrt{(0.20^2_{(tracking)} + 0.23^2_{(E/p\ stat.)} + 0.25^2_{(Rad.\ corrections)})} = 0.39\% \tag{10}$$

The electron energy leakage to the hadron calorimeter leads to an additional systematic uncertainty on the energy scale. In the W mass measurement the multiplication of the energy scale factor with the EM cluster energy implicitly corrects for the energy leakage to the hadron calorimeter. From the test beam measurement the energy leakage to the hadron calorimeter is:

$$Had/EM \sim 0.04 \times \frac{E}{100}, \tag{11}$$

where E is the energy measured in the electromagnetic calorimeter. By assuming an average 5 GeV energy difference between the decay electrons from Zs and Ws, it leads to 0.2% systematic uncertainty on the energy scale at the Z mass.

There is a further complication that fortunately cancels when the cluster energy is scaled. Some of the energy from the event underlying the W ends up in the same tower(s) as the electron being measured. On average 50 MeV ends up in each electromagnetic tower. This effect is on the order of .2% and cancels when the cluster energy gets multiplied by the energy scale.

An additional effect on the energy scale determination comes from the spread of the event z vertex. The response map calibration assumes an event vertex position value of z=0. Because the CDF detector is symmetric about z=0, and also the decay properties of electrons and positrons from Ws and Zs are symmetric about z=0, this effect averages out. This effect implicitly enters in the energy scale and cancels when the cluster energies are scaled. Since there is a lack of test beam data with off z=0 vertex, an estimate of the systematic uncertainty for this effect is not available. In the present CDF data the statistical fluctuation limits the accuracy of the Z mass measurement; the systematic

uncertainty from non-zero event vertex in z is not a crucial factor and may be implicitly part of 0.39% energy scale uncertainty.

4 Measuring the Z Mass and Width

I use the maximum likelihood method to determine the Z mass and width [20]. My goal is to keep the fitting procedure as straightforward as possible and at the same time to keep its systematics within the statistical fluctuation of the available data. In the maximum likelihood fit I use the relativistic Breit-Wigner function,

$$\frac{dN}{dm} = A\frac{m^2}{(m^2 - M_Z^2)^2 + (m^2\Gamma^2/M_Z)^2}, \tag{12}$$

as the probability distribution of the Z mass resonance, and convolute this with a Gaussian distribution to account for the measurement resolution of the CEM. The electroweak interference and the nonresonant Drell-Yan terms are not included in the fit. Given the available statistics and the $\Gamma/M_Z \sim 3\%$ ratio, the classical Breit-Wigner function,

$$\frac{dN}{dm} = A\frac{\Gamma/2}{(m - M_Z)^2 + (\Gamma/2)^2}, \tag{13}$$

gives an equivalent result compared to the expression with the energy dependent width. First I'll describe the fitting procedure and its systematics, next I'll give the details of further cuts to the Z sample and the results of fits for each step.

4.1 Fitting Procedure

4.1.1 Fitting algorithm

The fit results come from minimizing[21] the following likelihood function:

$$\log(L) = -\sum_{i=1}^{n} \log[p(m_i', \sigma_{m_i'}; M_Z, \Gamma)], \tag{14}$$

where $p(m_i', \sigma_{m_i'}; M_Z, \Gamma)$ is the probability of observing an event with measured mass m_i'. n is the number of events in the fit. The function $p(m_i', \sigma_{m_i'}; M_Z, \Gamma)$ is a convolution of relativistic Breit-Wigner and Gaussian distributions:

$$p(m_i', \sigma_{m_i'}; M_Z, \Gamma) = A_i(M_Z, \Gamma, \sigma_{m_i'}) \int_{m_i'-5\sigma_{m_i'}}^{m_i'+5\sigma_{m_i'}} e^{-\frac{1}{2}\left(\frac{m-m_i'}{\sigma_{m_i'}}\right)^2} \frac{m^2}{(m^2 - M_Z^2)^2 + (m^2\Gamma/M_Z)^2}\, dm. \tag{15}$$

The integration over m is carried out using the Romberg algorithm[22]; the result is accurate to one part in 10^6. The choice of the limits of integration covers more than 99.99% of the area of the Gaussian distribution, prevents machine accuracy from influencing the answer, and the integral is calculated within a reasonable time. The fitted width is correlated with the limits of integration; a narrower range of integration, say $m_i' \pm 2\sigma_{m_i'}$, gives a larger fitted width. For each event the normalization constant,

$$A_i^{-1}(M_Z, \Gamma, \sigma_{m_i'}) = \int_{81}^{101} p(m', \sigma_{m_i'}; M_Z, \Gamma)\, dm', \tag{16}$$

is calculated by integrating the event probability over the observed mass range; the range from which the events enter in the fit. The description of the mass range selection is given in section 4.1.5. The effective mass resolution, $\sigma_{m_i'}$, is the event weight in the fit. This weight is a function of measured energies and angles; the details of its calculation is given in section 4.1.3. The curve that is superimposed on the distribution of the observed masses is the sum of the probabilities of each measurement:

$$p(m') = \sum_{i=1}^{n} p(m', \sigma_{m_i'}; M_Z, \Gamma). \tag{17}$$

The calculation of the goodness of fit, χ^2, uses the expected number of events within a bin calculated from the sum of the probabilities and the bin contents of the observed invariant masses. The calculation treats the bin contents as Poisson distributed:

$$\chi^2 = \sum_{j=1}^{N} \frac{[p_j - q_j]^2}{q_j}, \tag{18}$$

where N is the number of bins, q_j is the number of entries for the j-th bin, and p_j is:

$$p_j = \int_{\text{j-th bin lower limit}}^{\text{j-th bin upper limit}} \sum_{j=1}^{n} p(m', \sigma_{m_i'}; M_Z, \Gamma)\, dm'. \tag{19}$$

4.1.2 Invariant mass calculation from measured quantities

The invariant mass calculation uses energies measured by the Central Electromagnetic Calorimeter and angles measured by the Central Tracking Chamber. The measured quantities are: energies $E_{1,2}$, and azimuthal angles $\phi_{1,2}$, and polar angles $\cot(\theta_{1,2})$. Neglecting the masses of the electron and the positron, the invariant mass in terms of the measured quantities is:

$$m^2 = 2E_1E_2[1 - \cos\theta_1 \cos\theta_2 - \sin\theta_1 \sin\theta_2 \cos(\phi_2 - \phi_1)]. \tag{20}$$

The average resolutions of the measured quantities are given in table 2. The contributions from the measured quantities to the average uncertainty of the invariant mass are:

$$\sigma_{E_{1,2}} = \frac{m}{2}\left[\left(\frac{\sigma_{E_1}}{E_1}\right)^2 + \left(\frac{\sigma_{E_2}}{E_2}\right)^2\right]^{1/2}$$

Table 2: Average resolutions of quantities measured by CEM and CTC

Detector	Measurement Resolution	Comments
CEM	$\left(\frac{\sigma_E}{E}\right)^2 = \left(\frac{13.5\%}{\sqrt{E\sin\theta}}\right)^2 + (2.4\%)^2$	Energy resolution in GeV
CTC	$\sigma_{p_t} = 0.0011 \times p_t^2$	Momentum resolution in GeV/c
	$\sigma_\phi = 3 \times 10^{-4}$	Azimuthal angle resolution in radians
	$\sigma_{\cot\theta} = 2.7 \times 10^{-3}$	Polar angle resolution

$$\sim 2.0 \text{ GeV}/c^2 \text{ (uncertainty on mass from energies)} \tag{21}$$

$$\sigma_{\phi_{1,2}} = \frac{m}{2}\left[\frac{\sin\theta_1\sin\theta_2\sin(\phi_2-\phi_1)}{1-\cos\theta_1\cos\theta_2-\sin\theta_1\sin\theta_2\cos(\phi_2-\phi_1)}\right]\left(\sigma_{\phi_1}^2+\sigma_{\phi_2}^2\right)^{1/2}$$

$$\sim 0.02 \text{ GeV}/c^2 \text{ (uncertainty on mass from azimuthal angles}(\phi)) \tag{22}$$

$$\sigma_{\theta_{1,2}} = \frac{m}{2}\left[\frac{[\sin\theta_1\cos\theta_2+\cos\theta_1\sin\theta_2\cos(\phi_2-\phi_1)]^2\,\sigma_{\theta_1}^2}{1-\cos\theta_1\cos\theta_2-\sin\theta_1\sin\theta_2\cos(\phi_2-\phi_1)} + \frac{[\cos\theta_1\sin\theta_2+\sin\theta_1\cos\theta_2\cos(\phi_2-\phi_1)]^2\,\sigma_{\theta_2}^2}{1-\cos\theta_1\cos\theta_2-\sin\theta_1\sin\theta_2\cos(\phi_2-\phi_1)}\right]^{1/2}$$

$$\sim 0.1 \text{ GeV}/c^2 \text{ (uncertainty on mass from polar angles}(\theta)) \tag{23}$$

where $\sigma_\theta = \sigma_{\cot\theta}/(1+\cot^2\theta)$. The uncertainty in the energy contributes most to the overall effective mass resolution. The angular measurement uncertainties are a factor 20 smaller, hence only the energy contribution is used to calculate the event weight.

4.1.3 Calculation of the effective mass resolution

The energies E_1, E_2, that enter in the invariant mass calculation have been corrected for the CEM tower to tower variations, and the position dependent response of the tower. Their energies are scaled using the result of the E/P calibration,

$$E_i^{\text{corrected}} = s\frac{E_i^{\text{measured}}}{r_i\ q_i}. \tag{24}$$

The uncertainty of the energy scale, s, is common to all EM clusters. This uncertainty is assigned to the energy scale systematics. The uncertainty of the position dependent

correction factor, r, depends on the tower in which the electron deposits its energy and on the location of the electron shower within that tower[15]. The uncertainty of the tower to tower variation correction factor, q, depends on the tower in which the electron deposits its energy. The overall measurement uncertainty of a CEM cluster energy is:

$$\left(\frac{\sigma_E}{E}\right)^2 = \left(\frac{13.5\%}{\sqrt{E\sin\theta}}\right)^2 + \sigma_r^2 + \sigma_q^2 \tag{25}$$

In the likelihood fit the above definition enters in the calculation of the effective mass resolution for each EM pair.

For 9 towers within a wedge, the average uncertainty of the response map correction is 1.5%. Figure 25 shows the geometrical categories, within a wedge, used by the authors in reference[15] to derive the response map correction and its uncertainty. The uncertainties at the tower boundaries are larger compared to the average uncertainty from 9 towers; these are categories, B, C, and D in Figure 25. These information are included in the calculation of the effective mass resolution. The average uncertainty of the tower to tower correction factor is 1.7%(Fig. 23). The quadrature sum, $b = \sqrt{(\sigma_r^2 + \sigma_q^2)}$, is the average tower to tower uncertainty of the CEM. The average value of b is 2.4%(Fig. 26).

The effective mass resolution is the convolution of the energy uncertainties, E_1, E_2:

$$\sigma_m = \frac{m}{2}\left[\left(\frac{\sigma_{E_1}}{E_1}\right)^2 + \left(\frac{\sigma_{E_2}}{E_2}\right)^2\right]^{1/2}. \tag{26}$$

The mean value of the effective mass resolution is 2.0 GeV/c^2 (Fig. 26).

4.1.4 Mass acceptance of Et and fiducial cuts

The effect of both the fiducial volume and the transverse energy cuts on the shape of the Z invariant mass distribution is checked using events generated by ISAJET(V6.22)[23]. My conclusions from these tests are based on $\sim 60,000$ $Z \rightarrow e^+e^-$ events. The rapidity

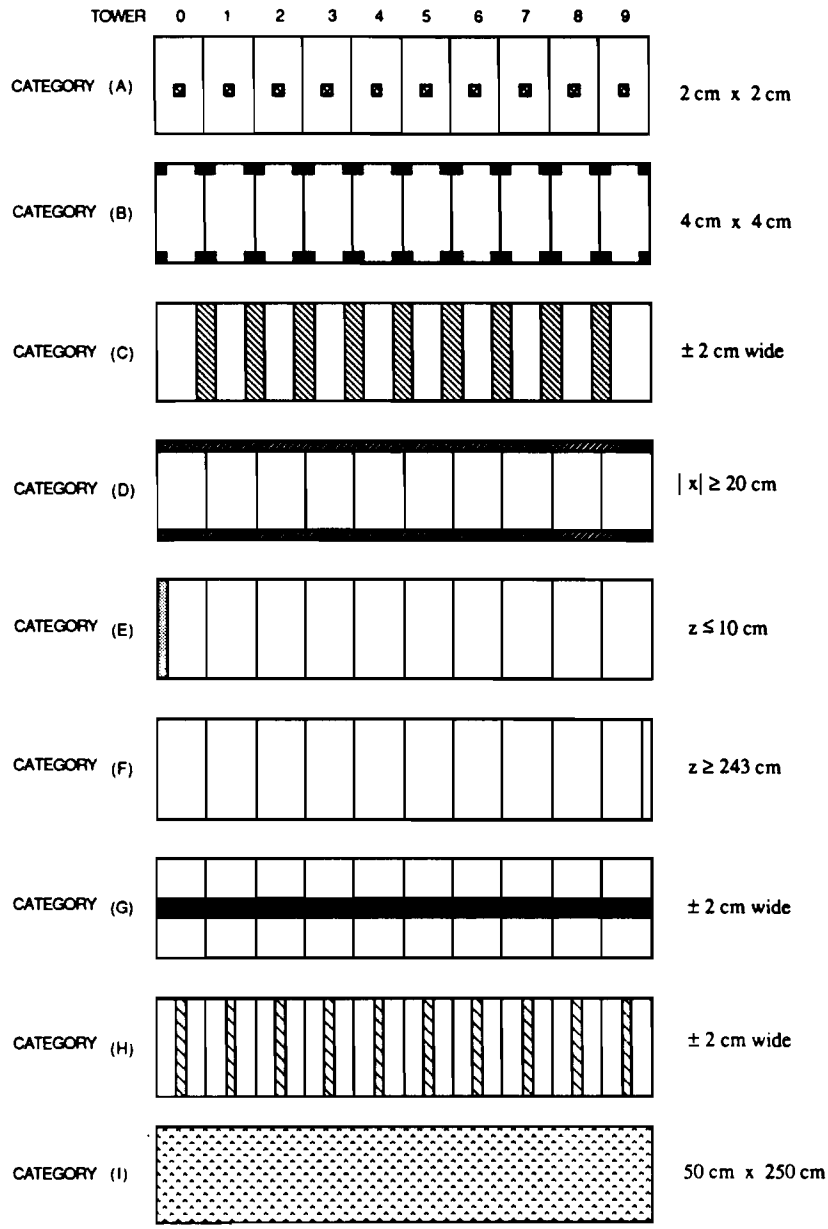

Figure 25: Classification of geometrical categories to test the response map correction reproducibility. The response map correction for categories B, C, and D have larger than average uncertainties. These are the tower edges. No CEM cluster from categories E and F enter in the Z mass and width analysis.

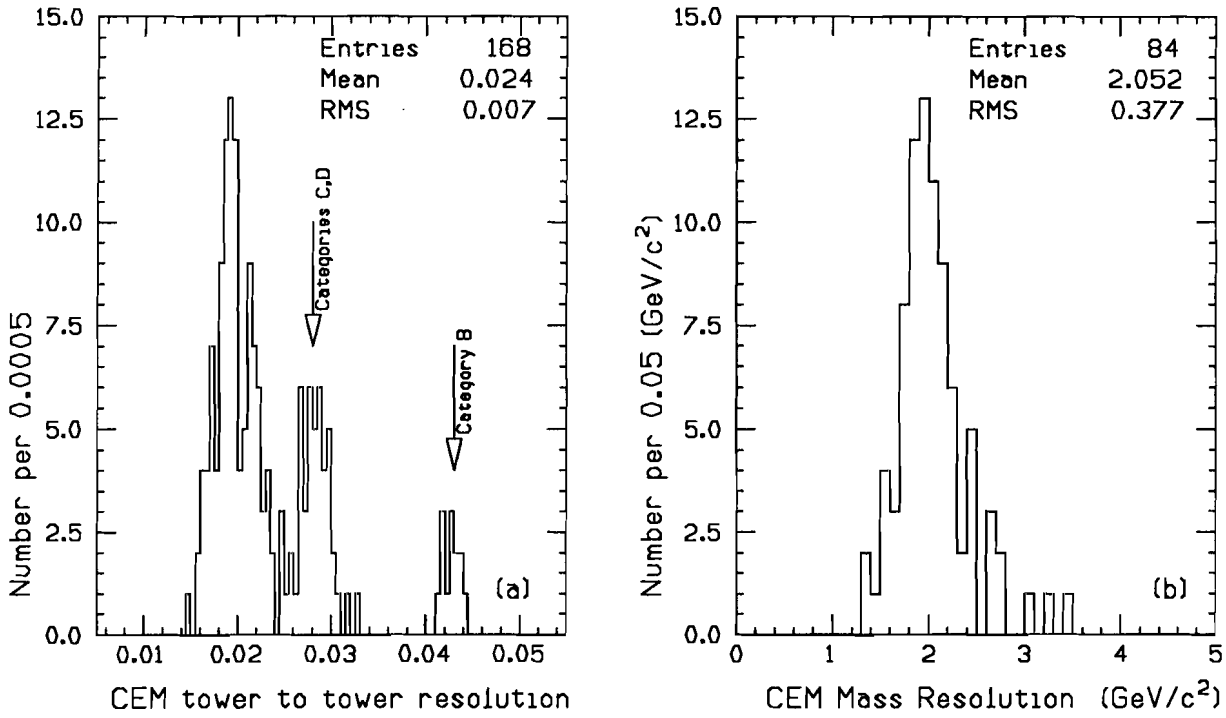

Figure 26: a) The CEM tower to tower resolution, b) The effective mass resolution. If the contributions from tower boundaries are not included, the average CEM tower to tower resolution is 2.0%. The effective mass resolution has a single peak, because the chances of both EM clusters having poor measurement resolution are small.

range of electrons and positrons from Z decays in Monte Carlo data is $|\eta| < 7.5$, where the fiducial cut in $\bar{p}p$ data is $|\eta| < 1$. First I'll describe the effect of the fiducial cut and afterwards the transverse energy cut.

The generated data is smeared with nominal CEM calorimeter resolution. The event vertex position in z is smeared to reflect the vertex spread in $\bar{p}p$ data. The shapes of the invariant mass distributions with and without fiducial cuts are the same. The Kolmogorov-Smirnov statistic[20], [22], test show both invariant mass distributions, with and without fiducial cuts, are identical with a 100% confidence level. Integral distributions are shown in figure 27. A lower Et cut of 20 GeV on electrons and positrons does not distort the invariant mass distribution. The fiducial cut in rapidity implicitly applies an E_t cut because of kinematics that enter in the invariant mass calculation. The E_t distributions with and without fiducial cuts are shown in figure 28. These distributions show that an Et cut of 20 GeV does not affect the shape of the Z invariant mass distribution.

Since the fiducial and the E_t cuts leave the invariant mass distribution unaffected, their effects are not included in the likelihood fits. The trigger acceptances(E_t, electronics, phototubes) and efficiency of each CEM cell are assumed to be identical and are not considered in the fit.

4.1.5 Fitted Mass Range Selection

Events that enter in the fit are selected from 81-101 GeV/c^2 mass range. This mass range is symmetric about the observed invariant mass distribution peak. With this choice more than 90% of Z candidates are selected to be used in the fit. A Monte-Carlo Z sample, where the electrons passed the fiducial and the E_t cuts, was prepared and each lepton was smeared with the nominal calorimeter resolution. The superposition of both generated and smeared mass distributions is shown in figure 29. The bin by bin difference of calorimeter smeared to ideal mass distribution is also shown. The dip in

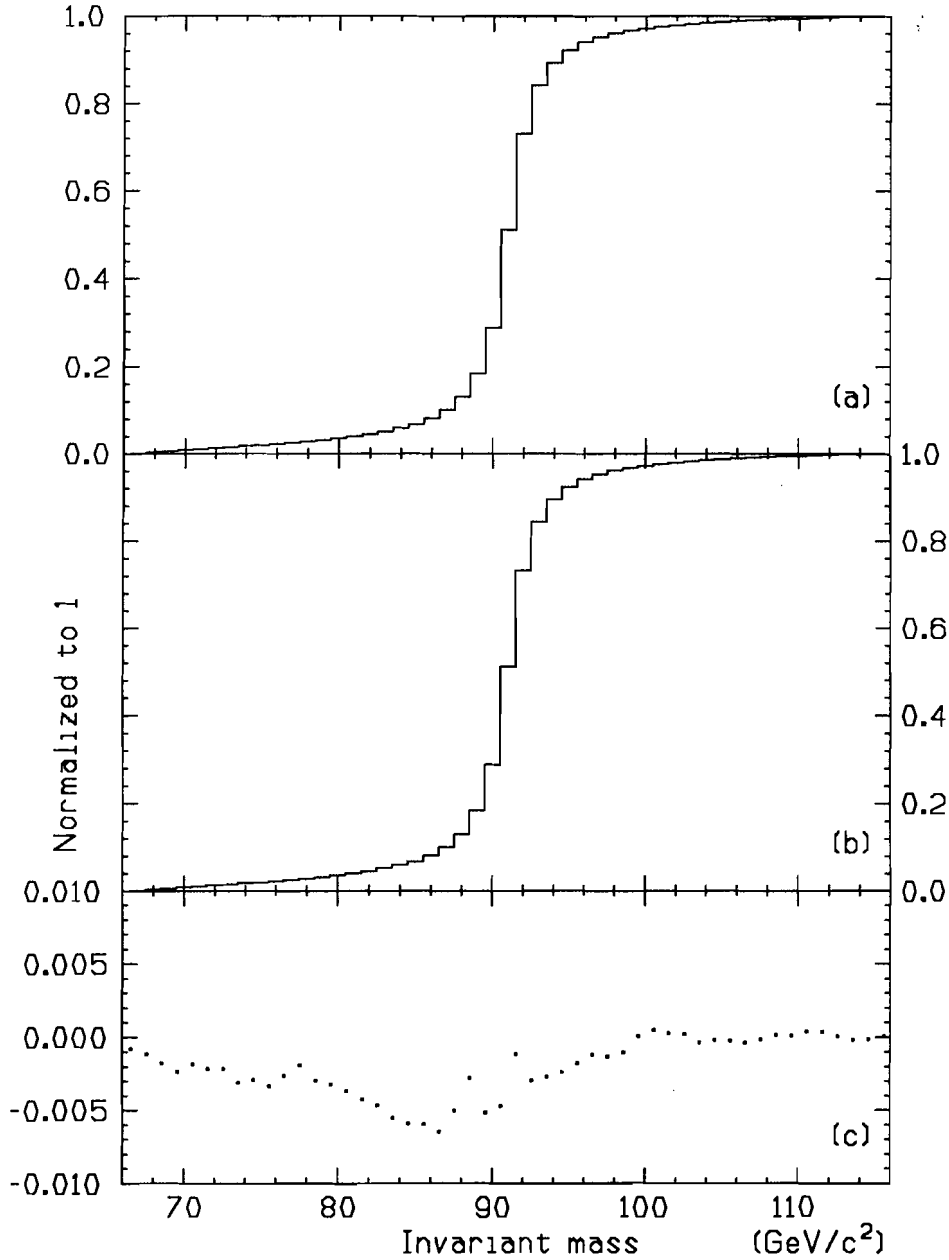

Figure 27: Integral distributions of Z invariant mass are shown in plots a and b. a) The generated distribution without cuts. b) Fiducial cut is applied. c) The difference of the plots a and b, (b-a). The invariant mass distributions are normalized for the mass range 66-116 GeV/c^2 . The plot in c is used to determine the confidence level of Kolmogorov-Smirnov statistic.

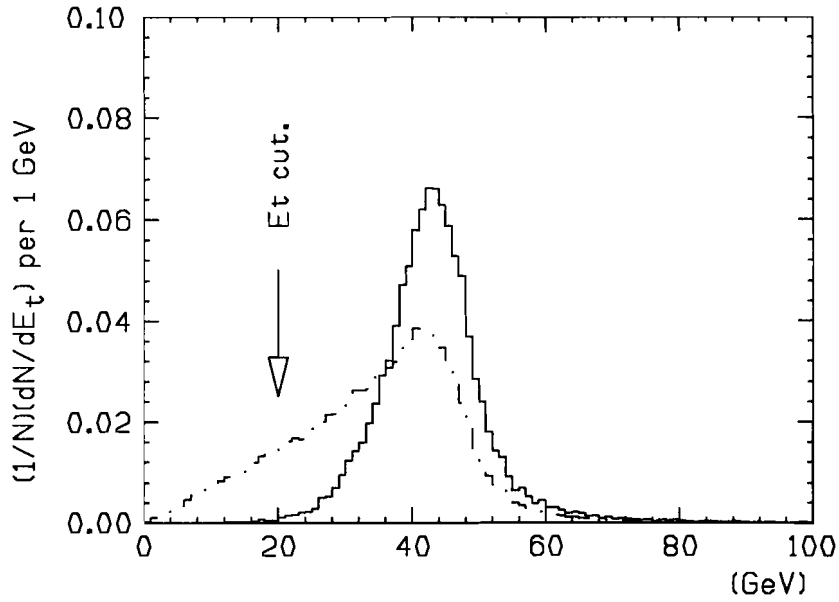

Figure 28: Transverse energy(Et) distributions of electrons and positrons from Z decays. The distribution with solid curve was prepared after an $|\eta| < 1.0$ cut. The dashed curve is the original distribution. The fiducial cut changes the shape of the Et distribution of electrons and positrons.

the difference plot indicates that, within the $M_Z \pm \Gamma_Z$ range, events are depleted due to resolution smearing. Beyond $M_Z \pm 3\Gamma_Z$ the effect is smaller, hence the difference is close to 0. The choice, $M_Z \pm 10$ GeV/c^2, selects about 92% of Z candidates. With the effective mass resolution due to the CEM calorimeter resolution of $\sigma_m = 2.0$ GeV/c^2, the mass range also satisfies the $5\sigma_m$ criteria assuming the spread of the invariant mass distribution arises primarily because of the calorimeter resolution.

The probability distributions used in the likelihood fits are normalized using the selected mass range limits. Since the mass window is symmetric about the Z resonance, the normalization constant has small effect on the mass value but is crucial in determining the width.

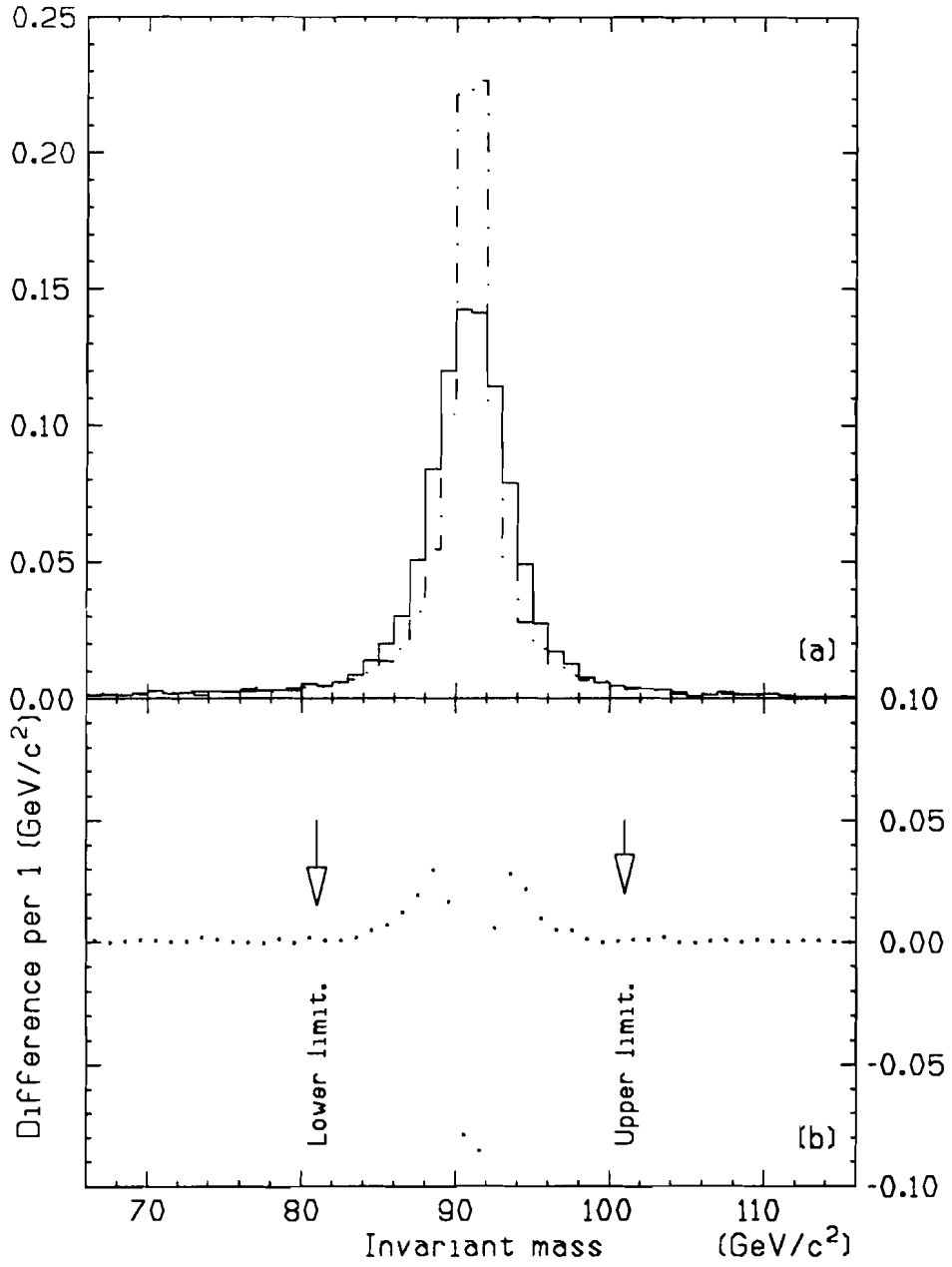

Figure 29: a) The superposition of ideal and smeared generated mass distributions. b) The difference of smeared to ideal mass distribution. The Z mass range was chosen based on plot b. Parameters used to generated these plots are : $M_Z = 91$ GeV/c^2 , $\Gamma_Z = 2.4$ GeV, and $\sigma_m = 2$ GeV/c^2 .

4.2 Fitting Systematics

4.2.1 Structure function contribution to the Z mass fit

A systematic effect of the fit comes from excluding the structure function contribution in the calculated probabilities. The Z mass distribution is skewed toward lower mass values by the dependence of the parton densities on the generated mass.

To keep the fitting procedure as simple as possible, the structure function contribution is not included when calculating probabilities. Instead, the results of several tests show the fitted mass is shifted by -80 ± 40 MeV/c^2. The uncertainty on this shift is from tests[24] of different structure functions: EHLQ-1[25], DO-1, DO-2[26], DFLM-2,DFLM-3[27]. To account for this shift, an 80 MeV/c^2 is added to the fitted Z mass from $\overline{p}p$ data. This mass shift is 5 times smaller compared to the statistical uncertainty of the Z mass, hence the fitting method is suitable to the determine the Z mass with the available statistics. The fitted mass range used for this study is 81-101 GeV, with the generated mass value of 91 GeV. No mass shift is observed by ignoring the nonresonant Drell-Yan and the electroweak interference effects in the fit.

By not including the structure function in the fit, the fitted width comes out broader by 100 MeV compared to the input value of 2.5 GeV. This effect is washed out by the 20 times larger energy measurement resolution. The statistical uncertainty of the Z width from the available Z sample, $\sim \pm 1$ GeV, is 10 times larger than the 100 MeV shift. The structure function contribution to the fit can be safely ignored. I consider this 100 MeV broadening as part of the Z width systematics.

4.2.2 QED radiative effect to the Z Mass

The QED radiative effect comes about because an instantaneously accelerated electron from rest to a speed β = v/c emits a photon with some probability. When a Z boson decays in its rest frame into e^+e^- pairs, the electron and positron each acquire

$\sim$ 45.5 GeV/c^2 energy and both are accelarated instantaneously from rest to a speed $\beta \sim 1$. If the photon makes a large angle with respect to the electron or the positron, the photon energy won't be deposited in the same CEM tower as the electron. With reduced cluster energy the calculated invariant mass value will be smaller. In the case of Z decays, the probability that at least one of the electrons emits a photon with energy greater than 100 MeV is around 60%. The CEM calorimeter does measure energies on the order of 100 MeV.

Monte Carlo studies show the fitted mass is shifted by -110 MeV/c^2 by not including the QED radiative corrections to the final state electrons in the probability calculation[28]. The Z$\rightarrow e^+e^-$ events were simulated with a Monte Carlo event generator which uses the exact matrix elements to order α^2[29]. Thus, 110 MeV is added to the fitted mass from $\bar{p}$p data. This shift is about a factor of 3 smaller compared to the Z mass statistical uncertainty. Hence the fitting procedure is suitable to estimate the Z mass with available statistics.

By not including the QED radiative corrections to leptons in the fit, the fitted Z width from Monte Carlo is broadened by 200 MeV. This effect is washed out by the 10 times larger energy measurement resolution. The statistical uncertainty of the Z width from the available Z sample is 5 times larger than the 200 MeV shift. The QED radiative corrections to leptons are safely ignored in the fit, the 200 MeV braodening is treated as part of the Z width systematics.

In the external bremsstrahlung, caused by the electrons passing through the detector, the emitted photon is collinear with the electron and its energy is deposited in the calorimeter and becomes part of the electromagnetic (EM) cluster energy. The effect of large angle external bremsstrahlung is assumed to be small compared to the QED radiative corrections and is not included in the fit.

4.3 Fitting the $\bar{p}p$ Z data

Having described the details of the fitting method and its systematics, I now use this method to fit the Z $\rightarrow e^+e^-$ candidates. Table 3 contains the fitted results of the Z mass and width for different cuts. The QED radiative and the structure function contributions are not included in the displayed results. The fitted results for the di-electron sample(section 3.1), category A, is consistent with the results from Z sample with tighter cuts: categories B, C, D, E and F. The presence of background in the sample of category A broadens the fitted width. The fitted mass from the di-electron sample agrees within 100 MeV/c^2 with the results from Z samples. In the di-electron sample there are 3 like sign pairs within 81-101 GeV/c^2 range. There are no like sign events in the samples of the remaining categories.

The cut on the ratio of the electromagnetic energy to momentum, E/P$\leq$ 2, is intentionally kept loose at the event selection stage. In category B, both clusters of an EM pair are made to pass the inclusive electron cuts. The application of the same cuts on both clusters prevents unknown energy scale systematics. The CEM energy scale is determined from W$\rightarrow e\nu$ electron sample where the electrons pass an E/P$\leq$ 1.4 cut. The category C is the sample with E/P$\leq$ 1.4 cut. The fitted results of categories B and C are consistent with one another. I'll use the results of category C to quote the Z mass and width. There is no background contribution to the Z mass measurement, in the central region of the detector, from other physics processes [30]. In the Z mass analysis stricter cuts are applied to both EM clusters compared to the Z cross section analysis[17], [30]; where the background under the Z mass resonance is estimated to be $< 1\%$.

Up to this stage of this analysis I have not used CES χ^2 information; this information is as good as the E/P cut to identify electrons and to reject backgrounds. To further check on the presence of background, I have applied CES $\chi^2_{avg.}$, where $\chi^2_{avg.} = (\chi^2_{strip} + \chi^2_{wire})/2$, cut to the Z sample of category C. Categories D,E and F in table 3 show the results of the CES $\chi^2_{avg.}$ cut; this χ^2 is for 9 degrees of freedom. Up to 4 events are rejected compared

Table 3: The fitted values of the Z mass and width. The QED radiative and the structure function corrections are not included in these values. The number of events within 50-150 GeV/c^2 range are listed under the 'Cuts category'. Events in a fit are selected from 81-101 GeV/c^2 . A) One of the EM cluster passes the inclusive electron cuts, where the second cluster passes a HAD/EM<0.1 cut and there is a 3D track pointing at it. B) Both EM clusters pass the inclusive electron cuts. The E/P ratio is less than 2. C) Both EM clusters pass the inclusive electron cuts. The E/P ratio is less than 1.4. D) In addition to cuts in C, both clusters pass CES $\chi^2_{avg.} \leq 20$ cut. E) In addition to cuts in C, both clusters pass CES $\chi^2_{avg.} \leq 16$ cut. F) In addition to cuts in C, both clusters pass CES $\chi^2_{avg.} \leq 10$ cut. G) In addition to cuts in C, both clusters pass CES $\chi^2 \leq 10$ cut for each $r\phi$ and z views. Where $\chi^2_{avg.} = (\chi^2_{strip} + \chi^2_{wire})/2$.

Cuts category	Mass(GeV/c^2)	Width(GeV)	χ^2_{dof}	Number of events used in fit
A/213 events	$90.63 \pm^{0.36}_{0.37}$	$3.90 \pm^{1.03}_{0.84}$	29.0/18	114
B/90 events	$90.53 \pm^{0.38}_{0.39}$	$2.90 \pm^{0.99}_{0.78}$	18.0/18	79
C/83 events	$90.59 \pm^{0.39}_{0.40}$	$2.76 \pm^{1.00}_{0.78}$	23.5/18	72
D/81 events	90.69 ± 0.380	$2.47 \pm^{0.91}_{0.75}$	26.5/18	70
E/80 events	90.69 ± 0.380	$2.47 \pm^{0.91}_{0.75}$	26.5/18	70
F/79 events	$90.72 \pm^{0.39}_{0.38}$	$2.52 \pm^{0.94}_{0.76}$	25.4/18	69
G/66 events	$91.03 \pm^{0.42}_{0.42}$	$2.59 \pm^{1.06}_{0.82}$	20.7/18	58

with category C. A visual inspection shows these are Z candidates where the radiated photon is close to the electron shower; the closeness of both showers gave larger χ^2 values. The fitted masses of categories D,E and F are consistent with the result from category C. The mass shift among different categories is due to the statistical fluctuation in fitted samples. The results of a tighter CES χ^2 cut is given in category G. The fitted mass is larger by 0.44 GeV/c^2 compared to the fitted mass in category C. This result reflects the use of improper energy scale; there is no CES χ^2 cut in the energy scale calibration. This tighter cut rejects Z candidates where the radiated photons from electrons are physically close to the electron showers, thus resulting in larger CES χ^2 values.

The fitting algorithm is tested to check for systematics on the fitted results. Fits are performed on 72 events per sample for total of 200 samples. Each sample is selected from

a Gaussian convoluted Breit-Wigner distribution with an average Gaussian resolution of 2.05 GeV/c^2 ; about 20,000 events are generated with Breit-Wigner mass and width values of 91 GeV/c^2 and 2.5 GeV. Figures 30a,c show the distributions of fitted mass and width from Monte Carlo generated samples; the mean values of mass and width agree with the input values. The r.m.s. values of these distributions reflect the measurement uncertainties of mass and width for 72 events. These agree with the fit uncertainties from $\bar{p}p$ data. The mean values of the uncertainties on the mass and width(Fig. 30b,d) agree with the r.m.s. values of figures 30a,c; this result is expected. The statistical uncertainty of the width is asymmetric; the absolute values of positive and negative uncertainties about the fitted width are different. This asymmetrical nature comes about because both the width and the effective mass resolution are inversely proportional to the normalization constant. In figures 30c,d I have histogrammed the average quantities of positive and negative uncertainties. The statistical uncertainties of the fitted results in $\bar{p}p$ sample agree with the results from Monte Carlo studies[31].

The statistical uncertainties of the fitted results, in Monte Carlo study, shows dependence on the fitted width. This dependence is expected since the spread of a probability distribution is by definition used to determine the uncertainty of its parameters[32],[20]. The statistical uncertainty of the location parameter, M_Z, in a Breit-Wigner distribution is $\Gamma/\sqrt{2N}$, and the statistical uncertainty of the scale parameter, Γ, is $\sim \Gamma/\sqrt{N/2}$. Both uncertainties are proportional to the width of the Breit-Wigner distribution. Similarly, the statistical uncertainty of the scale parameter, σ, in a Gaussian distribution is $\sigma/\sqrt{2N}$. These are valid in the limit of infinite events, N. The dependence of the statistical uncertainties on the fitted width is shown in figures 31a,b. These uncertainty bands will shift upward, in the plot, if the resolution value is greater than 2.05 GeV/c^2 ; downward if the resolution is less than 2.05 GeV/c^2 . The agreement between the fitted results from $\bar{p}p$ data, category C sample, and the Monte Carlo is excellent. This is expected since the vertical location of the uncertainty bands is determined by the measurement

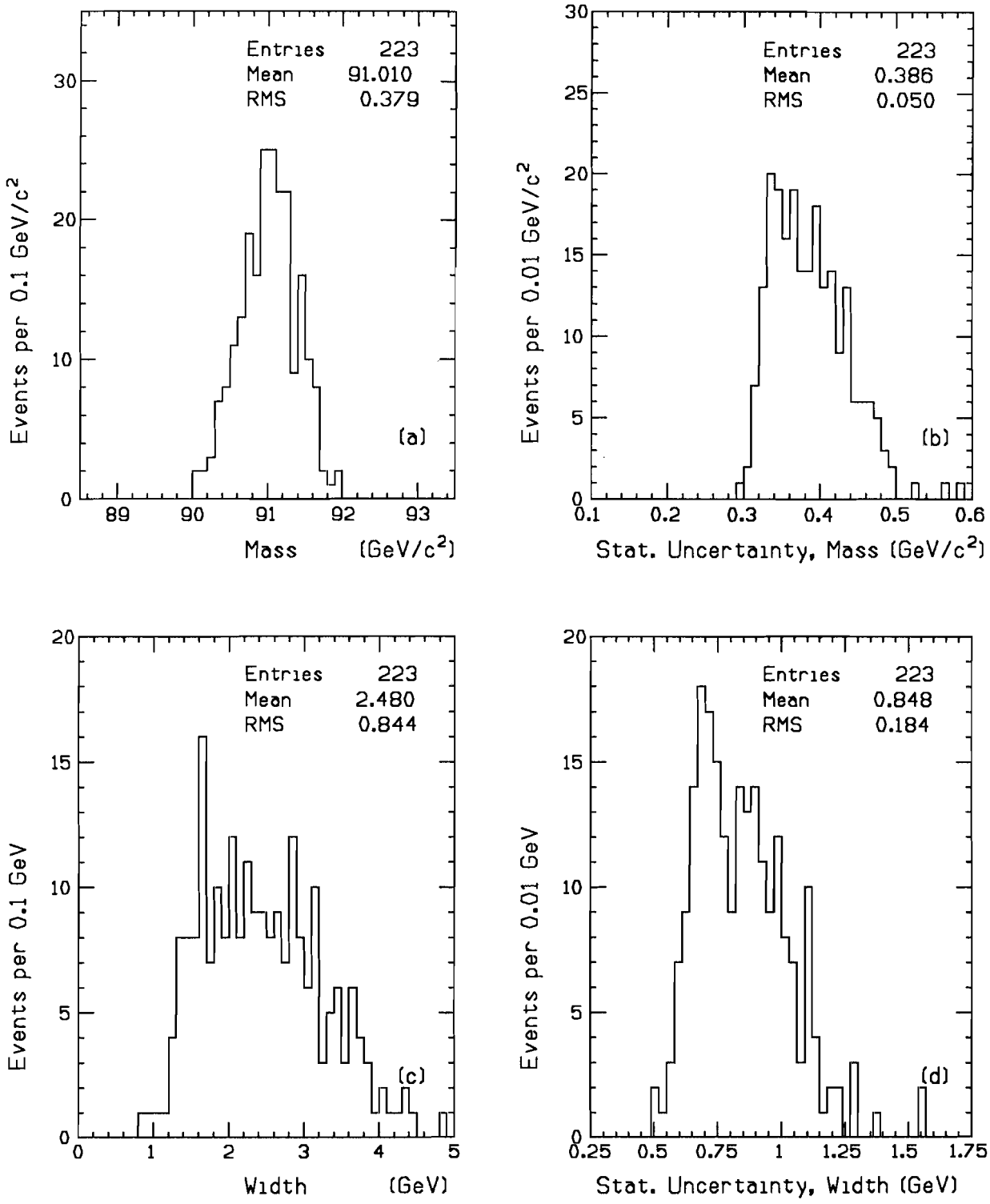

Figure 30: Results of tests on fitting code. The input parameters are: M = 91.0, $\Gamma = 2.5$, and $\sigma = 2.05$. a) Fitted mass. b) Uncertainty on the fitted mass. c) Fitted Width. d) Uncertainty on the fitted width. The mean values of the statistical uncertainties(Histogram b,d) agree well with the r.m.s. values of mass and width distributions(Histogram a,c).

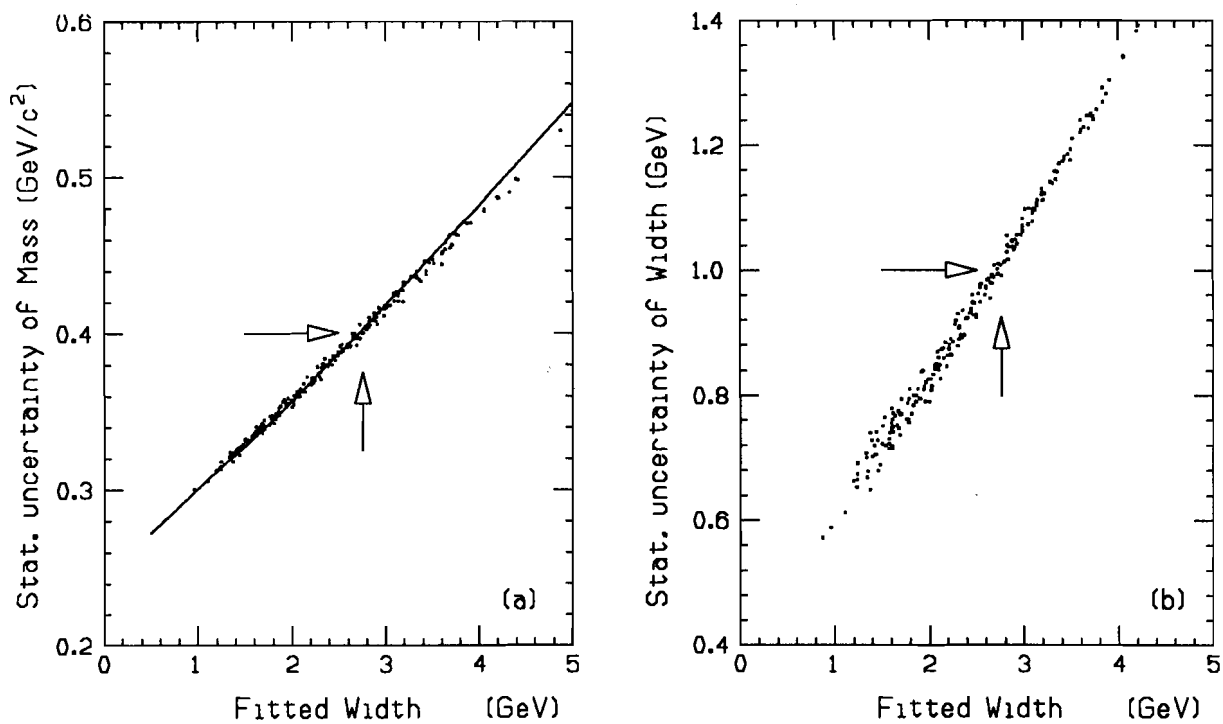

Figure 31: The dependence of statistical uncertainty of mass and width on the fitted width. I have only plotted the positive uncertainies of the fitted width. The arrows indicate the fitted results from Z$\rightarrow e^+e^-$ from $\overline{p}$p data. The agreement is excellent.

resolution used in the fit. This is yet another check that the fitting algorithm works; this also indicates the quoted uncertainties on the Z mass and width are consistent with expectation. The fitted width and the measurement resolution are correlated. In case the wrong measurement resolution is used in the fit, the fitted width will compensate for the wrong value by having different than its nominal value.

The fitted Z mass and width from $\overline{p}$p data are listed in table 4 with their statistical and systematic uncertainties. The quoted statistical uncertainty is the largest of either positive or negative uncertainties in table 3. The likelihood functions in each mass and width parameter space are shown in figure 32. Each of these functions has one maximum and both are well behaved. The likelihood function dependence of the mass is symmetric about its maxima; where as the likelihood function of the width is asymmetric about its maxima. The fitted mass and width are weakly correlated(Fig. 33), hence less than

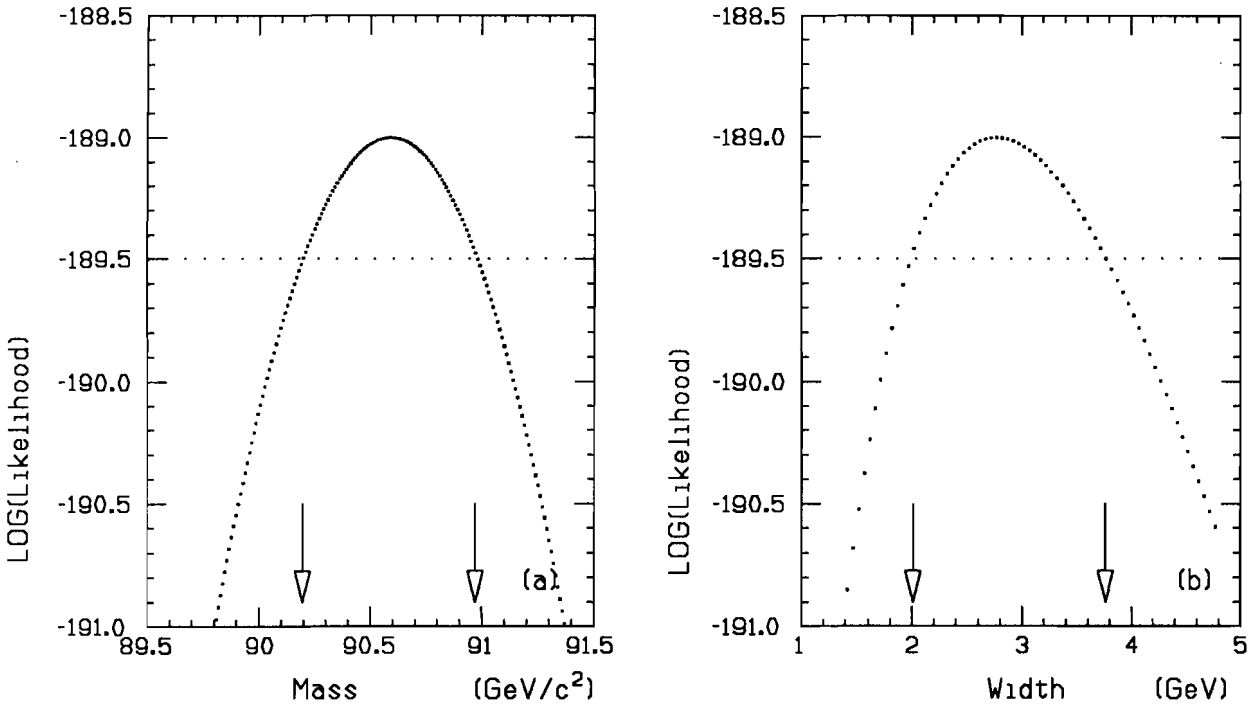

Figure 32: Likelihood functions for a) Mass and b) Width. The dotted horizontal line shows 1σ level, and the arrows their corresponding mass or width values.

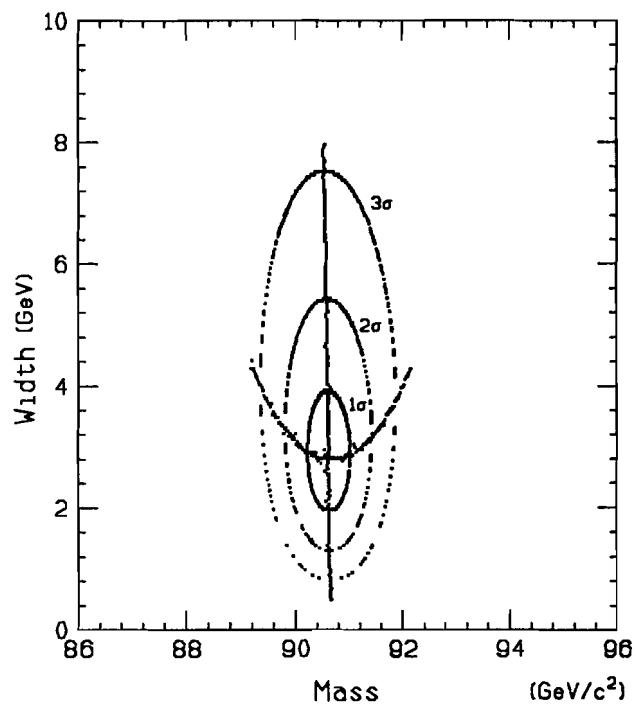

Figure 33: Z mass and width contour plot. The QED and structure function corrections to the mass are not included. The line (in the vertical direction) shows how far from the optimum value the fitted mass will be if the width is fixed to a wrong value. The parabola shows how wrong the fitted width will be if the mass is fixed. Near the optimum values, the mass and width are weakly correlated.

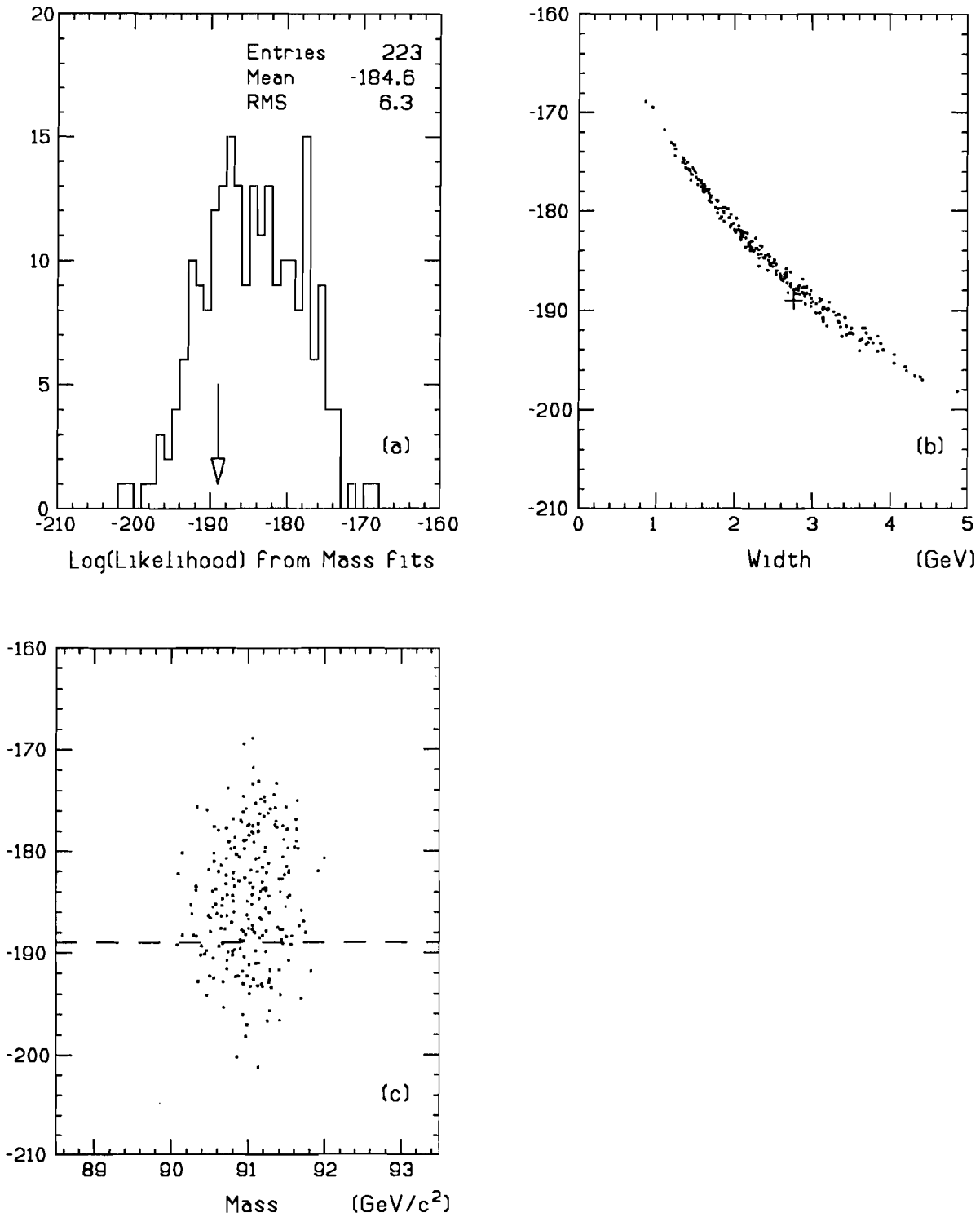

Figure 34: Log(Likelihood) distribution from fitting code tests. a) The arrow indicates the log(likelihood) value from $\overline{p}p$ data, b) The cross indicates the $\overline{p}p$ results. c) The fitted mass and the log(likelihood) are not strongly correlated.

Table 4: Corrections and uncertainties in the Z mass and width. The first uncertainty is statistical and the second systematic.

	Mass(GeV/c^2)		Width(GeV)
Observed fitted results	90.59 ± 0.40		2.8 ± 1.0
Radiative corrections	+0.11	± 0.03	±0.2
Structure functions	+0.08	± 0.03	±0.1
E/P calibration		±0.38	±0.0
CEM resolution uncertainty		±0.03	±0.5
Mass scale		±0.20	±0.0
Corrected results	90.78 ± 0.40 ± 0.43		.2.8 ± 1.0 ± 0.5

1σ fluctuation of one parameter has a negligible impact on the second parameter. The goodness of fit χ^2 test of 23.5/18$\sim$ 1.3 indicates the choice of the probability distribution very well models the behavior of the observed invariant mass distribution. This test is bin dependent, the χ^2 value depends on both the location and the size of histogram bin. A bin independent check[33] is to compare the log(likelihood) value from $\overline{p}$p data to that of the Monte Carlo. This test does not assign any confidence level, but gross inconsistencies can be easily observed. Monte Carlo test shows the log(likelihood) value and the fitted width are correlated(Fig. 34b); there is no correlation between the fitted mass and the log(likelihood) value(Fig. 34c). The log(likelihood) value from $\overline{p}$p fit is -189.00, this is a dimensionless quantity. This log(likelihood) value and the fitted width from $\overline{p}$p data are in excellent agreement with the Monte Carlo behavior(Fig. 34a,b).

The statistical uncertainty of the E/P calibration is the dominant source of systematic uncertainty on the measured Z mass. With the exception of the overall mass scale from momentum measurement, the rest of systematics on the measured mass are small. Since the CEM detector resolution is correlated with the fitted width, the uncertainty on this resolution is a source of systematic uncertainty on the width measurement. I assume an exaggerated error of 20% on the CEM resolution; the fitted mass varies by .03 GeV/c^2

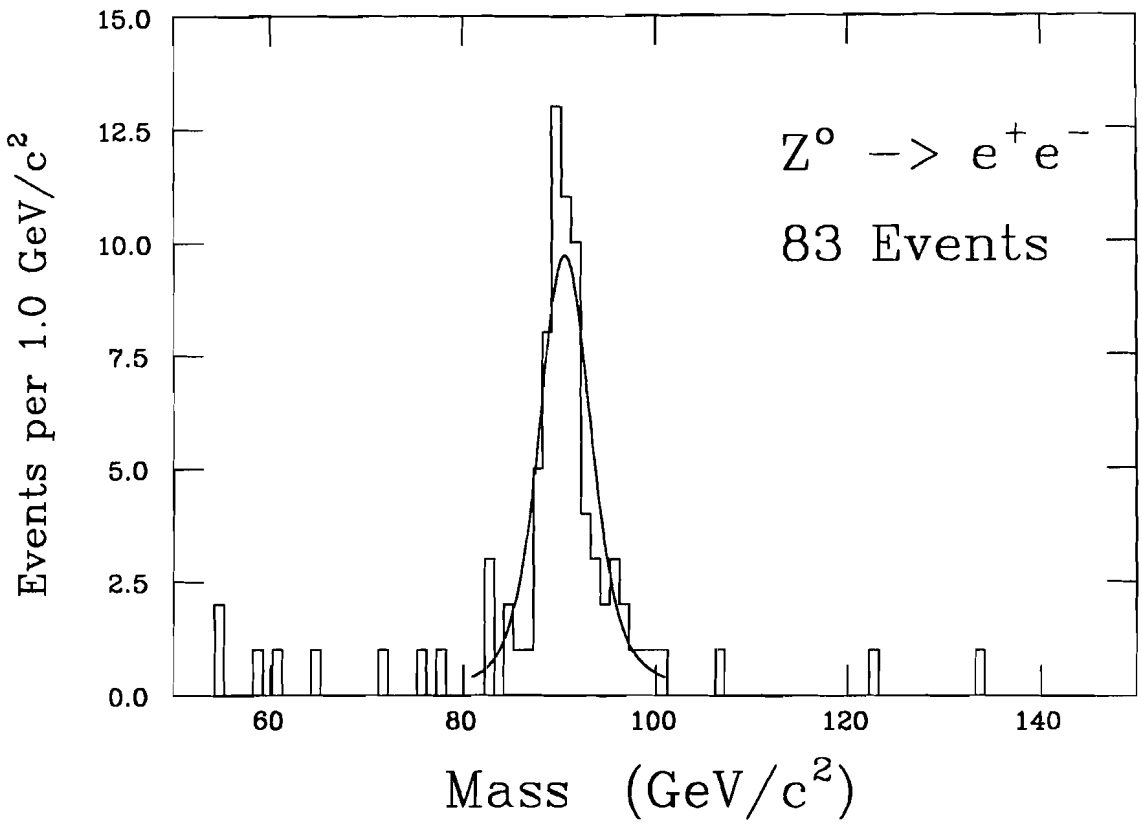

Figure 35: Z mass using calorimeter information.

and the fitted width varies by 0.44 GeV. The other systematics on the fitted width are from the QED radiative and the structure function effects. By adding the uncertainties in quadrature, the fitted mass and width values measured from 1988-1989 CDF's collider data are:

$$M_Z = 90.78 \pm 0.40(\text{stat.}) \pm 0.38(\text{syst.}) \pm 0.20(\text{scale}) \tag{27}$$

$$\Gamma = 2.8 \pm 1.0(\text{stat.}) \pm 0.5(\text{syst.}) \tag{28}$$

Given the statistical and the systematic errors, the Z mass and width are in excellent agreement with measurements from e^+e^- colliders[34]. The Z mass distribution is shown in figure 35.

5 Results and Future Prospects

The measured Z mass at the Tevatron tests the standard electroweak theory at the level of radiative corrections. This measurement can be explained by the quantized version of the theory. The theory predicts the Z mass value of 88.5 ± 0.8 GeV/c^2 in the lowest order calculation; where the measured mass, at the Tevatron, CERN, SLC, and LEP, is three standard deviations away from prediction.

The measured Z width at the Tevatron indicates the calorimeter energy measurements are understood within their uncertainties. The uncertainty on the measured width is larger than one neutrino contribution to the Z width, hence the measured width cannot be used to determine the number of generations in the context of the standard electroweak theory. From e^+e^- colliders, SLC and LEP, the measured Z width is 2.59 ± 0.07 GeV. The lowest order prediction from theory is ~ 2.5 GeV[5].

Two more input parameters are yet to be determined in the electroweak theory, W and Higgs masses. The W mass measurement is underway at the Tevatron by the CDF collaboration; a preliminary measured W mass is 79.8 ± 0.44 GeV/c^2 . A previous precise measurement of W mass is by the UA2 collaboration at CERN, with measured value of 80.4 ± 0.4 GeV/c^2 . By measuring both W and Z masses using the same detector, the measurement systematics will be common to both and cancel in the mass ratio. This fact coupled with the factor of 10 - 100 increase in data will make it possible to measure the W mass to 200-100 MeV/c^2. At this level of measurement uncertainty it will be possible to set stricter limit on the top quark mass or discover it. Figure 36 shows how W, Z, and top masses are correlated. On the plot the world average Z mass value is marked. The CDF Z mass measurement agrees within the statistics with the world average value. The CDF's preliminary, $M_Z - M_W$, mass difference is indicated on the plot. This plot shows the need to achieve 100 MeV/c^2 uncertainty on the W mass to make a profound statement about the top mass. At the present time the Z mass value is measured to a precision

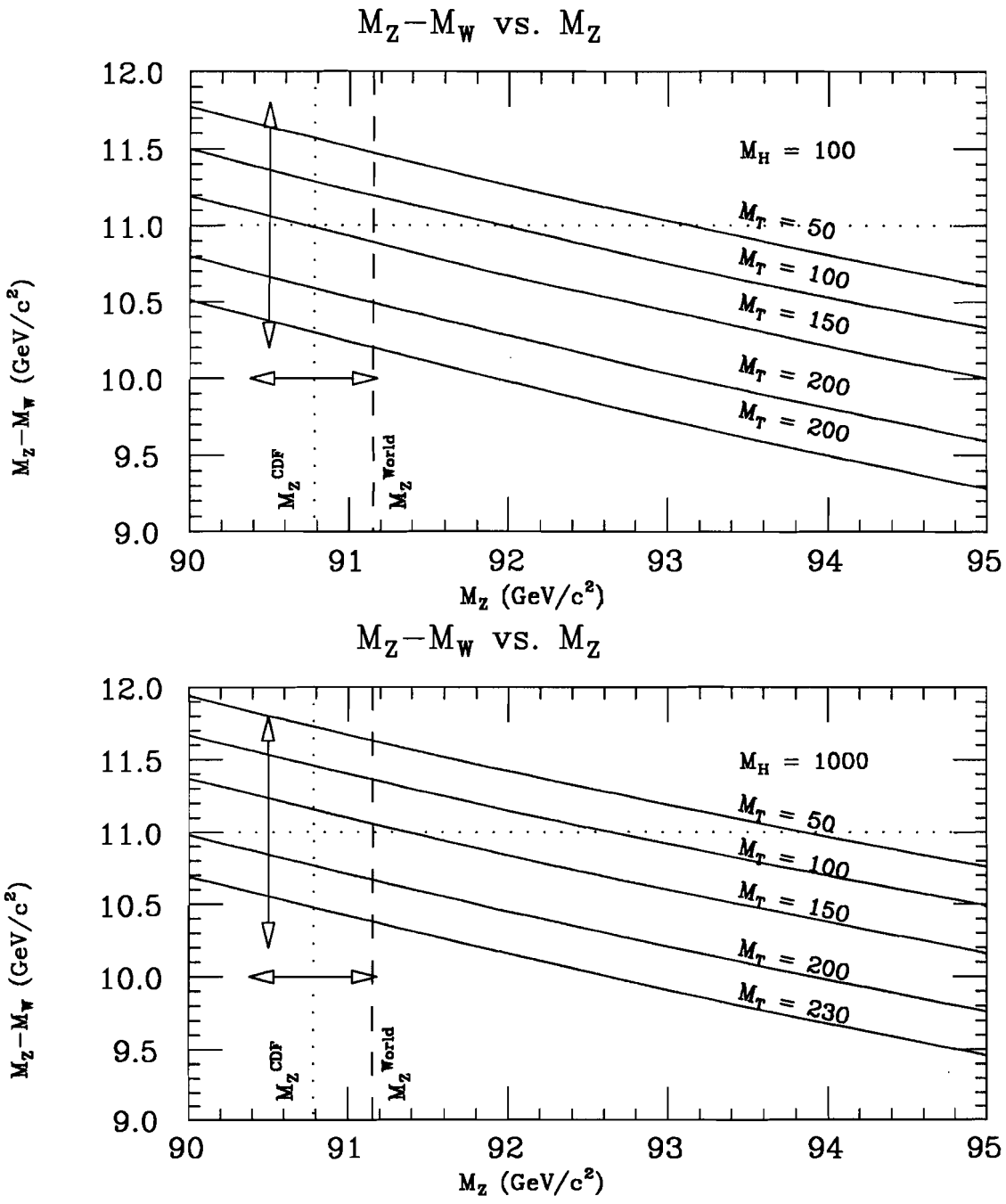

Figure 36: The interdependence of W, Z, and top masses for Higgs masses of 100 GeV/c^2 and 1000 GeV/c^2 . A preliminary estimate of the W and Z mass difference is shown. The length of the arrows is the statistical uncertainties.

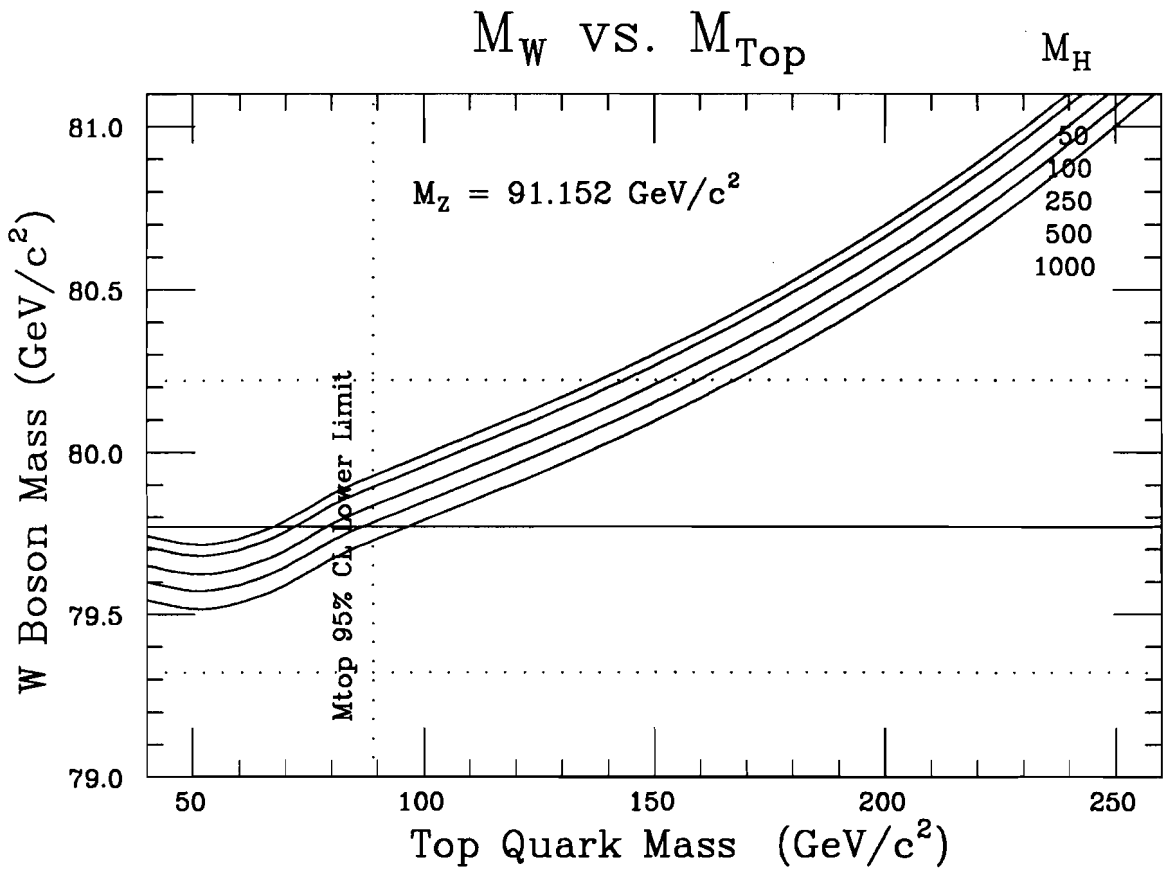

Figure 37: W mass vs. top quark mass plot. The interdependence of W, top, and Higgs masses is displayed.

of ~ 50 MeV/c^2 in e^+e^- colliders. The interdependence of W, top quark, and the Higgs masses(Fig. 37) can be seen for a fixed Z mass value. The CDF's preliminary W mass measurement is indicated on the plot in figure 37 . It is clear that the uncertainty on the W mass does allow a broad range of top quark masses. A lower limit on the top mass is 89 GeV/c^2 ; this is from direct searches by the CDF collaboration. With 25 times more data, $\sim 125\text{pb}^{-1}$, the Z mass statistical uncertainty measured at the Tevatron will be less than 100 MeV/c^2. This implies the W mass can be measured to about the same accuracy as the Z mass; I'm assuming the systematics of the W and Z mass measurements cancel. This measurement can be accomplished in 1993 before the W mass is measured at LEPII in 1995. If in 1993 the top quark mass is measured, the CDF collaboration will be able to directly start probing the Higgs sector of the standard electroweak theory. More data are needed! The hardware exists and its measurement ability exceeds the design goal.

A Z → e+e− Event Display

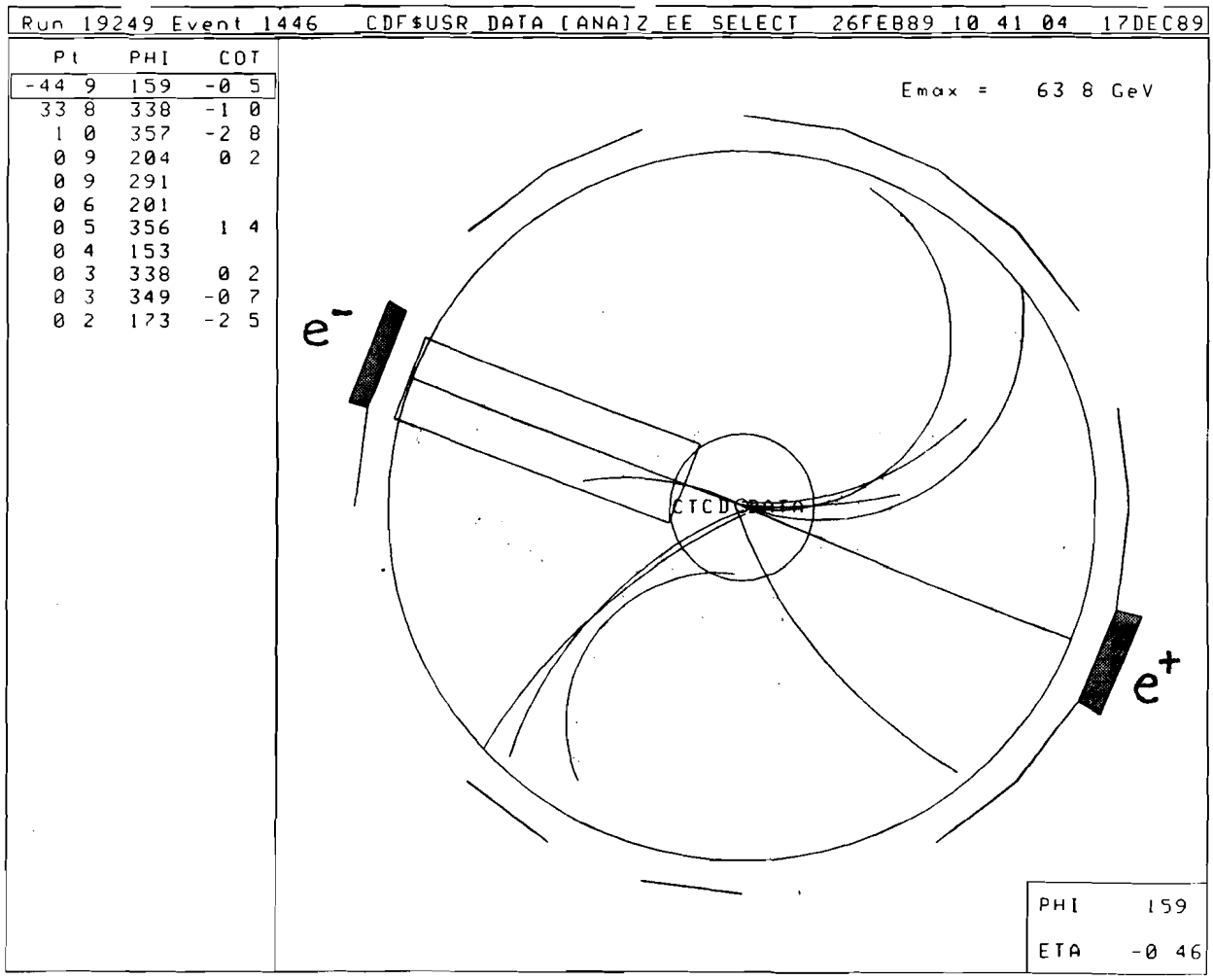

Figure 38: CTC display of Z→ e^+e^- candidate in a $\overline{p}p$ collision. The electron direction in xy plane is at $\phi = 159$ degrees, and the positron direction is at $\phi = 338$ degrees. The list on the left gives complete information about tracks. The negative value of p_t indicates negatively charged track. The outermost rectangles at the end of electron and positron shows the EM calorimeter energy. The combination of two quantities, momentum and energy, verify the particle as electron or positron.

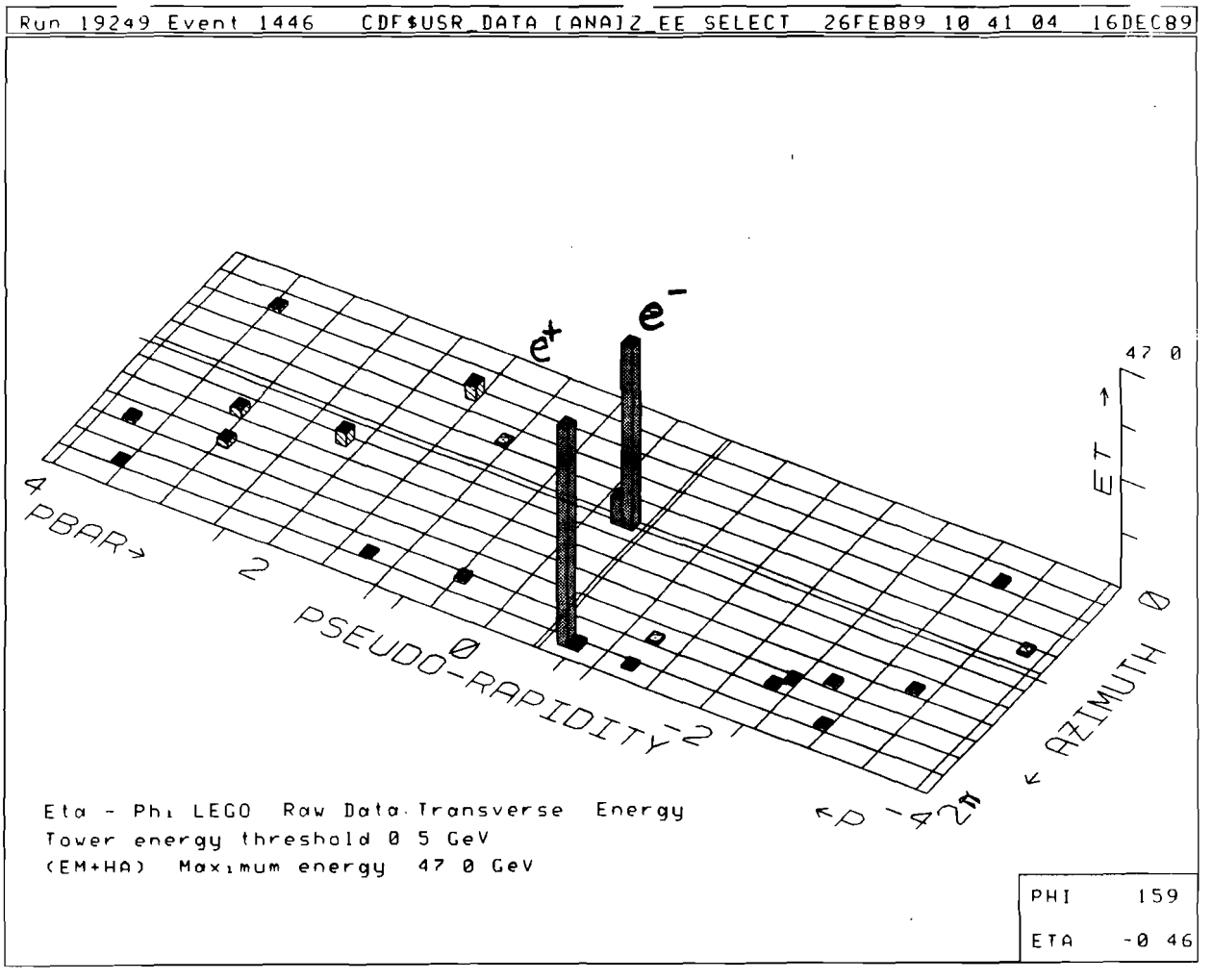

Figure 39: Calorimeter display of Z→ e^+e^- candidate in a $\bar{p}p$ collision. The transverse energies of the electron and the positron clearly stand out of the background energies. The central region of the detector is $\eta \leq \pm 1.1$ in pseudo-rapidity. The directions of incoming protons and anti-protons are also shown.

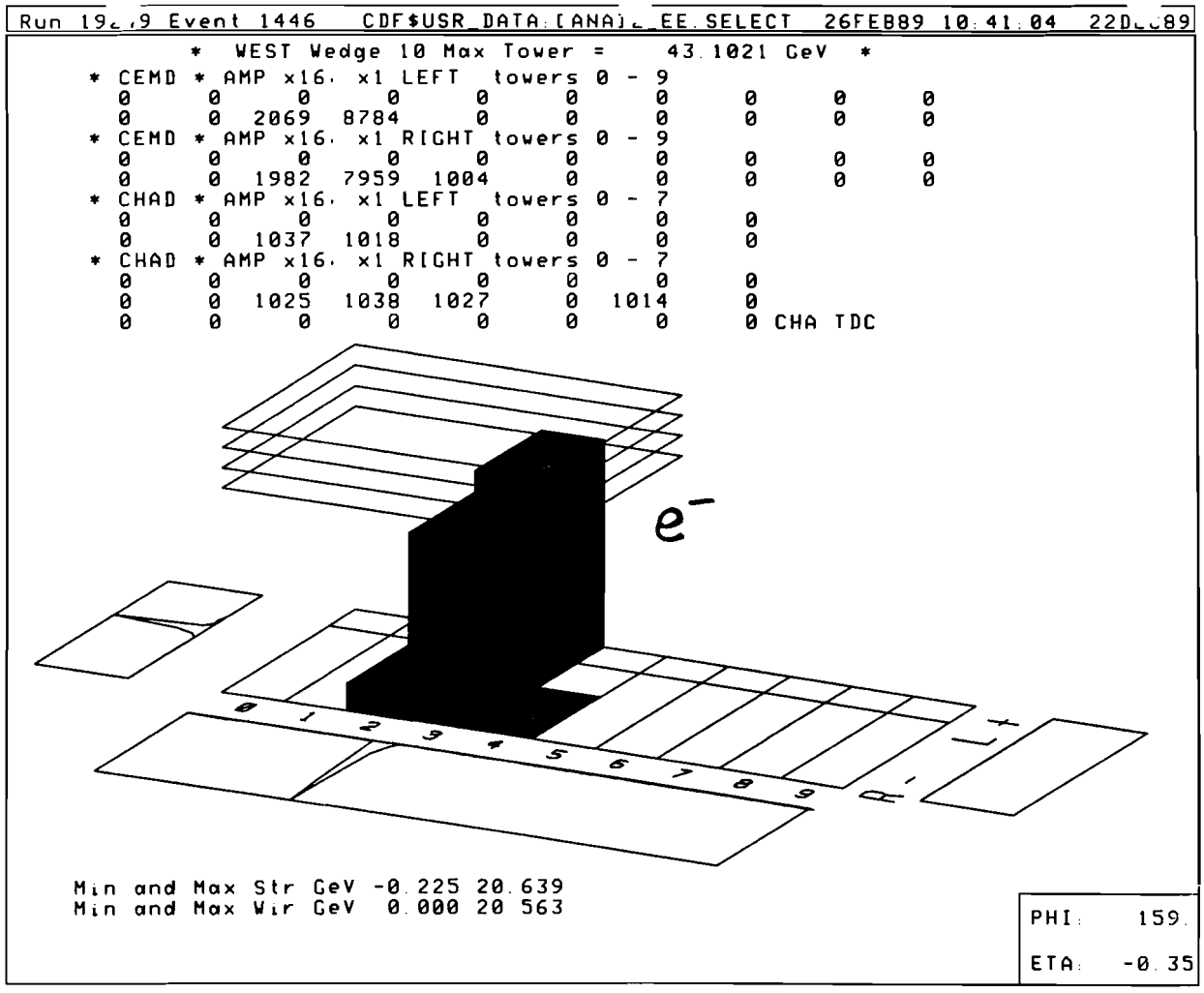

Figure 40: The display of the wedge at which the electron deposited its energy. The electron shower is mostly in one tower. The electron energy is calculated using energies in towers 2 and 3. The CES shower profiles in x and z views show the location of the electron shower within a wedge. The raw energies of strip and wire are 20.64 GeV and 20.56 GeV.

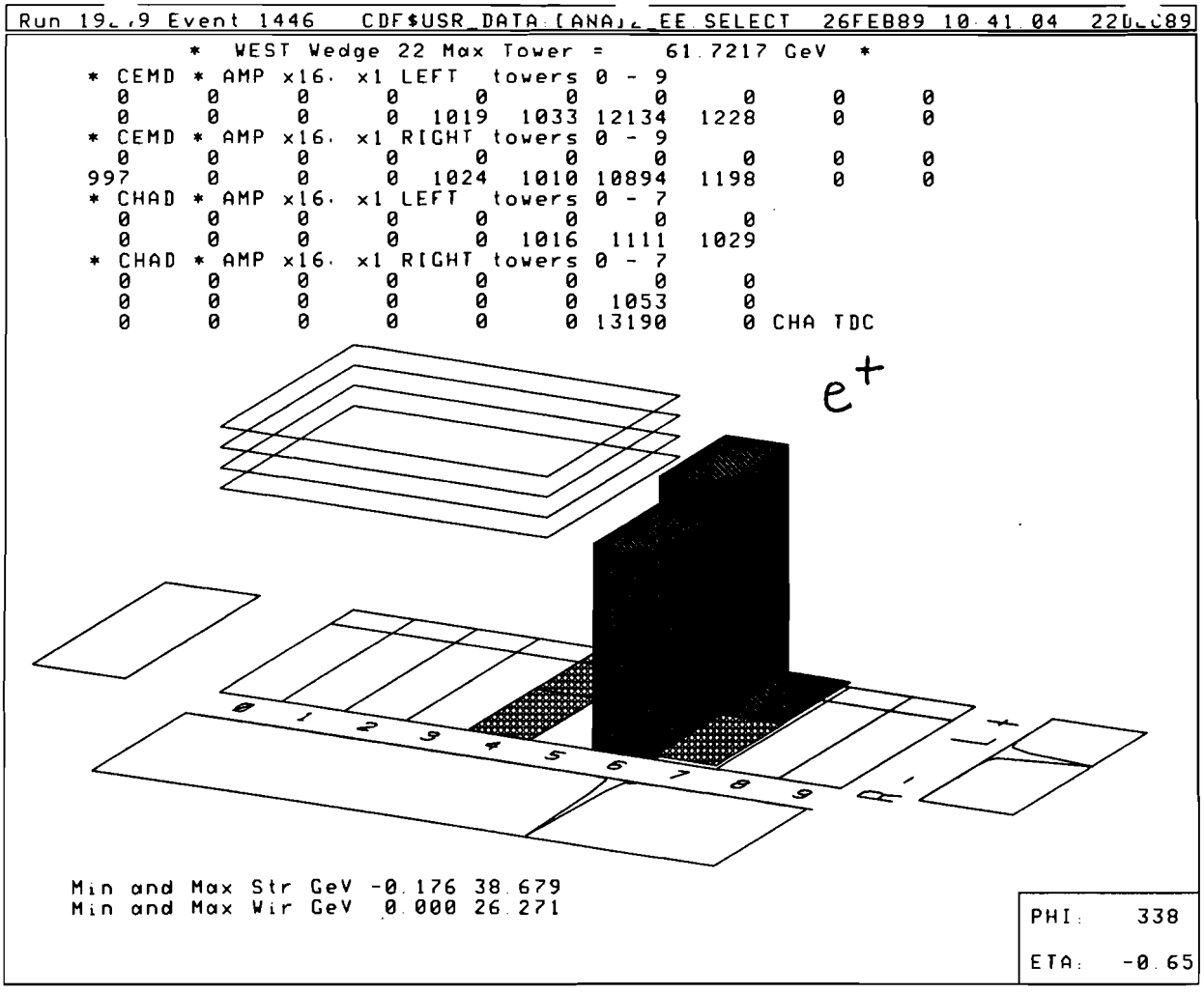

Figure 41: The display of the wedge at which the positron deposited its energy. The positron deposited most of its energy in tower 6. The CES shower profiles in x and z views show the location of the positron shower within a wedge. The calorimeter response to electrons and positrons does allow to determine their energies but not their charge.

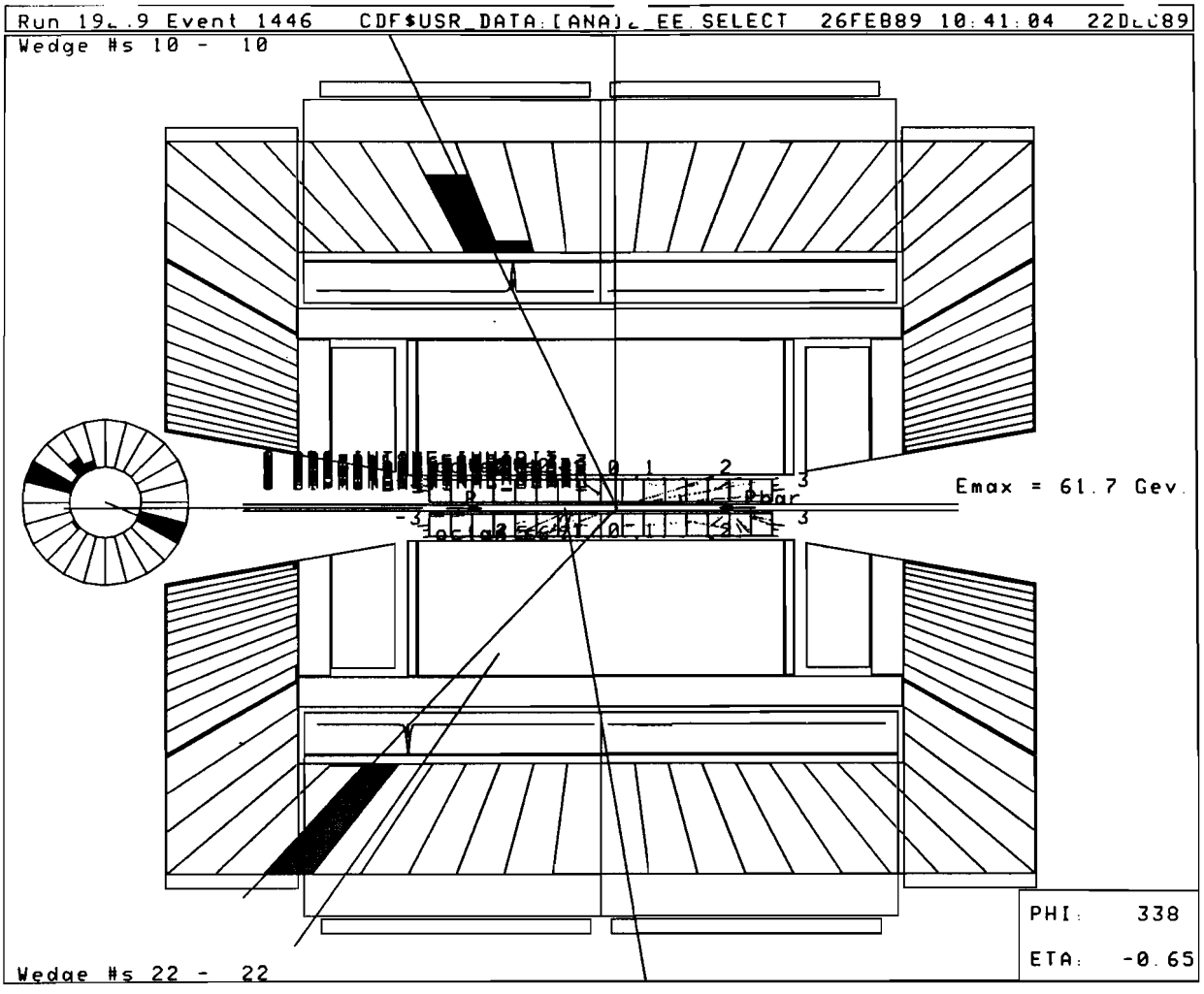

Figure 42: The side view of Z→ e^+e^- candidate in a $\bar{p}p$ collision- rz view. The detector is symmetric about the beam pipe. The direction of protons and anti-protons are shown. The combination of VTPC, CTC, CES, and CEM measurements can be seen by following the electron and positron tracks.

B The Kolmogorov-Smirnov Statistic

If any parameter in a probability distribution is estimated from data, the distribution of the Kolmogorov-Smirnov statistic, $D_N = \max|S_N(X) - F(X)|$, is dependent on the probability function used in a fit. The cumulative distributions of data, $S_N(X)$, and that of a probability function, F(X), cover the same range of X. This appendix describes the procedure to determine the confidence level of the fit results for 72 $Z \rightarrow e^+e^-$ candidates. First, I give the the confidence level calculated from theory[20],[22]. Next, a Monte Carlo test is carried out to check the result from theory. This test also checks the algorithm that is used to prepare the D_N distribution. In the last step, Monte Carlo method is used to prepare D_N distribution using fit results from each sample.

The 72 $Z \rightarrow e^+e^-$ candidates are fitted using a Gaussian convoluted relativistic Breit-Wigner distribution. The maximum distance between the cumulative distributions of data and probability function is 0.0547. The universal (independent of the probability distribution) Kolmogorov-Smirnov statistic assigns a 98.2% confidence level to a distance of 0.0547 given the 72 events[20],[22]. This result is checked by preparing a distribution of D_N using Monte Carlo method. The distribution of D_N (Fig. 43a) is prepared from generated samples of a Gaussian convoluted relativistic Breit-Wigner distribution. Each sample consists of 72 events. The confidence level read from figure 43a is $96.9 \pm 6.5\%$. This agrees with the value calculated from theory.

The distribution of D_N calculated using the fit results from each sample is shown in figure 43b. From this distribution, a confidence level of $81.6 \pm 6\%$ is found for the maximum distance of 0.0547 for the 72 $Z \rightarrow e^+e^-$ candidates. The distribution in figure 43a is broader than the distribution in figure 43b.

In addition to being a bin independent test, the Kolmogorov-Smirnov statistic shows no dependence on the quantities found in the likelihood fits (Fig. 44.) Figure 44a shows no correlation between the fitted mass and the maximum distance, D_N. Similarly, fig-

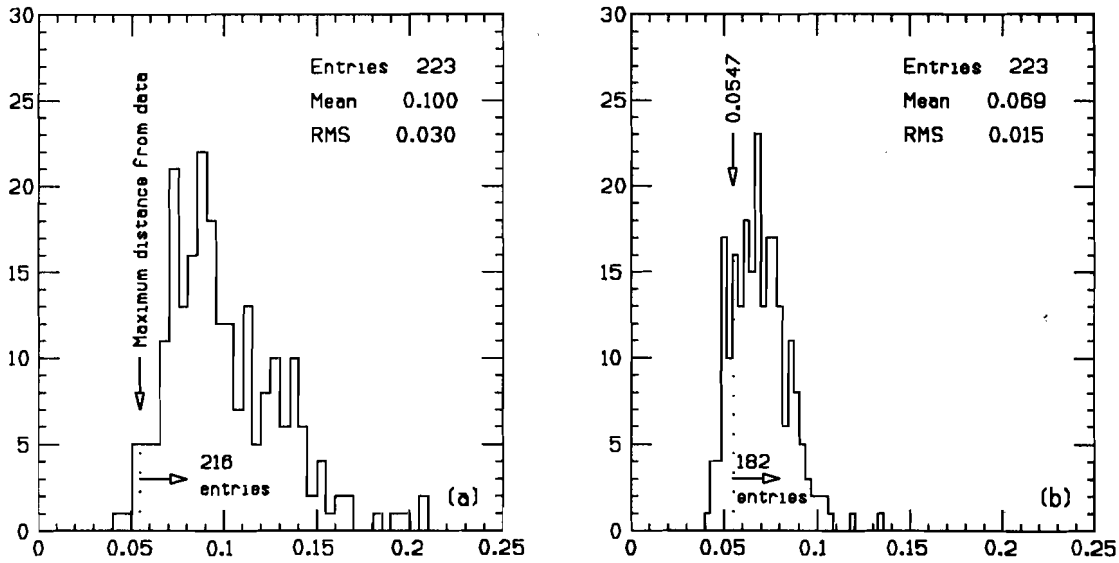

Figure 43: Distributions of the Kolmogorov-Smirnov statistic prepared from 72 events generated according to a Gaussian convoluted relativistic Breit-Wigner probability function. a) An input mass of 91 GeV/c^2 , and width of 2.5 GeV are used to calculate the maximum distance. The confidence level is the ratio of 216 to 223 entries: 0.969. The probability of finding a maximum distance greater than 0.0547 is $96.9 \pm 6.5\%$. b) The fit results from each sample are used to calculate the maximum distance. The confidence level is the ratio of 182 to 223 entries: 0.816. The distribution in a) is universal; the shape of this distribution is independent of the probability function used to calculate the maximum distance. If any parameter of a probability function is estimated from data, a distribution such as in b) has to be prepared to quote a confidence level.

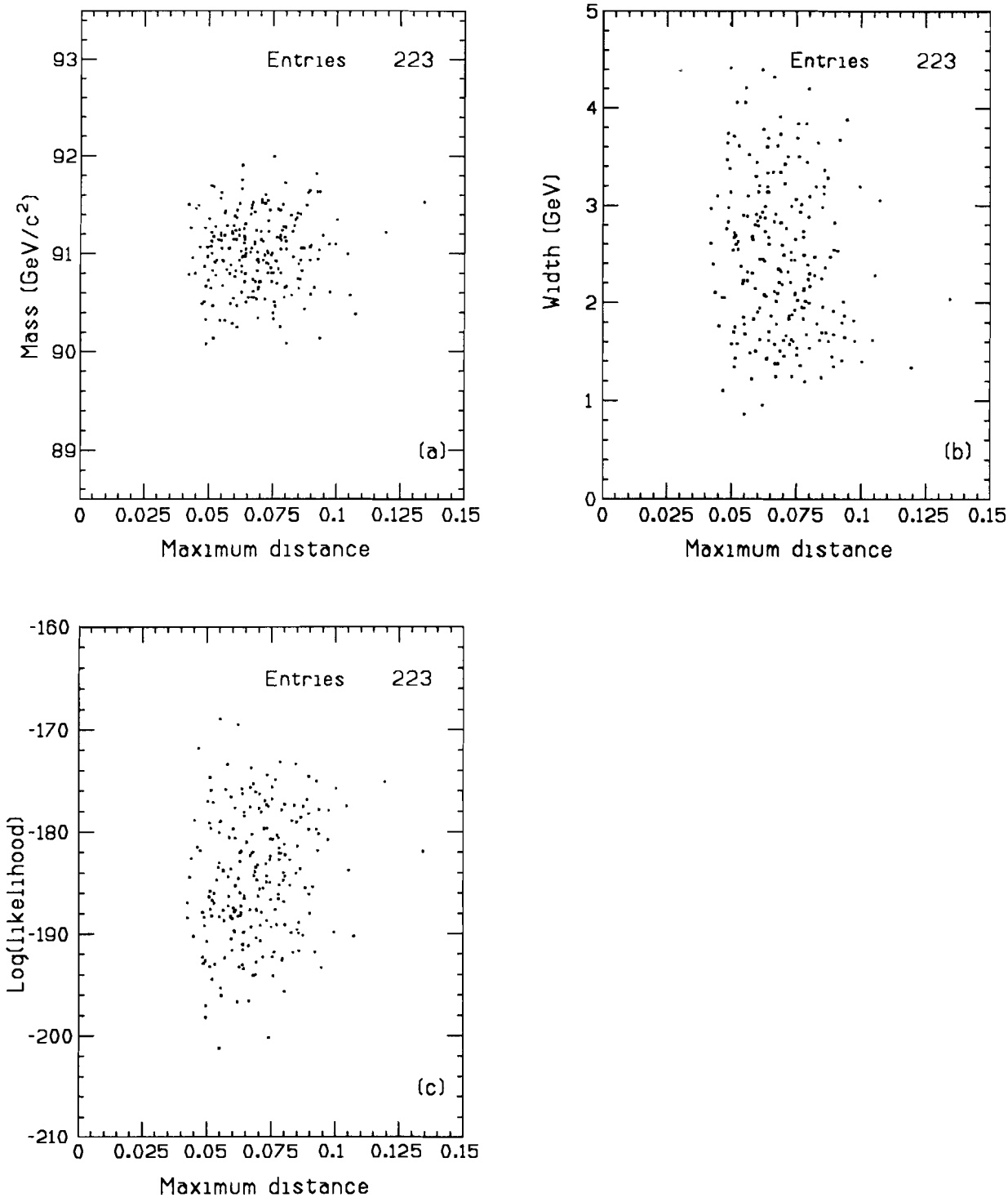

Figure 44: Scatter plots of the maximum distance (Kolmogorov-Smirnov statistic) and the fitted parameters from 223 Monte Carlo samples. a) Fitted mass vs. maximum distance. b) Fitted width vs. maximum distance. c) Log(likelihood) vs. maximum distance. These plots indicate the Kolmogorov-Smirnov statistic is not correlated with the fitted results.

ure 44b shows no correlation between the fitted width and D_N. The scatter plot of the log(likelihood) against D_N shows that the distribution of the Kolmogorov-Smirnov statistic is independent of the fitting procedure (Fig. 44c.)

With a confidence level of $81.6 \pm 6\%$, a Gaussian convoluted relativistic Breit-Wigner distribution describes the distribution of 72 $Z \rightarrow e^+e^-$ candidates.

C CDT z position calibration

The CDF Central Drift Tubes Array(CDT) is described in detail in references [35],[36]; in this note I describe how the position measurement along the beam direction (the z axis) was calibrated. The first calibration took 25 days(24 working hours) to carry out in 1987. In 1988 a faster method was implemented to collect Fe^{55} source data. Routinely the data was collected within 15 hours during a calibration period.

The CDT [35] is located inside the solenoidal superconducting coil and is mounted on the Central Tracking Chamber(CTC). The CDT array consists of 2016 cylindrical tubes of 12.7 mm diameter each arranged in three layers. The CDT is $\sim$ 3 meters long and its radial thickness is 3.8 cm. The radial thickness is constrained by the dimensions of the outer radius of the CTC and the bore of the solenoid magnet(Fig. 45.) To reduce the number of electronic readout channels pairs of tubes are connected(electrical) together at the west end. They are located in the same layer separated by eight tubes(Fig. 47.) The effective length of the sense wires are doubled, $\sim$ 6 meters. The timing and the charge information of each tube-pair is readout using two QVC(charge to voltage converter) channels and a single TVC(time to voltage converter) channel. The measured charges and time are used to calibrate the z position measurement of the CDT. In $\overline{p}p$ data the measured charges and time are also used to measure the $r\phi$ position of a track. This measurement method is not described in this appendix and is the subject of another note.

The charge division is based on the fact that the electric potential drop across two parallel resistors is equal. Whenever a charge of Q amount is deposited along the sense wire in a drift tube, at that location the sense wire is divided up into two resistors with respect to ends(Figure 46.) Here is the derivation of the charge division formula.

$$\frac{dQ_0}{dt}(\frac{l}{2} + x)\rho = \frac{dQ_1}{dt}(\frac{l}{2} - x)\rho, \tag{29}$$

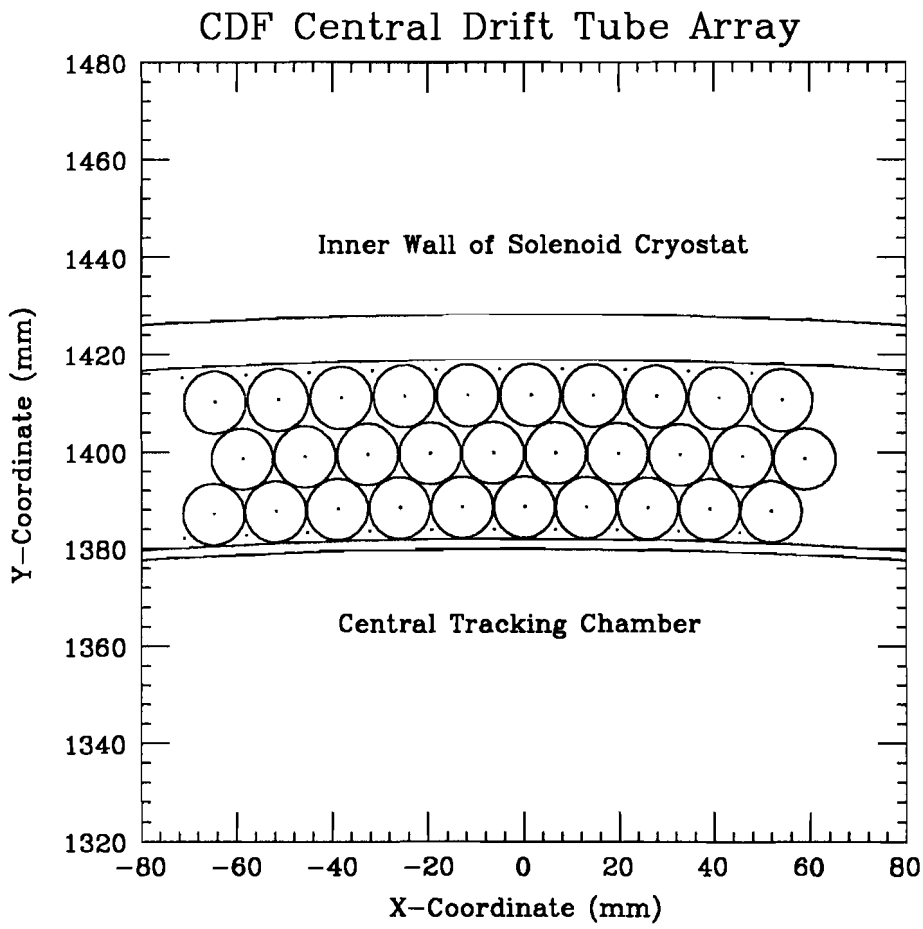

Figure 45: Detail of the CDT array's drift tube geometry.

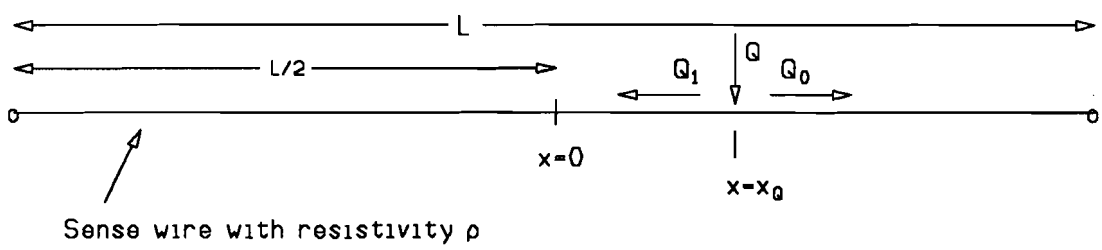

Figure 46: Schematic view of a charge division process. Charge Q is deposited at $x = x_Q$. The charges(Q_0, Q_1) are measured from the ends of sense wire, their magnitude depends on the resistances from the ends to the x_Q position and on the magnitude of the total charge Q.

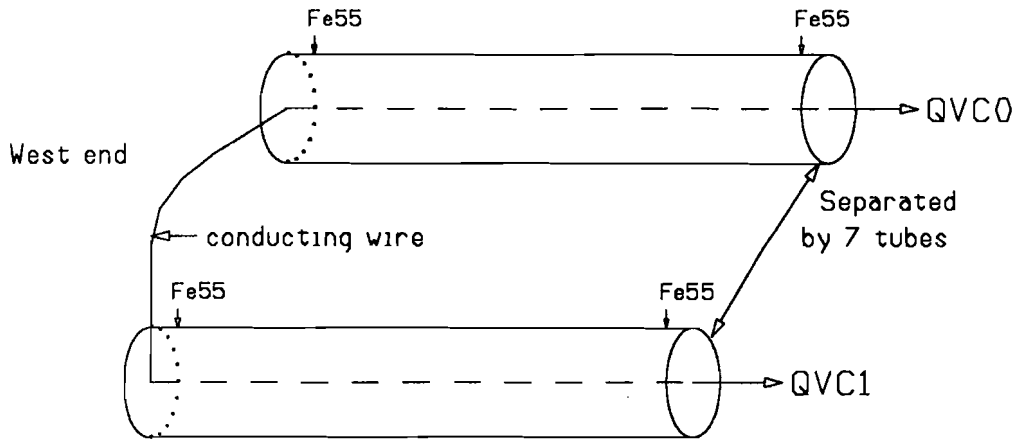

Figure 47: Schematic of a single tube-pair readout system.

the wire length,l, and the wire resistance per unit length, ρ, are time independent. The position x and wire length are measured in units of cm. Integrating over time and solving for x the charge division formula is:

$$R = \frac{2x}{l} = \frac{Q_0 - Q_1}{Q_0 + Q_1}. \tag{30}$$

When deriving R it was assumed that ρ is a constant and independent of position along the wire. The charge division ratio R ranges from -1 to +1. There are two Fe^{55} sources located ~18 cm away from the ends of a drift tube; the distance between the sources are known to within 0.1 mm. These sources provide 2 position measurements that help determine the slope in the line equation. A line equation is used to convert the position measurement from R space to the physical space(z axis). The readout schematic of a single tube-pair is shown in figure 47. The sense wires resistance from end to end of a tube is $R_1 \sim R_2 \sim 1988 \pm 3\Omega$. Each tube capacitance is about 40 pf. The high voltage blocking capacitor at the end of a drift tube makes the charge division equation time dependent. Another source of time dependence is introduced by blocking capacitors at

the inputs of the rabbit QVC channels. A tube-pair can be treated as an RC circuit with time constant τ = RC. By a straight forward but involved calculation the time dependent charge division formula is derived to be:

$$R = \frac{2x}{l} = \frac{Q_0 - Q_1}{Q_0 + Q_1} e^{-t/\tau}. \tag{31}$$

Where τ is charge decay time constant. In the charge division equation time and position independent constants are not shown; they are absorbed in the Fe^{55} calibration constants. The charge division equation in terms of measured quantities is:

$$R = \frac{Q_0' - Q_1'}{Q_0' + Q_1'} e^{t'/\tau}. \tag{32}$$

The most important tool used to collect Fe^{55} calibration data is the set of level-1 CDT trigger cards [37]. These cards are designed to select up to four fold coincidence of tube-pairs. The PAL (Programmable Array Logic) multiplicity logic units on each card are controlled by addressable R/W(read/write) registers and enabled triggering off of a single drift tube-pair. Typical singles counting rates per drift tube-pair from cosmic rays plus Fe^{55} sources were ~60 Hz. The CDF DAQ(data acquisition) system and the main CDF trigger module(CDFFRED) are used to collect Fe^{55} calibration data in the $\bar{p}p$ physics data collection mode.

Digitized data is read and manipulated by an MX. The MX computer is designed to collect data from CDF electronics. The CDT array is readout using 4 MXs working in parallel. This way it is possible to trigger off of 4 drift tube-pairs in parallel and collect calibration data 4 times faster. But the main gain in speed comes about by avoiding the bottleneck that exists when the data is transferred from the MXs to tape [38]. I'm avoiding the discussion of the system that transferred the data from the MXs to the output tape, it's irrelevant to this calibration. The bottleneck gets avoided by storing

1000 source events in the MX memory and transferring them all at once to the tape. For each trigger(event), the source data length consists of eight 16 bit words arranged in the MX memory as follow: trigger number, junk word, LID(logical ID of a drift tube-pair),TVC,LID+1,QVC0,LID+2,QVC1.

Without any selection cuts the MX memory will be swamped with data from other tube-pairs. For example, the first trigger of a single drift tube-pair provides information and at the second trigger three drift tube-pairs provide information. In this mode it is not definitely possible to know that there are 1000 events recorded from the same drift tube-pair. For each trigger there is data from the tube that was selected to begin with, but triggers from cosmic rays or coincidence hits from other tube-pairs can also be present. To help out the offline analysis and also to reduce data not coming from Fe^{55} decay, it is required there to be only a single time(TVC) information present in the MX memory per trigger. The requirement of single TVC eliminates both cosmic rays that triggers two or more tube-pairs and coincident Fe^{55} decays. Each tube-pair has one time measurement. The raw data output is displayed in figures 48,49, 50.

The calibration constants that need to be determined are the 4 source positions in charge division space(R) and the RC time constant of the drift tube-pair. Two additional parameters are added to check any offsets that the digitized charges Q_0 and Q_1 might have. These offsets add 2 more parameters in the fit, the parameters are denoted as 'a' and 'b'. The content of figure 50 motivated me to develop an algorithm to estimate all 7 parameters of a drift tube-pair. The equation of the charge division that parametrizes source position(line equation) in figure 50 is:

$$G_i = [(Q_0 - a) + (Q_1 - b)] \times R_i - [(Q_0 - a) - (Q_1 - b)] \times e^{t/\tau}] \equiv 0. \qquad (33)$$

The parameters of four sources are fitted simultaneously, there are four line equations that allow to estimate 8 parameters. From the simultaneous fit 7 parameters are estimated.

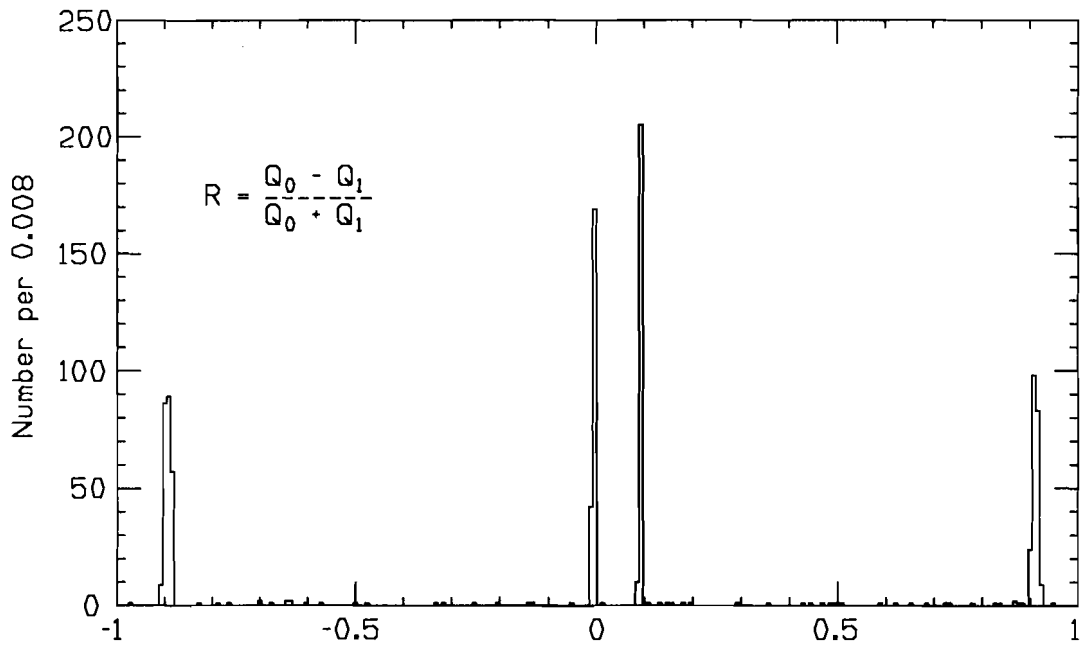

Figure 48: Charge division distribution of a drift tube-pair. Fe^{55} peaks are clearly visible, each tube has two sources.

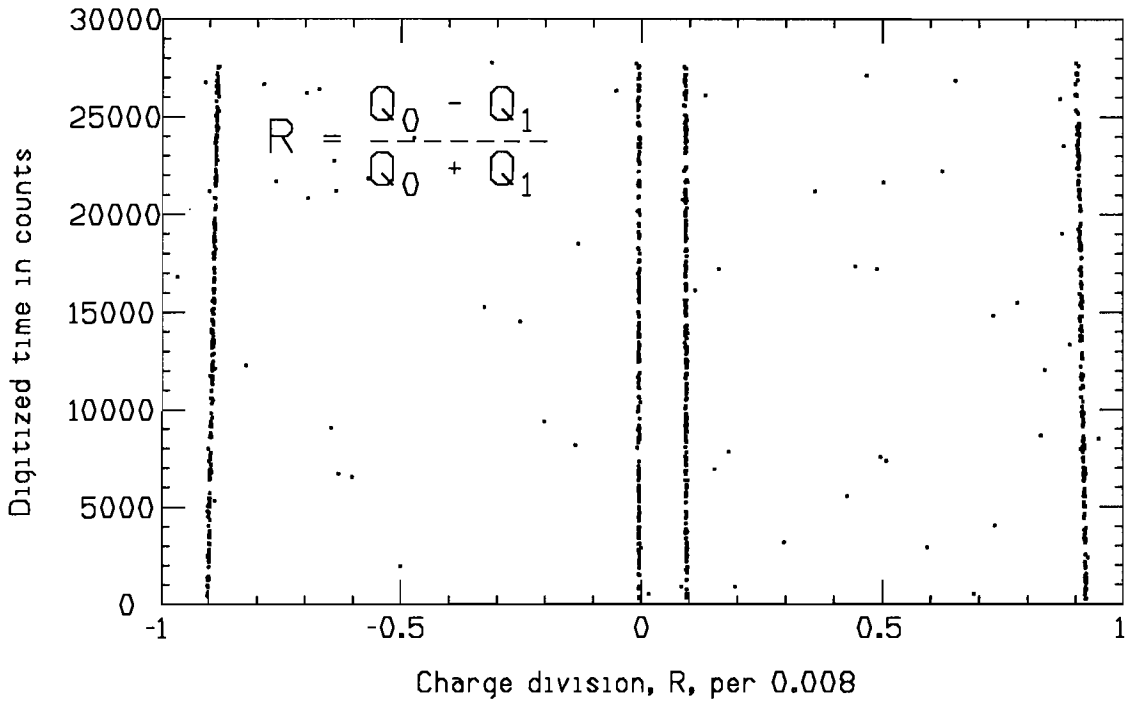

Figure 49: Measured time in counts vs. charge division distribution of a drift tube-pair. The source distributions near $\sim \pm 1$ show time dependence, this time dependence comes from the capacitances present in the drift tube-pair readout.

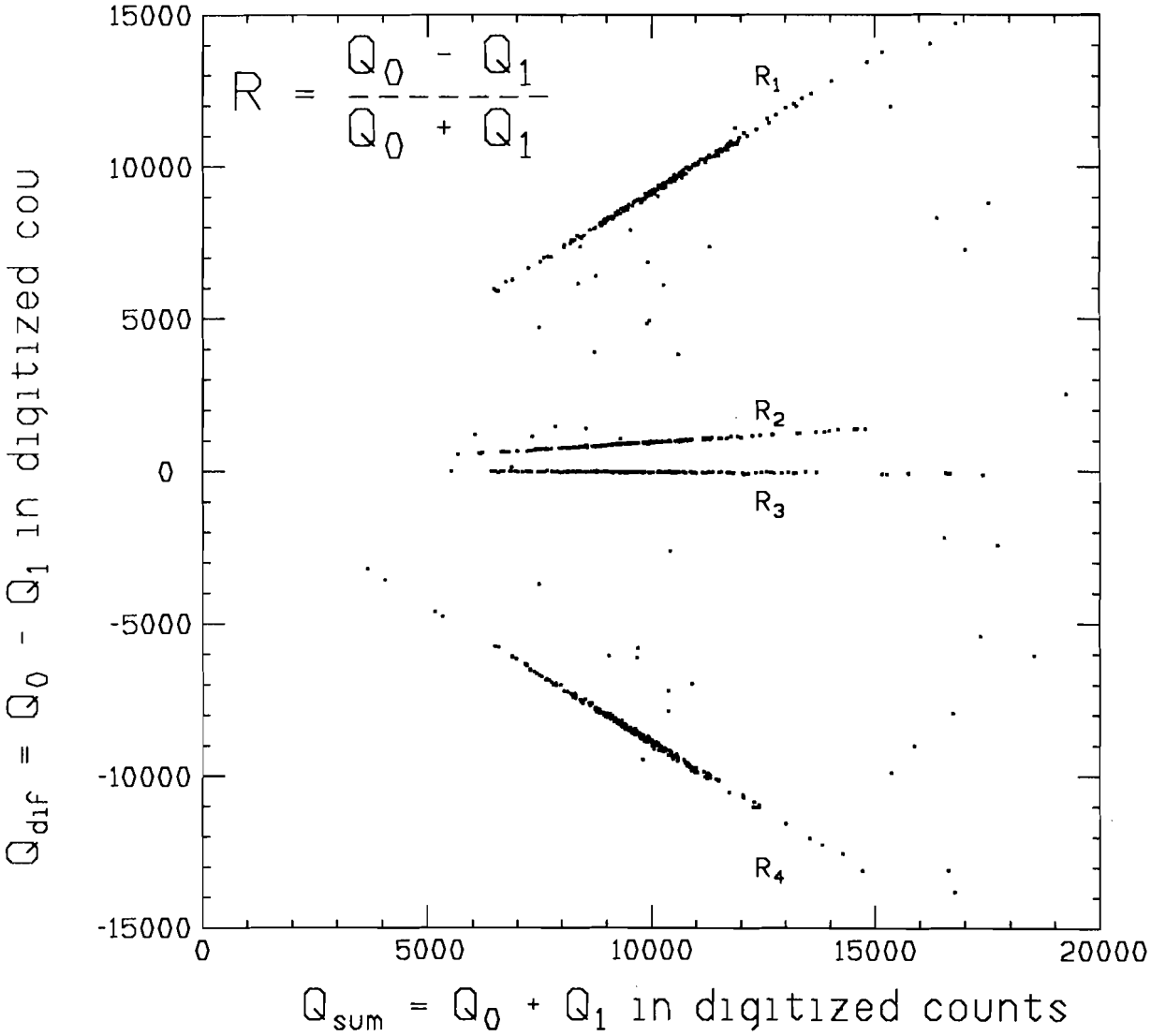

Figure 50: Difference of charges Q_0 and Q_1 vs. the sum of the charges Q_0 and Q_1. The slopes of the four lines give the positions of the Fe^{55} sources in the charge division space, these are the calibration constants. The linear dependence of charge division can be seen from this plot, although there is time dependence introduced by RC time constant of the drift tube-pair.

Fitting algorithm is as follow: 1) Fit each source location(the slope) independently and take this to the zeroth order estimate of the i-th source position. 2) From resistances and capacitances of a drift tube-pair system it is possible to estimate the RC time constant. The average RC time constant for drift tube-pairs $\sim$ 35 μs, this is taken to be the zeroth order estimate of τ. 3) The zeroth order estimate of a and b is 0, this is what we expect from well calibrated electronics. 4) the functional form G_i is linearized to iteratively estimate the best parameters; Taylor series expansion is carried out about the known estimates of the parameters. 5) The chi-squared is minimized iteratively to estimate the best value of the 7 parameters.

The average value of the goodness of fit test, χ^2, indicates the resolution of the electronics that measure the charges to be $\sim$ 9 counts. From the distributions of the offset parameters I conclude that the electronics are well calibrated, and that the rate at which they were calibrated is appropriate.

The average charge division value(R_0) of the middle two sources tell where the tubes are connected together. In $\overline{p}p$ data this information is used to decide in which tube a charged particle passed through. The calibration constants of each tube differs somewhat in magnitude, and 50% of source positions have opposite sign. The physical position of each source with respect to tube ends is measured prior to installation; using this information and the source positions from the fit we can calculate the slope that transforms position measured in R space to physical space(z axis). The relation is:

$$\begin{aligned} z &= R * m_i + intercept \\ z &= R * \frac{z_2 - z_1}{R_2 - R_1} + intercept, \end{aligned} \tag{34}$$

where R is the charge division ratio of a tube, the z_2,z_1 are the measured physical positions of 2 sources and the R_2,R_1 are the fitted positions of 2 sources in the charge division space. The intercept was chosen as to make the z position symmetric about z=0, z range

is $\sim \pm 1.5$ meters.

The CDT z measurement resolution is $\sim$ 6mm for large p_t tracks, for all range of p_t and ϕ, θ angles the resolution is $\sim$ 10mm. Hence the fractional resolution of CDT is: $0.17\% = \frac{10\ \mathrm{mm}}{6000\ \mathrm{mm}}$. The CDT-CTC track matching resolution along z axis is about 1 cm, and no z position dependence bias is observed within the resolutions of both CDT and CTC detectors.

References

[1] S. Weinberg, Phys. Rev. Lett.**19**, 1264(1967), Phys. Rev. Lett. **27**, 1690(1971). A. Salam, in Elementary Particle Physics, edited by N. Svartholm(Almqvist and Wiksells, Stockholm, 1968), p. 367. S.L.Glashow, Nucl. Phys. **22**, 579(1961).

[2] P. W. Higgs, Phys. Lett. **12**, 132(1964), Phys. Rev. Lett. **13**, 508 (1964), Phys. Rev. **145**, 1156 (1966).

[3] F. Abe et al.(CDF collaboration). The CDF Detector: An Overview. *Nuclear Instruments and Methods in Physics Research*, **A271**, 387-403(1988).

[4] G. Arnison et al.(UA1 Collaboration) Phys. Lett. 126 **B**(1983) 398; Phys. Lett. 129 **B**(1983) 273;
P. Bagania et al.(UA2 Collaboration) Phys. Lett. 129 **B**(1983) 130.

[5] M. Böhm, W. Hollik, Nucl. Phys. **B 204**, 45(1982).
V. D. Barger and R. J. N. Phillips, *Collider Physics*(Addison-Wesley, Reading, Massachusetts, 1987).

[6] R. Snider et al. CDF Vertex Time Projection Chamber system. *Nuclear Instruments and Methods in Physics Research*, **A268**, 75-91(1988).

[7] L. Balka et al., The CDF Central Electromagnetic Calorimeter. *Nuclear Instruments and Methods in Physics Research*, **A267**, 75-91 (1988).

[8] S. R. Hahn et al., Calibration Systems for the CDF Central Electromagnetic Calorimeter. *Nuclear Instruments and Methods in Physics Research*, **A267**, 75-91(1988).

[9] S. Bertolucci et al., The CDF Central and Endwall Hadrom Calorimeter. *Nuclear Instruments and Methods in Physics Research*, **A267**, 301-314 (1988).

[10] D. Amidei et al. A two Level FASTBUS Based Trigger System for CDF. *Nuclear Instruments and Methods in Physics Research*, **A267**, 75-91(1988).

[11] G. W. Foster et al. A Fast Hardware Track-Finder for the CDF Central Tracking Chamber. *Nuclear Instruments and Methods in Physics Research*, **A269**, 75-91(1988).

[12] The trigger clustering scheme searched for trigger cells with more than 4 GeV of energy and grouped all adjacent cells with more than 3.6 GeV of energy into a cluster.

[13] F. Abe et al(CDF collaboration). Search for New Heavy Quarks in Electron-Muon Events at the Fermilab Tevatron Collider. *Physical Review Letters*, 64(2):147, 1990.

[14] Each cluster is formed from 4 or less trigger cells.

[15] K. Yasuoka et al. Response Maps of the CDF Central Electromagnetic Calorimeter with Electrons. *Nuclear Instruments and Methods in Physics Research*, **A267**(1988) 315-329.

[16] F. Abe et al(CDF collaboration). Transverse-Momentum Distributions of Charged Particles Produced in $\overline{p}p$ Interactions at $\sqrt{s} = 630$ and 1800 GeV. *Physical Review Letters*, 61(1819:1822), 1990.

[17] Z and Drell-Yan cross section measurement at $\sqrt{s} = 1.8$ TeV. In preparation to be published.

[18] C. Newman-Holmes, E. E. Schmidt, and R. Yamada, *Nuclear Instruments and Methods in Physics Research*, **A274**, 443 (1989).

[19] The Particle Data Group. Review of Particle Properties. *Physics Letters*,**B204**, April 1988.

[20] W. T. Eadie, D. Drijard, F. E. James, M. Roos, B. Sadoulet. STATISTICAL METHODS In Experimental Physics. North-Holland Publishing Company, 1971
A. G. Frodesen, O. Skjeggestad, H. Tofte. Probability and Statistics in Particle Physics. UNIVERSITETSFORLAGET, 1979

[21] F. James and M. Roos. Function Minimization and Error Analysis. CERN Computer Centre Program Library. D506, 1983.

[22] W.Press, B. Flannery, S. Teukolsky, and W. Vetterling. NUMERICAL RECIPIES. Cambridge University Press, 1986.

[23] F. Paige and S.D. Protopopescu. Technical Report BNL 38034, Brookhaven National Laboratory, 1986(unpublished). $\bar{p}p$ physics simulation program(V6.22).

[24] R. G. Wagner, M. Mangano, and I independently verified the mass shift due to the structure function.

[25] E. Eichten, I. Hinchliffe, K. Lane, and C. Quigg. Supercollider Physics. *Reviews of Modern Physics*, **56**(1984) 579; erratum **58**(1986) 1065.

[26] D. Duke and J.F. Owens. Q^2-Dependent Parametrizations of Parton Distribution Functions. *Physical Review*, D **30**(1984) 49.

[27] M. Diemoz, F. Ferromi, E. Longo, and G. Martinelli. Parton Densities from Deep Inelastic Scattering to Hadronic Processes at Super Collider Energies. *Z. Phys.*,C **39**(1988) 21.

[28] Michelangelo Mangano. QED Radiative Corrections to Final State Leptons in Z, J/ψ and Υ Decays. CDF Note 1006,(1989 unpublished.)

[29] R.G. Wagner(unpublished) based on calculations by F. Berends *et al.*, Z. Phys. C **27**, 155 (1985).

F. Berends and R. Kleiss, Z. Phys. C **27**, 365 (1985).

G. Marchesini and B. Webber, Nucl. Phys. **B310**, 461 (1988).

G. Bonvicini and L. Trentadue, University of Michigan Report No. UM-HE-88-36(to be published).

[30] F. Abe et al(CDF collaboration). Measurement of the ratio $\sigma(W \to e\nu)/\sigma(Z \to ee)$ in $\overline{p}p$ Collisions at $\sqrt{s} = 1.8$ TeV $= 1.8$ TeV. *Physical Review Letters*, 64(152:156), 1990.

[31] I acknowledge the suggestion by Joe R. Incandela, member of the UA2 experiment at CERN. His work and suggestions as how to test the statistical uncertainty of the Z mass, by using Monte Carlo, was passed on to me by Henry Frisch.

[32] The statistical uncertainty from a maximum likelihood fit is equal to the square root of the variance divided by the number of events; $\sigma_\theta = \sqrt{Var(\theta)/N}$. The dimensionless quantity, $z = (x - \mu)/\Gamma$, is common to both the Breit-Wigner and the Gaussian distributions. The variance of the location parameter, μ is: $\int_{-\infty}^{+\infty} \left(\frac{df}{d\mu}\right)^2 \frac{1}{f} dx$, and the variance of the scale parameter, Γ, is: $\int_{-\infty}^{+\infty} \left(\frac{df}{d\Gamma^2}\right)^2 \frac{1}{f} dx$. [20].

The calculation of uncertainties for distributions that are convolution of two distributions in general is best accomplished by Monte Carlo method. The uncertainty of the location parameter can still be calculated as described above, but the uncertainty calculation of the scale parameter is ambiguous except for special cases; a) Convolution of two Gaussian, and b) Convolution of two Breit-Wigner distributions. The dependence of uncertainties on the scale parameters, width and resolution, is always present.

[33] The standard Kolmogorov-Smirnov statistic is not applicable in the case where the parameters are estimated from the sample[20].

[34] G. Abrams et al.(Mark II Collaboration) : *Phys. Rev. Lett.* **63**(1989) 2173;
D. Decamp et al. (ALEPH Collaboration) : Phys. Lett. **231B**(1989) 519;
P. Aarnio et al. (DELPHI Collaboration) : Phys. Lett. **231B**(1989) 539;
B. Adeva et al. (L3 Collaboration) : Phys. Lett. **231B**(1989) 509;
M.Z. Akrawy et al. (OPAL Collaboration) : Phys. Lett. **231B**(1989) 530.

[35] S. Bhadra et al., **The Design and Construction of the CDF Central Drift Tube Array**, Nuclear Instruments and Methods in Physics Research. **A268** (1988) 92-104.

[36] S. Bhadra et al., **A Computer-Controlled Wire Tension Measurement System Used in the Fabrication of the CDF Central Drift Tube Array**, Nuclear Instruments and Methods in Physics Research. **A269** (1988) 33-39.

[37] Phil Schlabach is the expert of the CDT level-1 cards. He wrote the software to mask the trigger channels, wrote the fortran interface software to write to the registers on the trigger cards. My summary of the CDT trigger system does not do justice to his effort and to his time spent on maintaining the system. Together we speeded up the Fe^{55} source data collection for both the CDT and the CMU systems. His help made it worth while the time that I spent working on this project.

[38] Walter Stuermer of the PIG group suggested this procedure to me. He helped me throughout the development of the MX microcode, with this microcode it was possible to analyze and store the source data in the MX memory. I'm deeply indebted to him in his suggestions and help in speeding up the collection of Fe^{55} source data.

Vita

Hovhannes Keutelian's existence on earth began three decades ago in Lebanon. The international atmosphere of Beirut and its metropolitan character gave him the taste of living in a great city. It was in 1975 when he first learned about physics; he thought physics was the way to learn all about the physical world – a laudable goal, but a big mistake. In October, 1978, he emigrated to the United States with his family; this was after living for 3 years through the civil war in Lebanon and watching the destruction of neighbourhoods in and around Beirut. From 1979-1981 he attended the College of Lake County in Grayslake, Illinois. In 1981 he transferred to the University of Illinois undergraduate physics program. He received a B.S. in physics in 1983. His graduate physics education continued at the same institution; where, seduced by the glamour of "world class" physics, he joined the largest experimental high energy group (This was in 1984-87.) in the world – CDF. This was a great opportunity for him to also major in sociology; but, overworked and underpaid, he decided to pursue only high energy physics.... In March 1989, at the suggestion of Larry Nodulman, he quit vacillating and concentrated his efforts on measuring the Z mass. In the summer of 1989, despite constant harassment from Vic and Phil, he and other CDF physicists made the then most precise measurement of the Z mass. They held this great honor for 1 day. In 1990 he completed the PhD degree and moved on to...?